

University of Windsor

Scholarship at UWindor

Electronic Theses and Dissertations

Theses, Dissertations, and Major Papers

2011

Design of Heat Treatment for Production of Austempered Ductile Iron (ADI) With Targeted Automotive Applications

Tanzim Nasir
University of Windsor

Follow this and additional works at: <https://scholar.uwindsor.ca/etd>

Recommended Citation

Nasir, Tanzim, "Design of Heat Treatment for Production of Austempered Ductile Iron (ADI) With Targeted Automotive Applications" (2011). *Electronic Theses and Dissertations*. 7951.
<https://scholar.uwindsor.ca/etd/7951>

This online database contains the full-text of PhD dissertations and Masters' theses of University of Windsor students from 1954 forward. These documents are made available for personal study and research purposes only, in accordance with the Canadian Copyright Act and the Creative Commons license—CC BY-NC-ND (Attribution, Non-Commercial, No Derivative Works). Under this license, works must always be attributed to the copyright holder (original author), cannot be used for any commercial purposes, and may not be altered. Any other use would require the permission of the copyright holder. Students may inquire about withdrawing their dissertation and/or thesis from this database. For additional inquiries, please contact the repository administrator via email (scholarship@uwindsor.ca) or by telephone at 519-253-3000ext. 3208.

Design of Heat Treatment for Production of Austempered Ductile
Iron (ADI) With Targeted Automotive Applications

by
Tanzim Nasir

A Thesis
Submitted to the Faculty of Graduate Studies
through Engineering Materials
in Partial Fulfillment of the Requirements for
the Degree of Master of Applied Science at the
University of Windsor

Windsor, Ontario, Canada

2011

© 2011 Tanzim Nasir



Library and Archives
Canada

Published Heritage
Branch

395 Wellington Street
Ottawa ON K1A 0N4
Canada

Bibliothèque et
Archives Canada

Direction du
Patrimoine de l'édition

395, rue Wellington
Ottawa ON K1A 0N4
Canada

Your file *Votre référence*
ISBN: 978-0-494-81745-2
Our file *Notre référence*
ISBN: 978-0-494-81745-2

NOTICE:

The author has granted a non-exclusive license allowing Library and Archives Canada to reproduce, publish, archive, preserve, conserve, communicate to the public by telecommunication or on the Internet, loan, distribute and sell theses worldwide, for commercial or non-commercial purposes, in microform, paper, electronic and/or any other formats.

The author retains copyright ownership and moral rights in this thesis. Neither the thesis nor substantial extracts from it may be printed or otherwise reproduced without the author's permission.

In compliance with the Canadian Privacy Act some supporting forms may have been removed from this thesis.

While these forms may be included in the document page count, their removal does not represent any loss of content from the thesis.

AVIS:

L'auteur a accordé une licence non exclusive permettant à la Bibliothèque et Archives Canada de reproduire, publier, archiver, sauvegarder, conserver, transmettre au public par télécommunication ou par l'Internet, prêter, distribuer et vendre des thèses partout dans le monde, à des fins commerciales ou autres, sur support microforme, papier, électronique et/ou autres formats.

L'auteur conserve la propriété du droit d'auteur et des droits moraux qui protègent cette thèse. Ni la thèse ni des extraits substantiels de celle-ci ne doivent être imprimés ou autrement reproduits sans son autorisation.

Conformément à la loi canadienne sur la protection de la vie privée, quelques formulaires secondaires ont été enlevés de cette thèse.

Bien que ces formulaires aient inclus dans la pagination, il n'y aura aucun contenu manquant.


Canada

DECLARATION OF CO-AUTHORSHIP / PREVIOUS PUBLICATION

I. Co-Authorship Declaration

I hereby declare that this thesis incorporates material that is result of joint research with Derek O. Northwood of University of Windsor, ON; Jiman Han, Qian Zou and Gary Barber of University of Oakland MI, USA; and Xichen Sun and Philip Seaton of Chrysler LLC Technology Center, MI, USA. The collaboration is covered in Chapter 5 and 6 of the thesis. In all cases, the key ideas, primary contributions, experimental designs, data analysis and interpretations were performed by the author, and the contribution of co-authors was in the capacity of the research in the form of technical advice and suggestions

I am aware of the University of Windsor Senate Policy on Authorship and I certify that I have properly acknowledged the contribution of other researchers to my thesis, and have obtained written permission from each of the co-author(s) to include the above material(s) in my thesis.

I certify that, with the above qualification, this thesis, and the research to which it refers, is the product of my own work.

II. Declaration of Previous Publication

This thesis includes one original paper that has been previously submitted for publication in peer reviewed conference proceedings, as follows:

Thesis Chapter	Publication Title / Full Citation	Publication Status
Chapter 5 and Chapter 6	T. Nasir, D. O. Northwood, J. Han, Q. Zou, G. Barber, X. Sun, P. Seaton, Heat treatment – microstructure – mechanical/tribological property relationships in austempered ductile iron, <i>WIT Transactions of Engineering Science</i> , Vol 71, 2011, pp 159-170.	In-press

I certify that I have obtained a written permission from the copyright owner(s) to include the above published materials in my thesis. I certify that the above material describes work completed during my registration as a graduate student at University of Windsor.

I declare that, to the best of my knowledge, my thesis does not infringe upon anyone's copyright nor violate any proprietary rights and that any ideas, techniques, quotations or any other material from the work of other people in my thesis, published or otherwise, are fully acknowledged in accordance with the standard referencing practices. Furthermore, to the extent that I have included copyrighted material that surpasses the bounds of fair dealing within the meaning of the Canada Copyright act, I have obtained a written permission from the copyright owner(s) to include such material(s) in my thesis.

I declare that this is a true copy of my thesis, including any final revisions, as approved by my thesis committee and the Graduate Studies office, and that this thesis has not been submitted for a higher degree to any other University or Institution.

ABSTRACT

This research is on austempered ductile iron (ADI), which offers an excellent combination of low cost, design flexibility, good machinability, high strength-to-weight ratio, good toughness, good wear resistance and fatigue strength. While ADI has found quite wide application in some industries, its use in automotive parts production has been limited. ADI obtains its excellent properties through the development of a high carbon austenite+ferrite microstructure referred to as ausferrite. The properties of ADI can be tailored by changing the heat treatment schedule. In this research a special chemistry Ni-Mo-Cu ADI was subjected to heat treatment schedules. Mechanical properties (hardness, tensile strength, and toughness), tribological properties (scuffing and surface deformation) and microstructural studies were conducted. Feathery ausferrite microstructure produced by high austempering temperature and long time gave very good tribological properties. While martensitic microstructure produces by low austempering temperature and short time gave very high hardness. Heat treatment recommendations were made based on the targeted automotive applications.

DEDICATION

This thesis is dedicated to Dr Derek O Northwood. A truly remarkable man and my beloved and forever respected supervisor.

ACKNOWLEDGEMENTS

First I would like to thank my advisor Dr. Derek O. Northwood for his relentless hard work towards preparing me for my M.A.Sc degree. Also to my committee members Dr Randy Bowers, Dr Jennifer Johrendt and Dr Xichen Sun who provided valuable technical knowledge and facilities for this research.

From the University of Oakland, I would like to acknowledge Jiman Han, Qian Zou and Gary Barber who were the active research partners for a significant portion of this thesis.

From the Chrysler LLC Technology Center, I would like to acknowledge Dr Xichen Sun and Philip Seaton for the testing and ADI casting facilities.

I would also like to acknowledge Mr John Robinson, Andy Jenner, Matt Louise and Lucian Pop for their remarkable support at the University of Windsor labs. Also my dear friend Hao Ma (Mark) for his consultation and software expertise.

Finally I would like to acknowledge Dr Derek O. Northwood and University of Windsor graduate scholarships for funding my M.A.Sc. degree.

TABLE OF CONTENTS

DECLARATION OF CO-AUTHORSHIP / PREVIOUS PUBLICATION.....	iii
ABSTRACT.....	v
DEDICATION.....	vi
ACKNOWLEDGEMENTS.....	vii
LIST OF TABLES.....	xi
LIST OF FIGURES.....	xii
LIST OF ABBREVIATIONS.....	xvi
CHAPTER I : INTRODUCTION.....	1
1.1 Research Scope:.....	2
1.2 Motivation:.....	3
1.2.1 Direct Benefit in Industrial Applications:.....	4
CHAPTER II : LITERATURE REVIEW.....	5
2.1 Cast Irons.....	5
2.1.1 Gray Iron.....	7
2.1.2 Ductile (Nodular) Iron.....	8
2.1.3 White Iron Malleable Iron).....	9
2.2 Austempered Ductile Iron (ADI).....	11
2.3 Alloying Elements in ADI:.....	14
2.4 The Heat Treatment Process of ADI:.....	15
2.4.1 Austenitizing Step:.....	16
2.4.2 Austempering Step:.....	16
2.5 Process Window for Austempering Process:.....	17
2.6 Austenite Decomposition:.....	18
2.6.1 Bainite.....	19
2.6.2 Austenite:.....	26
2.6.3 Martensite:.....	26
2.6.4 Carbide:.....	26

2.7 Thermodynamics of ADI Transformation:	24
2.7.1 Isothermal Transformation Diagram:.....	26
2.8 Alloying Element Segregation in ADI:.....	29
2.9 Mechanical Properties of ADI:	30
2.10 Scuffing Process and ADI Scuffing Research:	33
2.11 Applications of ADI.....	34
2.12 Previous Studies of Particular Relevance:	36
CHAPTER III : EXPERIMENTAL DETAILS	42
3.1 Overview of the Experimental Procedures and Measurements	42
3.2 Material and Casting:	43
3.2.2 Casting Details:	44
3.2.3 As-Cast Samples:	44
3.3 Heat Treatment Design:	45
3.3.1 Austenitizing Temperature Experiment:	45
3.3.2 Austenitizing and Austempering Schedules:	47
3.4 Charpy Impact Testing:.....	48
3.5 Hardness Tests:	49
3.5.1 Surface Hardness:	49
3.5.2 Microhardness:.....	50
3.6 Tensile Testing:.....	51
3.7 Surface Profilometry:	52
3.8 Metallography:	53
3.9 X-Ray Diffraction:	54
3.10 Scuffing Test:.....	55
3.11 Image Analysis:	56
CHAPTER IV : MICROSTRUCTURE CHARACTERIZATION	58
4.1 Austempering Temperature and Time Effect:	58
4.2 Retained Austenite:	66

4.3 Qualitative Microstructure Image Analysis:	68
4.4 Microstructure Summary	70
CHAPTER V : MECHANICAL PROPERTY ANALYSIS	71
5.1 Hardness:.....	71
5.1.1 Microhardness:.....	75
5.2 Toughness:	76
5.3 Tensile Properties:	82
5.4 Mechanical Property Summary.....	84
CHAPTER VI : SCUFFING PERFORMANCE	86
6.1 Metallurgical Examination of Scuffed Samples	91
6.2 Scuffing Summary	94
CHAPTER VII : CONCLUSIONS AND RECOMMENDATIONS	95
7.1 Recommendations for Future Work:	97
REFERENCES	99
PUBLICATIONS AND PRESENTATIONS	104
VITA AUCTORIS	105

LIST OF TABLES

Table 2.1	ASTM Grades for ADI [5, 10]	31
Table 2.2	Tensile properties comparison of ADI, cast irons and steels [2].....	33
Table 2.3	Tensile properties for SAE 8620 steel: normalized material and core properties [2].	26
Table 3.1	Alloy composition of ADI.....	43
Table 3.2	Austenitizing process of initial test samples	46
Table 4.1	Volume % retained austenite for ADI samples.....	66
Table 4.2	Microstructure area % of the ADI samples.	69
Table 5.1	Hardness (HRC) of the as cast and heat treated samples..	72
Table 5.2	Microhardness (HV) of different phases in ADI samples.....	76
Table 5.3	Charpy impact toughness (J) for as cast and ADI samples.....	77
Table 5.4	Average roughness (Ra) of fractured ADI samples..	81
Table 5.5	Tensile properties of the as-cast and austempered samples.	82
Table 6.1	Scuffing load of ADI samples.....	86

LIST OF FIGURES

Figure 2.1	Fe-C phase diagram[13]	6
Figure 2.2	Classification of cast iron [14]	7
Figure 2.3	Optical micrographs of various cast irons: a) Gray iron 500X: Visible graphite flakes are embedded in the α -ferrite matrix. , b) Nodular (ductile) iron 200X: Graphite is in nodular form and surrounded by α -ferrite matrix. [13].Effect of carbon content on the minimum end-quench hardenability of 86xx series of alloy H-steels [19].....	8
Figure 2.4	Optical micrographs of white iron 400X: the light cementite regions are surrounded by pearlite which has ferrite-cementite lamellar structure [13].	9
Figure 2.5	Optical micrographs of malleable iron 150X: graphite are formed as rosettes [13].....	10
Figure 2.6	ADI ausferrite microstructure	12
Figure 2.7	Schematic representation of a) Ductile cast iron, b) ADI.	13
Figure 2.8	Two aspects of ADI production.	14
Figure 2.9	Heat treatment process for ADI [2, 3].....	15
Figure 2.10	Carbon dissolution in austenite during austenitizing step.....	16
Figure 2.11	Process window for austempering[1, 19].....	18
Figure 2.12	Schematic illustration of bainite sheaves and subunits.	20
Figure 2.13	Upper and lower bainite formation [1].....	21
Figure 2.14	Schematic phase diagram of portion of Fe-2.4Si-C system [6].	25
Figure 2.15	Isothermal transformation diagram of Austenite [6].....	25
Figure 2.16	TTT curve for ADI [22]	29
Figure 2.17	Strength comparison of ADI and other ferrous metals [2].....	32
Figure 2.18	Various commercial applications of ADI a.) gears, rotors, bodywork and other machine components[32], b) propellers [11], c)large wheels, shafts, mechanical housing of ADI[33].	35

Figure 2.19	ADI heat treatment, a) conventional austempering, b) 2 step austempering [17].....	37
Figure 3.1	Optical micrograph of as-cast sample.....	45
Figure 3.2	Microstructure comparison of austenitized samples: a)700C, b)740C, c)820C d)900C.....	46
Figure 3.3	Heat Treatment Schedules.....	47
Figure 3.4	ASTM E23 Charpy test diagram.....	48
Figure 3.5	Charpy sample after testing.....	49
Figure 3.6	Rockwell hardness testing machine.....	50
Figure 3.7	ASTM E8-04 Spec [48].....	51
Figure 3.8	Tensile testing equipment a) Tinius-Olsen testing system, b) extensometer, c) broken sample after testing.....	52
Figure 3.9	Stylus surface profilometry a) Measuring unit, b) Digital tray control.....	53
Figure 3.10	SEM equipment.....	54
Figure 3.11	Ball on disc scuffing test equipment.....	56
Figure 3.12	Optical image analysis for graphite nodule percentage. a) original micrograph, b)graphite nodules separated after ImageJ and Photoshop filtering.....	57
Figure 4.1	Optical micrographs of As-cast samples.....	60
Figure 4.2	Optical micrographs of samples austempered at 275°C, a-b) 10 min, c-d) 60 min e-f)150 min.....	61
Figure 4.3	Optical micrographs of samples austempered at 300°C, a-b) 10 min, c-d) 60 min e-f)150 min.....	62
Figure 4.4	Optical micrographs of samples austempered at 325°C, a-b) 10 min, c-d) 60 min e-f)150 min.....	63
Figure 4.5	Optical micrographs of samples austempered at 350°C, a-b) 10 min, c-d) 60 min e-f)150 min.....	64

Figure 4.6	Optical micrographs of samples austempered at 375°C, a-b) 10 min, c-d) 60 min e-f)150 min.	65
Figure 4.7	SEM micrographs of: (a) Medium feathery ausferrite, (b): Highly feathery ausferrite.	66
Figure 4.8	Relation between austempering temperature and % vol retained austenite for 3 different time durations.	67
Figure 4.9	3D plot relationship between %retained austenite and austempering time/temperature.	68
Figure 4.10	Microstructure balance comparison of all the ADI samples..	69
Figure 5.1	Relationship between hardness (HRC) and austempering temperature for 3 different time durations.....	72
Figure 5.2	Relationship between hardness (HRC) and %vol retained austenite.	73
Figure 5.3	3D plot relationship between hardness (HRC) austenite and austempering time/temperature..	75
Figure 5.4	Relationship between Charpy impact toughness (J) and austempering temperatures for 3 different times.	77
Figure 5.5	Relationship between toughness and (a) % retained austenite and (b) hardness.....	78
Figure 5.6	SEM fractographs of charpy specimens of the as-cast sample.	78
Figure 5.7	SEM fractographs of charpy specimens austempered at 275 C, for a) 60 min, b)150 min.....	79
Figure 5.8	SEM fractographs of charpy specimens austempered at 300 C, for a) 60 min, b)150 min.....	79
Figure 5.9	SEM fractographs of charpy specimens austempered at 325 C, for a) 60 min, b)150 min.....	79
Figure 5.10	SEM fractographs of charpy specimens austempered at 350 C, for a) 60 min, b)150 min.....	80
Figure 5.11	SEM fractographs of charpy specimens austempered at 375 C, for a) 60 min, b)150 min.....	80

Figure 5.12	Charpy fracture surface roughness average (Ra) comparison between 60 min and 150 min austempered ADI.	81
Figure 5.13	Tensile strength (MPa) of as-cast and ADI samples at 60 and 150 min austempering.	83
Figure 5.14	Elongation % of as-cast and ADI samples at 60 and 150 min austempering.	84
Figure 5.15	Elongation and tensile strength relation of the samples.	84
Figure 6.1	Comparison of scuffing failure loads.	87
Figure 6.2	Relationship between scuffing load and (a) % retained austenite, (b) hardness and (c) toughness.	88
Figure 6.3	3D plot relationship between scuffing load (N) and austempering time/temperature: a) 1.65m/s sliding speed, b) 1.35 m/s sliding speed. ...	90
Figure 6.4	SEM image in the subsurface micrograph at sliding speed of 1.649m/s (the horizontal arrow shows the sliding direction) for ADI austempered in (a) 325°C/10min, scuffing load=117N; (b) 350°C/10min, scuffing load=125N; (c) 375°C/10min, scuffing load=127N; (d) 275°C/60min, scuffing load=103N; (e) 275°C/150min, scuffing load=117N; (f) 300°C/60min, scuffing load=125N; (g) 325°C/150min, scuffing load=127N; (h) 350°C/60min, scuffing load=169N; (i) 375°C/60min, scuffing load=176N.	93

LIST OF ABBREVIATIONS

AISI	American Iron and Steel Institute
ICAT	Inter Critical Austenitizing Temperature
ASTM	American Society for Testing and Materials
CCR	critical cooling rate
CCT	continuous cooling transformation
CTC	Chrysler LLC Technology Center
DBTT	ductile-to-brittle transition temperature
HRC	Rockwell C Hardness
HV	Vickers Hardness
ID	inner diameter
M_s	martensite start temperature
M_f	martensite finish temperature
UTS	ultimate tensile strength
XRD	x-ray diffraction
YS	yield strength
%EL	percent elongation
%RA	percent retained austenite

CHAPTER I

INTRODUCTION

Austempered ductile iron, commonly referred to as ADI, is an interesting class of cast iron because of its unique microstructure and mechanical properties. It is a member of the cast iron family with a special microstructure, achieved by a combination of alloying elements, and a very precise and controlled heat treatment. A specific compositions of ductile iron are heat treated in two steps to achieve this microstructure, namely an austenitizing step and an austempering step. The goal of these two steps, along with the alloying elements catalytic effect, is to have an optimum combination of the bainitic ferrite and stable austenite. ADI offers the best combination of machinability, toughness, wear resistance, high strength to weight ratio with low-cost design flexibility compared to conventional ductile iron, cast and forged aluminum and many cast and forged steels[1-4].

In 2010, 300,000 tons of ADI were estimated to be used in industrial applications [3]. As it is a cast iron, ADI could be cast like any other ductile iron, thus offering engineers the opportunity to fabricate with a mature and inexpensive technology. The mechanical properties of ADI are superior to ductile iron, cast and forged aluminum, and even many cast and forged steels. For these excellent properties, ADI is a very serious material investigated for new applications. Since ADI has a very complex microstructure balance, it is not often easy for industry to exploit the properties of ADI according to their application. The ADI properties could be tailored within a very wide range of physical, mechanical and tribological properties. An in-depth knowledge of the property relationships with the heat treatment is thus essential for the practical use of ADI.

Researchers are involved in understanding the properties of ADI as it is still a relatively new material in many engineering fields. For this reason, new ideas for ADI applications are emerging all the time. Because of the increasing commercial uses, standards have been established such as ASTM A897 [5], which will encourage further applications of the ADI. The metallurgy of the ADI is an ideal example using the microstructure of a metal to tailor the mechanical and physical properties with the basic understanding of metallurgical kinetics and thermodynamics [6-7].

1.1 Research Scope:

The scope of this research is to develop a heat treatment schedule for a pre-specified chemical composition ductile iron to produce an ADI for automotive applications such as the crankshaft, camshaft and the lower-arm. These three components require different levels of hardness and tribological properties. Hardness levels required are 28, 50 and 40 HRC for crankshaft, camshaft and lower arm, respectively. The crankshaft and camshaft applications require good scuffing resistance as they are subjected to continuous rubbing in their operations. To achieve such various properties, it is important to develop an in-depth knowledge of the mechanical and tribological properties as a function of heat treatment schedule. The key to developing the desired product is to understand the matrix transformations during ADI heat treatment and how the important phases in the microstructure could be produced and stabilized.

To achieve the above mentioned targets, three aspects of ADI were researched in this thesis, namely mechanical, tribological and microstructural properties. All three are a function of the heat treating schedule. Mechanical properties include macro hardness,

phase hardness (micro-hardness), tensile properties, toughness and fracture roughness. Tribological properties included scuffing resistance and surface deformation.

1.2 Motivation:

The application of ADI is a very practical one in the modern industry. The automotive industry, in particular, is constantly evolving and introducing newer and less expensive ways of manufacturing to maintain their position in the face of global competition. Steels and ductile irons are used in almost every aspect of automotive manufacturing such as bodywork, chassis and engine. According to their applications, the metal used has to provide a certain level of performance. For example, the mechanical properties of the metal used in the piston ring would be completely different from the one that used in bodywork. Thus a very wide range of steel/iron types would be necessary to perform their perspective applications.

The mechanical and tribological properties of ADI could be altered over a very wide range just by adjusting the heat treatment parameters. The phases achievable in ADI microstructures include retained austenite, bainitic ferrite, martensite and carbide. With the combination of these phases the ADI could be made very hard or very tough, or in balance, as required for particular applications.

The main advantages on ADI compared to traditional forged or wrought steel are [2-4, 7-11]:

- Twice the fatigue strength compared to conventional ductile irons.
- Exceptional ductility, toughness and fracture resistance.
- The hardness, toughness and ductility level is easily obtainable and can be tailored for any specific application.

- Does not contain embrittling carbides unlike steels which obtain their high hardness from the presence of carbides.
- ADI exhibit superior sliding wear resistance compared to steel and ductile irons.
- Lower fabrication and manufacturing cost due to casting technology compared to steel forgings and cutting processes such as turning, milling, and CNC machining.
- 35% higher tensile strength than steel forgings.
- 10% lower density than steel, which results in significant weight reduction.
- Vibration dampening and heat transfer superior to many cast and forged steels.

1.2.1 Direct benefit in industrial applications:

Cost Benefit: up to 55% reduction in production cost due to casting technology, cheaper material and man-power savings as there is no need for assembly [9].

Weight Savings: up to 15% weight reduction compared to the same part made from steel. This could be attributed to the lower density of ADI and removal of assembly components such as bolts, screws and welds [7, 9].

Performance Benefits: Superior wear, durability and appearance compared to an assembly design. Greater independence to design engineers as all the properties can be varied over a wide range with tailored heat treatment schedules [7, 9].

With ADI's controllable properties by heat treatment, manufacturers will be able to produce all three components with same alloyed ductile iron by simply putting it through different heat treatments. This would be largely beneficial to streamline resource and spending. This is the main motivation of this research thesis.

CHAPTER 2

LITERATURE REVIEW

Although this research is specifically about ADI, it is very important to have a base knowledge of ductile iron and its properties in order to fully understand the ADI research. A brief introduction to ductile iron, its microstructures, and phase diagrams is given first. This is followed by a review of the origins, properties and applications of ADI.

2.1 Cast Irons

Cast Irons are a family of ferrous alloys that possess a wide range of microstructures and physical properties. Fe-C alloys with carbon contents higher than 2.14% are classified as cast irons, while those with lower carbon contents are classified as steel. Cast irons are generally Fe-C-Si alloys that often contain other alloying elements. Up to 10% total of C, Si, Mn, S, and P as well as varying amount of Ni, Mo, Cu and Va are typically present. The matrix microstructure consists of pearlite and ferrite. Cast iron is directly used in the as-cast condition without further heat treatment. In practice, most cast irons have carbon contents between 3.0-4.5 wt%, and other additional alloying elements [12, 13].

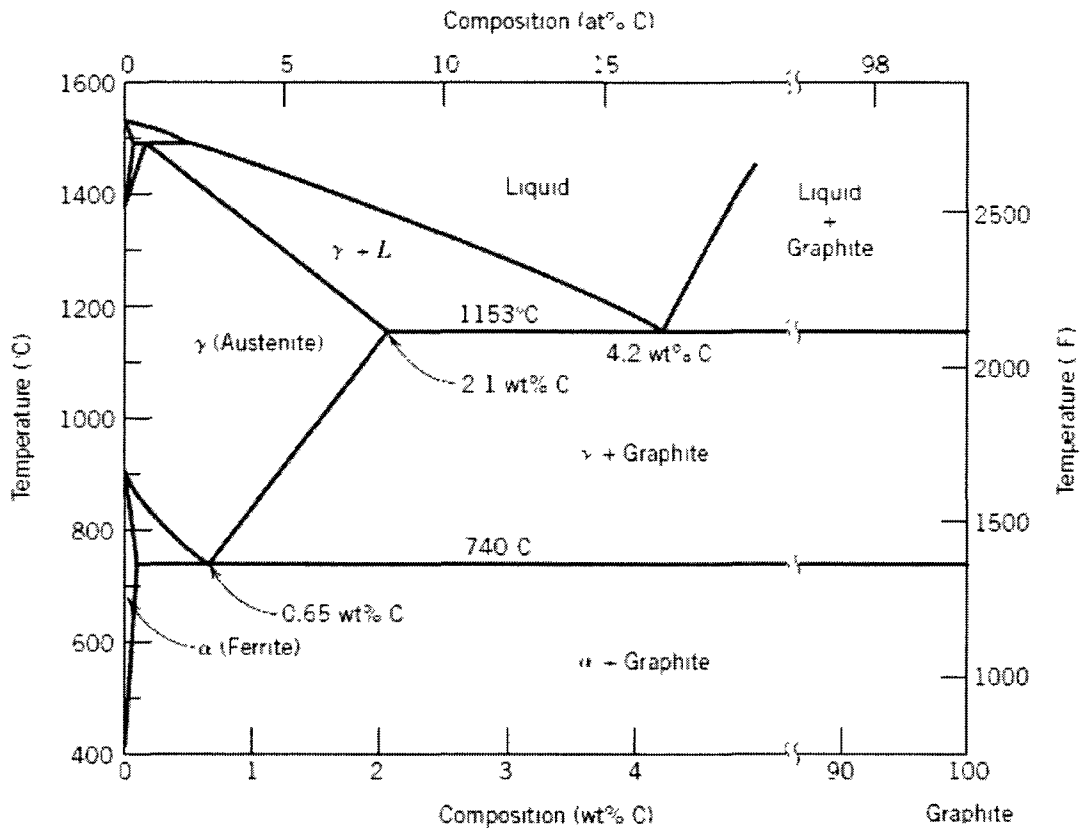


Figure 2.1 Fe-C phase diagram[13]

From the Fe-C phase diagram in Figure 2.1, it can be seen that cast iron completely liquifies between 1150 and 1300°C. This is a significantly lower temperature than for steel, thus cast iron is less expensive and more convenient to melt and fabricate. In fact, cast iron provides a wide spectrum of mechanical properties that can be tailored by just altering some of the processing variables during the heat treatment. For most cast irons, the carbon exists as graphite and the microstructural and mechanical properties and behaviour depend on the composition and heat treatment. The types of cast iron vary over a wide range from machinable gray iron to non-machinable white iron. The major

classifications of the cast iron family are shown in Figure 2.2. The most common types are: gray, nodular, white, malleable and compacted graphite.

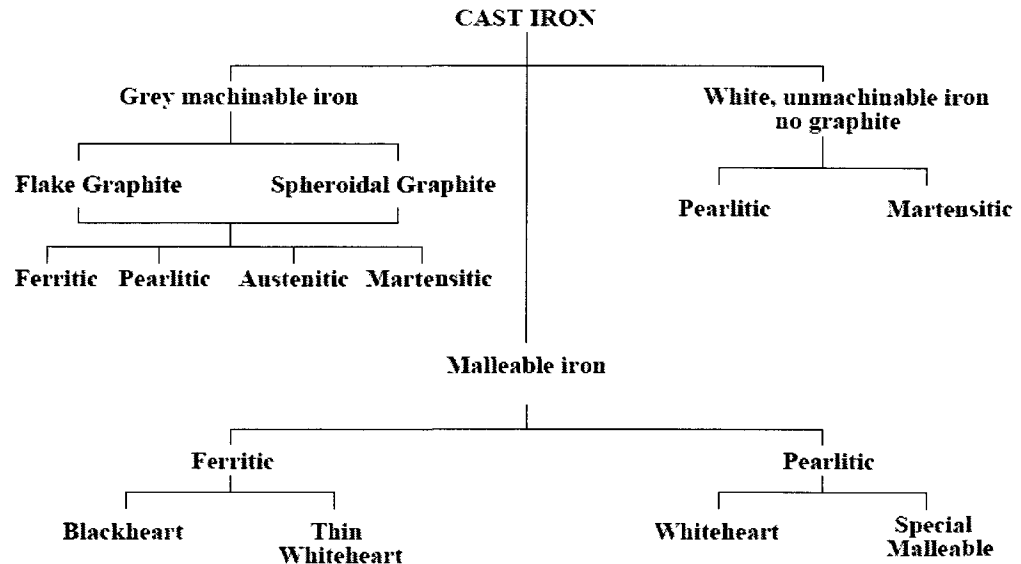


Figure 2.2 Classification of cast iron [14]

2.1.1 Gray Iron

The carbon and silicon contents are between 2.5~4.0% and 1.0~3.0%, respectively, in gray iron. Formation of graphite is common and it exists as flakes, which are surrounded by an α -ferrite or pearlite matrix; see Figure 2.3a. The flakey graphite formation in the iron matrix causes crack initiation and propagation through the sharp flake edges. This makes gray iron generally weak and brittle. The tips of the flakes are sharp and pointed, which could act as crack initiators and propagators under stress in the iron matrix. Gray iron can sustain heavy compressive loads, as the strength and ductility

are much higher under compressive loads. It is very effective for heavy mechanical vibration damping. Gray iron also exhibits high corrosion and wear resistance. In the molten state, gray iron exhibits high fluidity, which is useful in the casting process. Gray iron is the least expensive of all metallic materials [13]. Machines which are subjected to regular vibration and impacts are often constructed of gray iron[12, 13, 15].

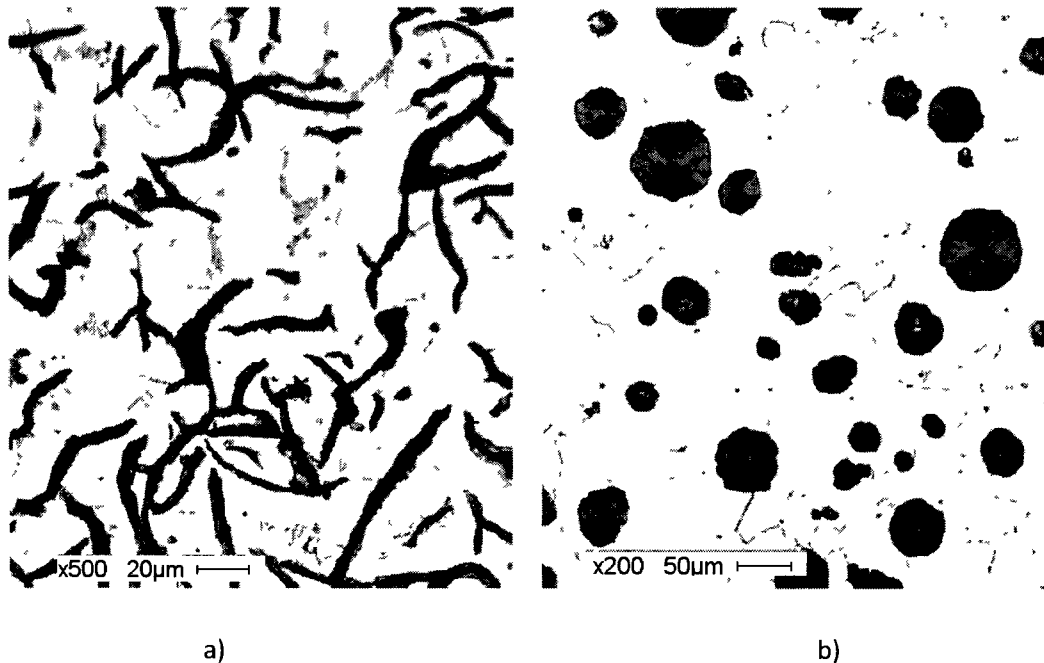


Figure 2.3 Optical micrographs of various cast irons: a) Gray iron 500X: Visible graphite flakes are embedded in the α -ferrite matrix. , b) Nodular (ductile) iron 200X: Graphite is in nodular form and surrounded by α -ferrite matrix. [13].

2.1.2 Ductile (Nodular) Iron

The flakey formation of the graphite in the gray iron could be altered to a nodular shape with small additions of Magnesium (Mg) or Cerium (Ce). A smaller and more nodular graphite formation reduces the localized stress that usually forms on the tip of the flake and increases the ductility of the iron. A typical microstructure of nodular cast iron

is shown on Figure 2.3b. The matrix phase surrounding the graphite nodules could be either pearlite or ferrite, depending on the heat treatment. Ductile cast iron has mechanical characteristics (tensile strength and elongation) comparable to those of steel. Typical applications include valves, pump bodies, crank shafts, gears and other machine components [13].

2.1.3 White Iron

In low silicon cast irons (containing less than 1 wt% Si), which are subjected to rapid quenching, carbon remains as cementite instead of forming graphite. Cementite is a very hard and brittle compound. The presence of cementite makes white iron brittle and un-machinable.



Figure 2.4 Optical micrographs of white iron 400X: the light cementite regions are surrounded by pearlite which has ferrite-cementite lamellar structure [13].

A fracture surface of this type of cementite/martensite phased iron has a white coloured appearance, thus adopting the name white cast iron. An optical micrograph showing the microstructure of white cast iron is shown in Figure 2.4. The light cementite phases are surrounded by pearlite. This white layer could be only surface deep due to the chilled cooling effect, protecting the gray iron underneath, which naturally cools more slowly. Typical applications of white cast iron include hot rollers for steel forming, where a very hard and wear resistant surface without any deformation is necessary [13, 14].

2.1.4 Malleable Iron

Heating white iron at temperatures between 700-900°C for a prolonged time in a neutral atmosphere causes decomposition of cementite into graphite. The microstructure becomes similar to that of nodular ductile iron which accounts for a relatively high strength and a significant ductility. This is called malleable white iron.

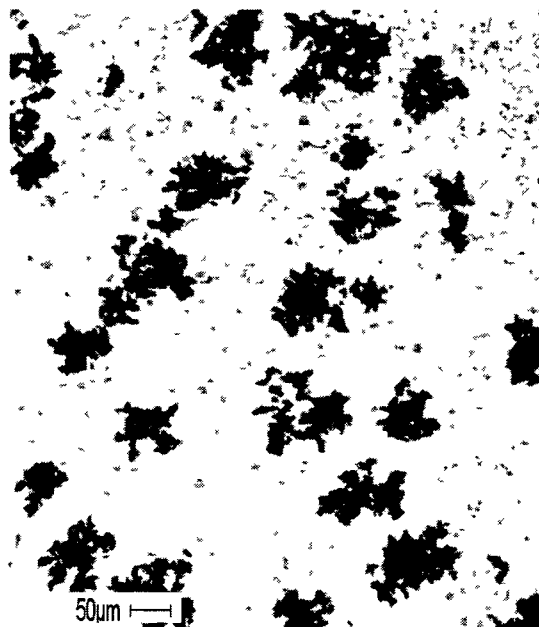


Figure 2.5 Optical micrographs of malleable iron 150X: graphite is formed as rosettes [13].

Figure 2.5 shows an optical micrograph of malleable white iron. Dark graphite rosettes are surrounded by α -ferrite matrix. Major applications for the malleable white iron include connecting rods, differentials, flanges, pipe, valve parts, railroad, and marine and other heavy duty applications[13, 14].

2.2 Austempered Ductile Iron (ADI)

ADI is a grade of iron, in which heat treatment is utilized to produce a metastable face-centered-cubic (FCC) matrix solid solution, austenite, which is stable at room temperature because it is saturated with 1.8-2 wt% carbon [6]. ADI has a very special microstructure made of acicular ferrite and carbon stabilized austenite. Though ADI is sometimes referred as ‘Bainitic Ductile Iron’, correctly heat treated ADI contains little or no bainite. Bainite consists of matrix of a plate-like ferrite and cementite (ferrous carbide), whereas ADI’s matrix is a mix of acicular (plate-like) ferrite laths and stabilized austenite. The acicular ferrite laths are termed as bainitic ferrite. Ferrite lath formations are similar to the cementite in bainite. This mixture of bainitic ferrite in the retained austenite phase is called the *Ausferrite Matrix* [16]. Bainitic ferrite, retained austenite and nodular graphite are the desirable microstructure of the ADI. However undesired phases such as martensite, cementite and other carbides are often present [14].

In Figure 2.6, the ausferrite microstructure of ADI is shown in an optical micrograph. The sheaves/laths are densely packed in a stable austenite (light color) matrix. The dark feathery sheaves/laths are the bainitic ferrite and the light and smooth sheaves are the unwanted α' martensite.

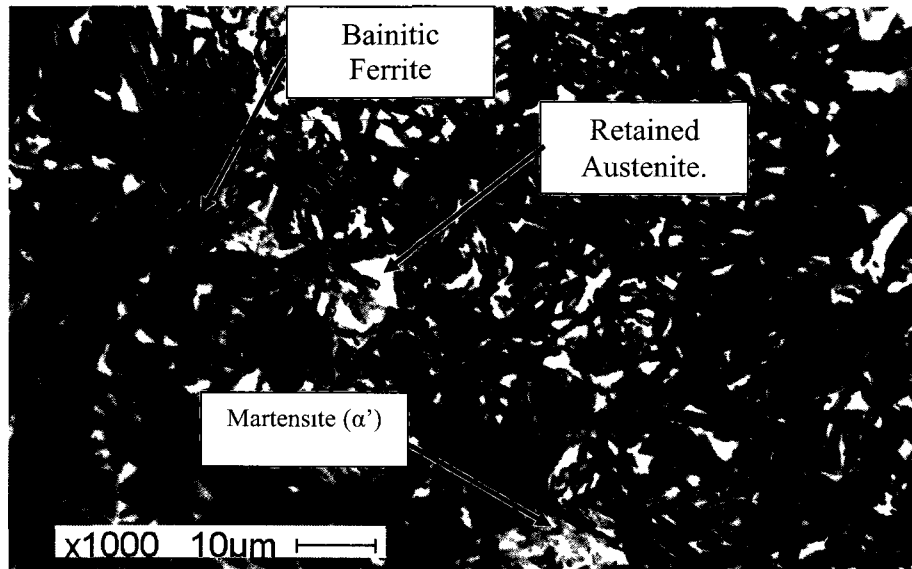


Figure 2.6 ADI ausferrite microstructure

In Figure 2.7 (a) and (b), the microstructures of ductile iron (DI) and ADI are shown schematically and compared. In Figure 2.7 (a), it is seen that the ductile iron is formed of ferrite, pearlite and graphite nodules. Ferrite often surrounds the graphite nodules. But in ADI (Figure 2.7b), ferrite is in the form of feathery sheaves or laths. They are densely packed inside an austenite matrix. Retained austenite usually accumulates in large areas without graphite nodules. Carbide particles often form inside these retained austenite rich areas, which is result of austenite decomposition (further discussion in chapter 2.4.2)

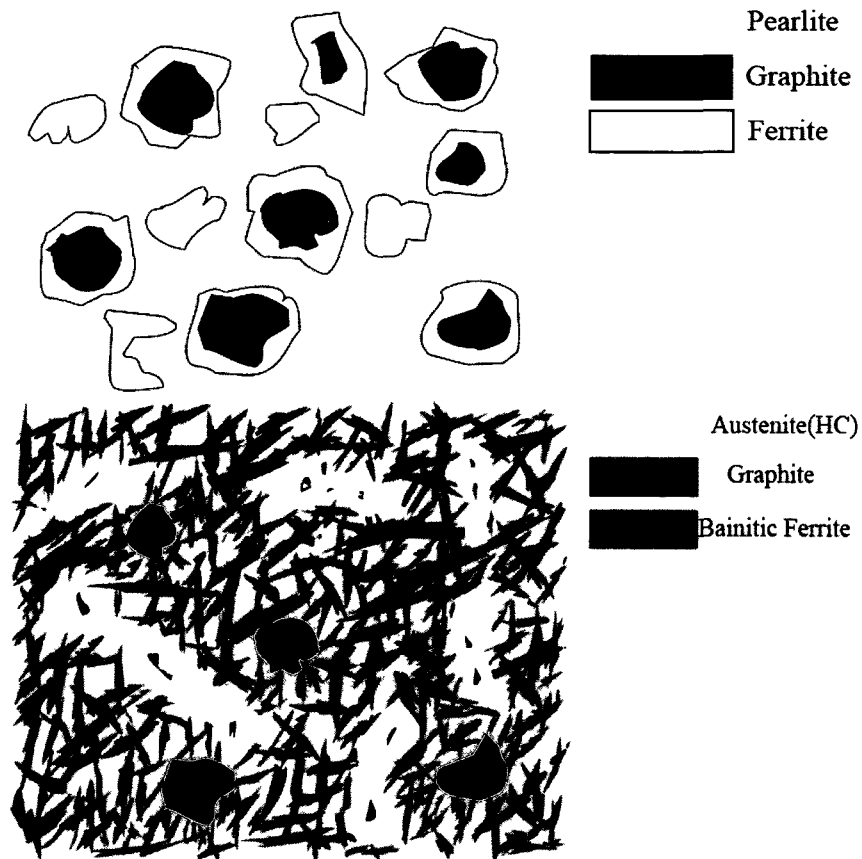


Figure 2.7 Schematic representation of a) Ductile cast iron, b) ADI

The mechanical properties of ADI are dictated by three factors: a. bainite/ausferrite morphology, b. austenite volume fraction, and c. martensite and carbide volume fraction (undesired). The ADI microstructure is produced by the alloying elements and the 2 step heat treatment process; see Figure 2.8.

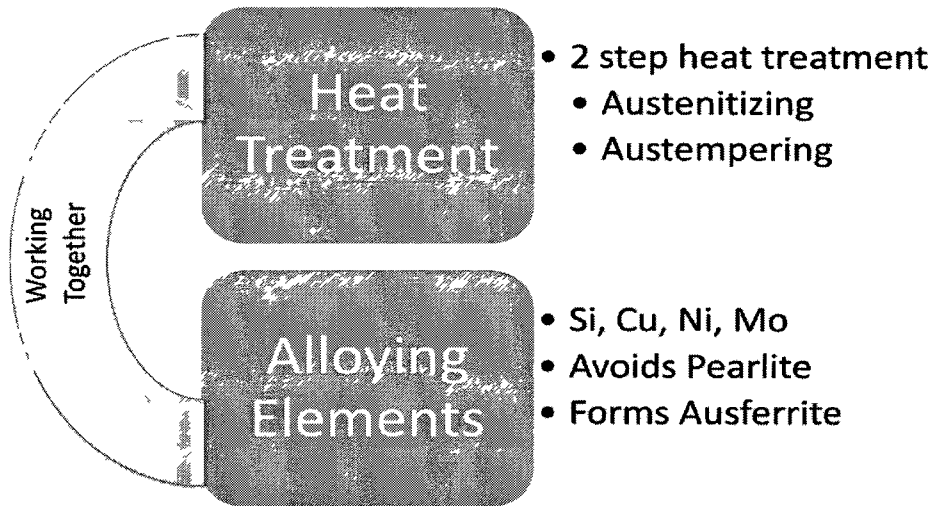


Figure 2.8 Two aspects of ADI production.

2.3 Alloying Elements in ADI:

The composition of ADI differs from conventional ductile irons. Typical alloying elements in ADI are: Carbon (C), Silicon (Si), Manganese (Mn), Copper (Cu), Nickel (Ni) and Molybdenum (Mo). The selection of these elements is done primarily to improve the cast quality by preventing non-spheroidal graphite or carbide formation or by promotion of shrinkage. The presence of a large amount of silicon suppresses the precipitation of carbides during the austempering process and retains a substantial amount of the stable high carbon austenite. Nickel, copper and molybdenum improve the hardenability of ADI quite significantly without the formation of pearlite [4, 16, 17]. Another crucial effect of the alloying elements is to prolong the process window. The process window is discussed in Section 2.5.

2.4 The Heat Treatment Process of ADI:

The development of the ADI heat treatment process can be traced back to 1930, when the austempering process was introduced. Through the evolution of metal, ductile iron was invented in 1948, and the austempering process for ductile iron was developed in the 1950s. In the 1970s, the austempering methods for ductile iron were being industrially developed and used [16].

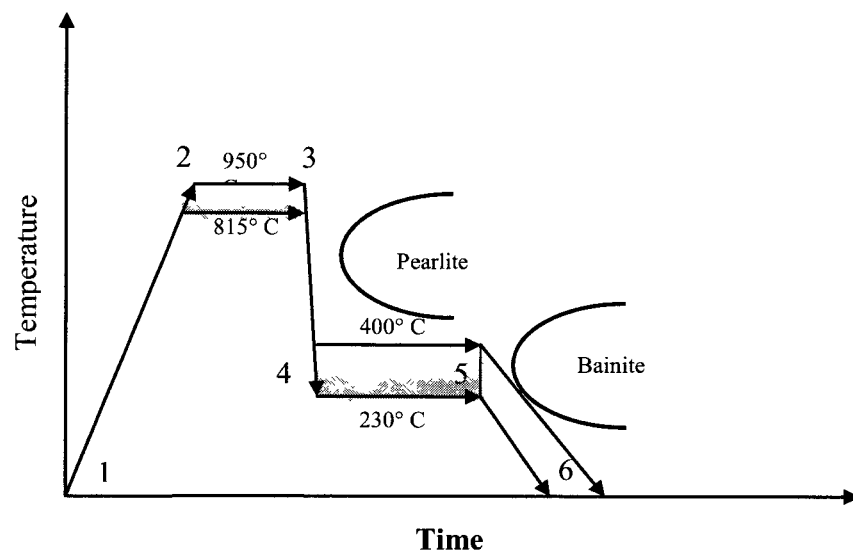


Figure 2.9 Heat treatment process for ADI [2, 3]

The ADI heat treatment process is precisely controlled and it is illustrated schematically in Figure 2.9. Heat treatment is composed of two precisely controlled steps, namely the austenitizing step and the austempering step.

2.4.1 Austenitizing Step:

Ductile iron with ADI composition is first heated to the austenitizing temperature (step 1-2). This is usually from 800 to 950°C where Fe ions assume the FCC crystal structure thus transforming to γ -austenite. The austenitizing temperature is maintained to dissolve some carbon from the graphite nodules in austenite, and also to uniformly dissolve the alloying elements in the γ -austenite (step 2-3). The austenitizing temperature and duration is controlled to ensure the formation of austenite grain and uniform carbon content in the matrix. Figure 2.10 shows the carbon dissolving in to the austenite during the austenitizing step.

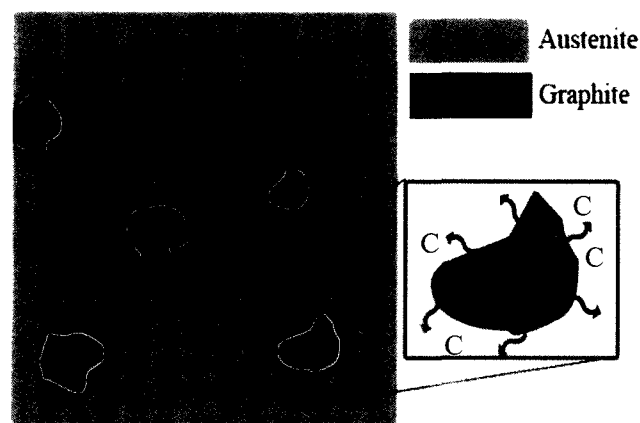


Figure 2.10 Carbon dissolution in austenite during austenitizing step.

2.4.2 Austempering Step:

The austenitized material is then quenched (step 3-4) and held (step 4-5) at the 'austempering' temperature. This temperature is slightly higher than the martensite start temperature (M_s). The quenching must be very rapid (within seconds), to avoid pearlite formation around the carbon nodules. The austempering time is also closely monitored

and controlled to avoid over or under processing. The range of austempering temperatures and times are typically 240°C-400°C and 30-240 minutes, while the martensite start (Ms) temperature is usually 220-250°C depending on the ADI composition[6].

During austempering, ductile iron undergoes two stages of transformations. In first stage, the austenite decomposes into ferrite and high carbon austenite, shown in **Equation 2.1**. This is the desirable stage of the transformation.



If the austempering is maintained too long, then the next stage of transformation occurs as given in **Equation 2.2**, where carbon austenite further decomposes into ferrite and carbide. This is undesirable and causes embrittlement from carbides[18, 19].



The treated metal is then allowed to cool down to room temperature (step 5-6).

2.5 Process Window for Austempering Process:

The transition time between stage 1 and stage 2 transformations is called the process window, see Figure 2.11. From the figure it is seen that the ausferrite transformation is completed at the end of the stage 1. During process window, the ausferrite level remains stable and only starts to decrease with commencement of stage 2 [17]. It has been established that the best mechanical properties of ADI (strength and ductility) are obtained by completing the stage 1 reaction completely, but before the onset of the stage-2 reaction. Thus, it is important to have a sizable process window which will allow the heat treatment process to stabilize so the system does not enter stage 2. As

mentioned earlier in section 2.3, one of the major purposes of the alloying elements is to prolong this process window time period. Alloying elements such as Ni, Co, Mo help expand the process window, to ensure optimum austempering. Mn on the other hand, contracts the process window[14, 17, 20].

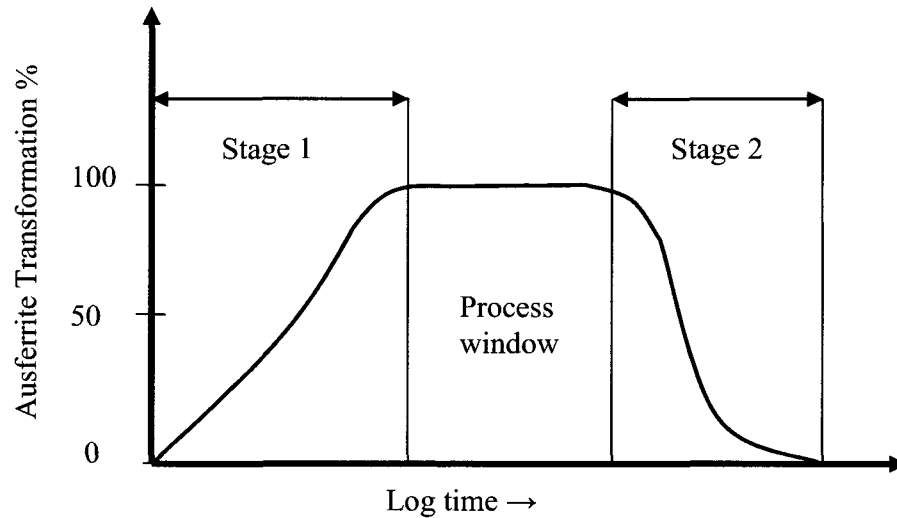


Figure 2.11 Process window for austempering[1, 19].

2.6 Austenite Decomposition:

Austenite decomposition is the most important step in ADI microstructure formation. ADI production is basically controlled decomposition of austenite. Heat levels are precisely controlled to tailor the transformation to achieve the desired ADI microstructure. A thorough understanding of the austenite decomposition kinetics is thus important for ADI knowledge development.

The common types of transformation that take place during the austempering are bainite (bainitic ferrite), retained austenite, martensite and carbides[1]. Although martensite and carbides trend to reduce ductility and toughness, it is difficult to completely avoid formation of these phases during the heat treatment.

2.6.1 Bainite:

Bainite is one of the common austenite decomposition products. Bainitic ferrite and austenite mixture is the most important feature of the ADI microstructure. The bainite microstructure consists of consecutive layers of ferrite plates, separated by thin films. These thin films could be of cementite, martensite or austenite. In conventional bainite, these films are cementite, which forms in conventional steels and low silicon ductile iron [13]. But for ADI and some high silicon steels, cementite films are not found in the bainite, but they are replaced by a carbon-enriched, stable austenite. This formation is called bainitic ferrite. The ferrite aggregate plates are often referred to as sheaves or laths [1]. The smaller ferrite plates that exist within larger sheaves are often termed as subunits [1, 14], as seen on Figure 2.12. These sheaves and subunits are related to each other by a specific crystallographic orientation. The very first ferrite subunit that nucleates on the grain boundary achieves a particular size, and then successive plates stack up to build a single sheaf. Although the subunit plates are adjacent to each other, they are isolated by 'yet to be' transformed austenite films. As the cooling continues, the separator films can transform into martensite or cementite under certain conditions.

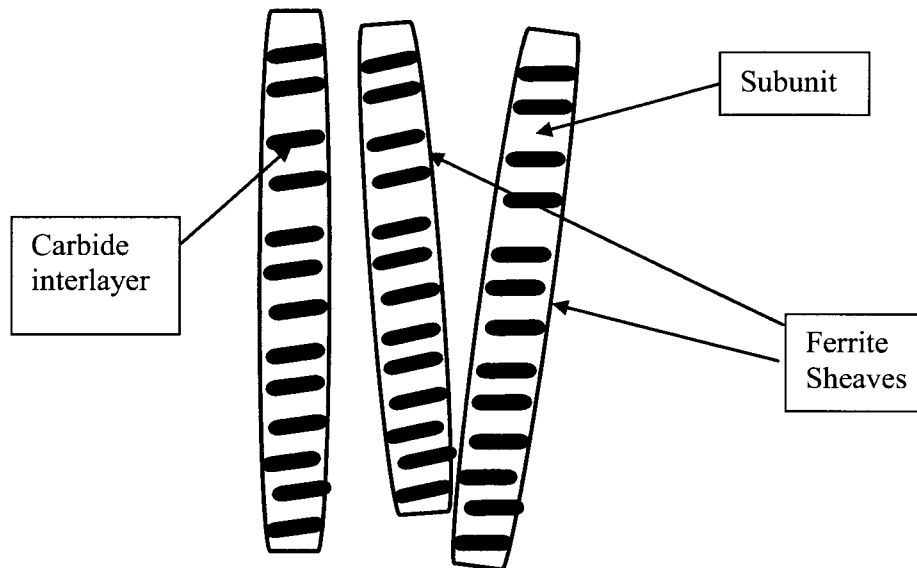


Figure 2.12 Schematic illustration of bainite sheaves and subunits.

Bainitic ferrite can exist in two different forms: *upper* and *lower* bainite. Upper bainite forms well above the martensite start temperature (M_s). In some ductile irons and steels, most of the carbides are present within the bainitic sheaf interface, rather than subunit-subunit interface. In other words, in upper bainite, the sheaves are made of uniform ferrite, without subunits. Whereas in lower bainite the sheaves are stack of subunit ferrite layers. The upper and lower bainite formation mechanisms are illustrated in Figure 2.13 [1].

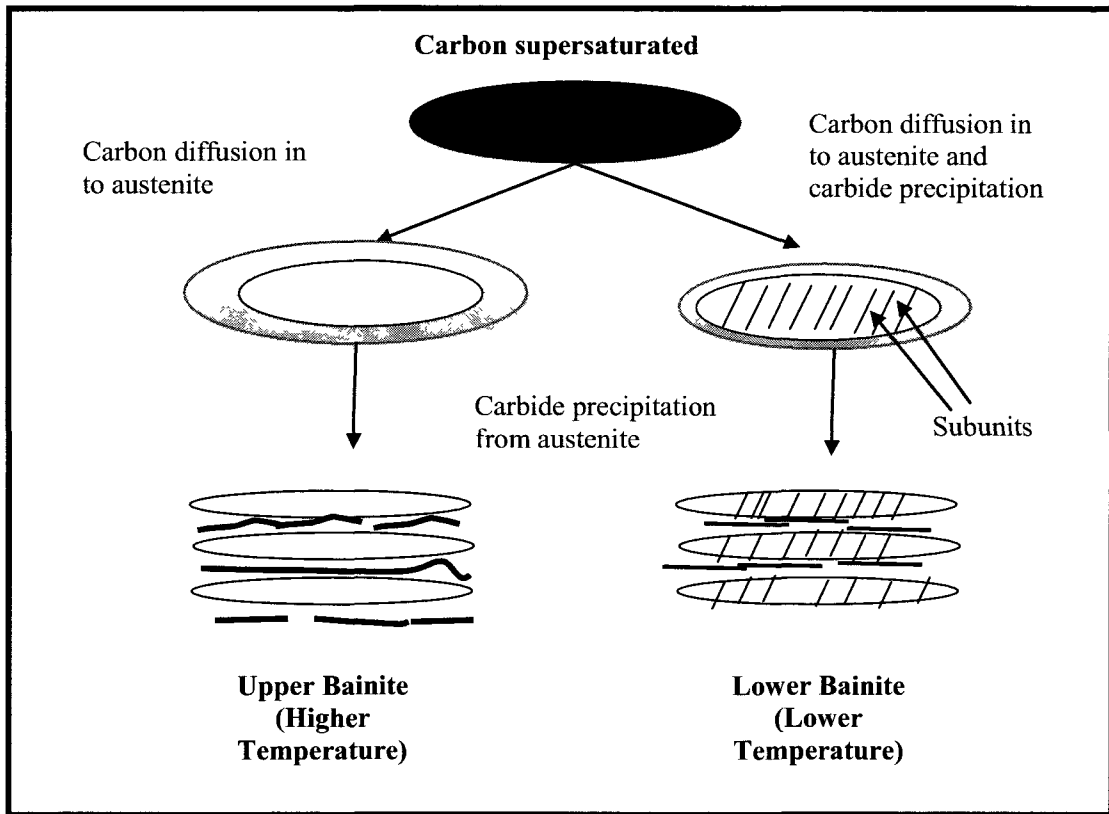


Figure 2.13: Upper and lower bainite formation [1].

Typically, lower bainite forms in high carbon steel and ductile irons below the temperature where upper bainite forms, but above that of the martensitic start temperature (M_s). There are many similarities in the lower bainite and martensite microstructure. The main difference is that in lower bainite, only one crystallographic variant of the carbide exists, whereas in martensite the tempered martensite shows multiple crystallographic variants. In some steels, the lower bainitic ferrite has ϵ -carbide, instead of cementite. In summary, it is important to understand that both upper and lower bainite are transformations of austenite. In the case of upper bainite, the carbon from a bainite subunit transforms into an austenite grain before the carbide precipitates within subunits.

And in the case of lower bainite, carbon precipitates within the subunits before carbon is transferred to the interlayer of the sheaves.

The ferrite growth is typically discussed based on either a reconstructive or a displacive transformation of austenite mechanism. One growth definition (reconstructive) claims the bainite growth is result of diffusional, non-cooperative and competitive growth of ferrite and cementite into the austenite during eutectoid composition with cementite appearing in non-lamellar form. In this definition, the transformation kinetics are related to the rate of ledge movement at the ferrite-austenite interface and it is controlled by the carbon diffusion. However, the displacive definition claims that a subunit of a ferrite is formed from the austenite with complete super-saturation of carbon through a displacive transformation [1, 13, 14].

2.6.2 Austenite:

Retaining high-carbon austenite is one of the prime targets during the austempering process. Alloying elements such as Si, Cu, Ni, Mo help avoid pearlite formation and retain γ -austenite. The difference between the austenite developed in the austenitizing step and the retained austenite is the carbon content. Austenite is not stable at room temperature because of its FCC crystal structure. But carbon saturated austenite can be stable at room temperature. In stage 1 of the austempering process, the parent austenite transforms into ferrite and high-carbon retained austenite. Carbon dissolves in residual austenite, producing “carbon-free” ferrite as upper-bainitic ferrite. This reduces the driving force for further decomposition. A portion of the *residual austenite* decomposes at the isothermal transformation temperature. The un-transformed *residual austenite* which remains stable at room temperature is the *retained austenite*. When

discussing the microstructure, it is important to differentiate between the residual austenite, which exists at the isothermal transformation temperature, and the retained austenite, which remains un-transformed even at room temperature[1, 13, 14].

2.6.3 Martensite

Martensitic transformation occurs below the M_s temperature. It is formed through a displacive transformation of austenite. Martensitic transformation is an athermal process (below M_s), which means that the extent of transformation depends how much below the M_s it is undercooled, but it is independent of the time duration spent below M_s . The transformation takes place as soon as the temperature dips below M_s and continues till the martensite finish temperature, M_f . If M_f is well above room temperature, then 100% martensitic transformation is expected on cooling. But if M_f is below room temperature, then some austenite may be retained if only cooled to the room temperature. Experimental evidence suggests that the martensite assumes a BCC crystal structure from austenite (FCC crystal structure). This is a displacive process, but BCC is not achievable by just one displacement. It requires two levels of shear displacement and then an inhomogeneous lattice invariant strain. In three steps the FCC crystal structure of austenite transforms into a BCC martensitic crystal structure [13, 21].

2.6.4 Carbide:

Carbon often forms carbides with Fe or other metallic elements present. Silicon hinders carbide precipitation during the austempering process. Prolonged austempering takes the process to *stage 2* where the high carbon residual austenite releases further carbon, which precipitates as carbides. Carbides are extremely detrimental to mechanical

properties. For best mechanical performance of ADI, the formation of carbides must be eliminated or minimized[19].

2.7 Thermodynamics of ADI Transformation:

The ADI transformation thermodynamics can be understood using a common ductile iron phase diagram for a Fe-C-2.4 Si ductile iron, which is the most common iron: see Figure 2.14. The most important features of this ductile iron phase diagram which can explain the ADI metallurgy include:

(I) Martensite start temperature (M_s , the temperature below the ductile iron must be quenched to obtain hard and brittle martensite microstructure).

(II) Extension of the $(\alpha+\gamma)/\gamma$ field boundaries (in the dotted line), which creates a metastable two phase $\alpha+\gamma$ field, where the carbon content of the austenite γ is quite high at low temperatures.

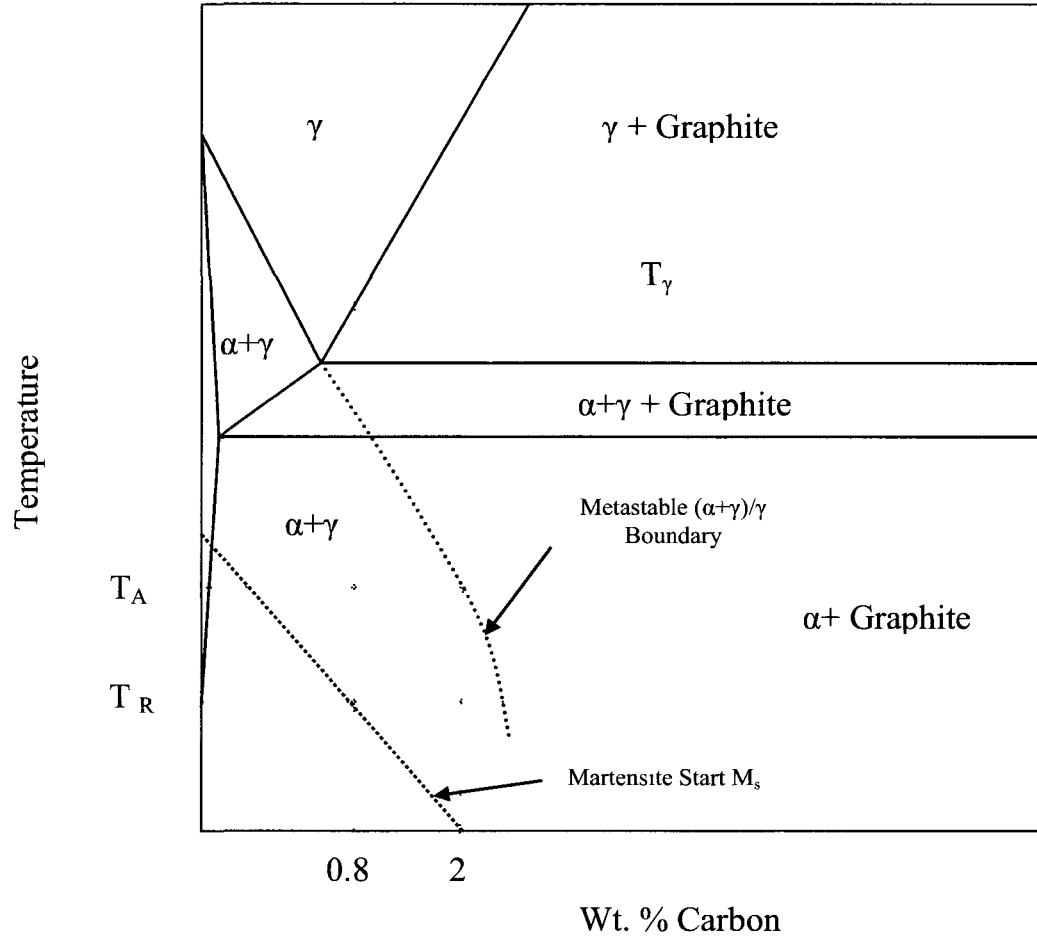


Figure 2.14: Schematic phase diagram of portion of Fe-2.4Si-C system [6]

(I) M_s Temperature: The M_s temperature line according to the Figure 2.14 shows that as the carbon content increases in the austenite, the martensite transformation start temperature is lowered. Austenite with 0.8 wt% will begin the martensite transformation above room temperature T_R , but if the austenite had 2 wt% C, the martensite transformation will not begin until the temperature is at 0°C.

(II) Metastable extension of the $(\alpha+\gamma)/\gamma$ phase boundary: The phase boundary between the $(\alpha+\gamma)$ and γ fields from the top-left area of Figure 2.14 has been extended in the dotted line with thermodynamic considerations. This dotted lined are helps explain the austenite transformations in ADI in a very practical way. If we assume 0.8 wt% C austenite is quenched rapidly to the austempering temperature of T_A , there will be no time for carbon diffusion to occur in the pearlitic transformations. Importantly, this T_A must be above the M_S line as shown in the diagram to avoid any martensite formation[6].

2.7.1 Isothermal transformation diagram:

An isothermal transformation diagram for austenite, which illustrates the possibilities of forming common phases during the isothermal quenching is shown on Figure 2.15. This diagram is derived based on the knowledge on the Fe-C phase diagram and ADI transformation kinetics. The diagram shows the kinetic mapping of the austenite transformation during the quenching and holding. The quenching from T_γ to T_A ideally would be a straight line, as it is desired to be instantaneous. This is because an instantaneous quench process would ensure the fastest cooling rate, which is necessary for acicular ferrite formation and to avoid pearlite formation. But as seen on the diagram, it is often a curved line, as the inner section of the casting is harder to rapidly cool.

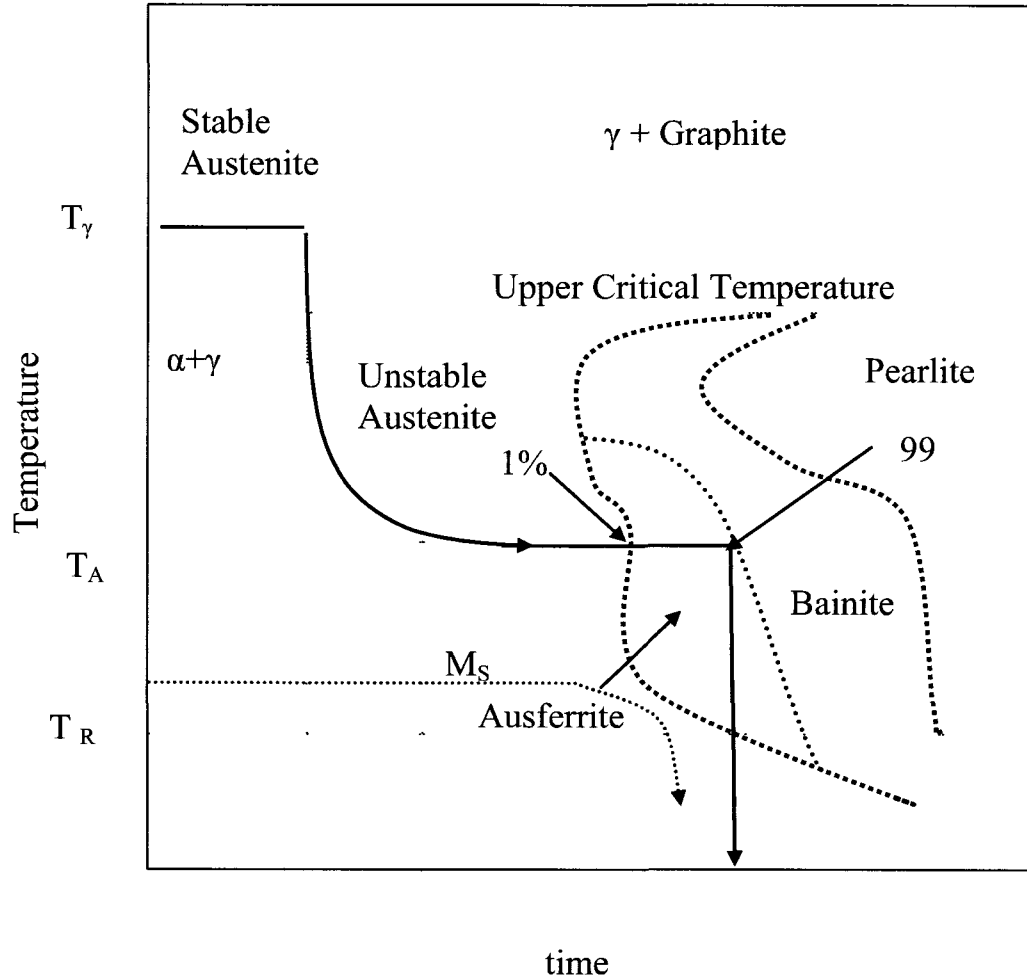
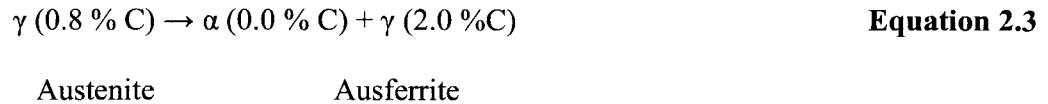


Figure 2.15: Isothermal transformation diagram of Austenite [6]

Consider a typical heat treatment process of 2.4 Si-3.6 C ADI on Figure 2.15 . The casting is heated up to the austenitizing temperature T_γ where the austenite is stable. This point the austenite matrix contained 0.8 wt% C in addition to the graphite nodules. A rapid quench to T_A , austempering temperature and a hold to T_A would initiate the following transformations shown in Equation 2.3:



During this transformation reaction, ferrite nucleates on the graphite nodules or on the austenite grain boundaries. BCC ferrite can only retain a very small amount of carbon and carbon is rejected to the austenite which now contains a very large amount 2.0 wt% C. This reaction usually takes 1-2 hours. Prolonged austempering takes the transformation system to the bainite phase where further carbon release by the enriched austenite occurs and Fe₃C carbides are formed. In steels, the bainitic transformation is very common but the large amount of silicon Si present in ADI suppresses carbide formation. Because the austenite is consuming the carbon from the matrix and becoming more and more carbon enriched, from Figure 2.15, we can see that the M_s will also decrease[6]

A general TTT curve for ADI heat treatment is shown on Figure 2.16. It can be seen that the ADI cooling starts from the upper critical temperature. Austempering takes place well above the M_s temperature. Upper bainite and retained austenite (ausferrite) is formed in the stage 1 transformation, and quenching to room temperature begins before entering stage 2.

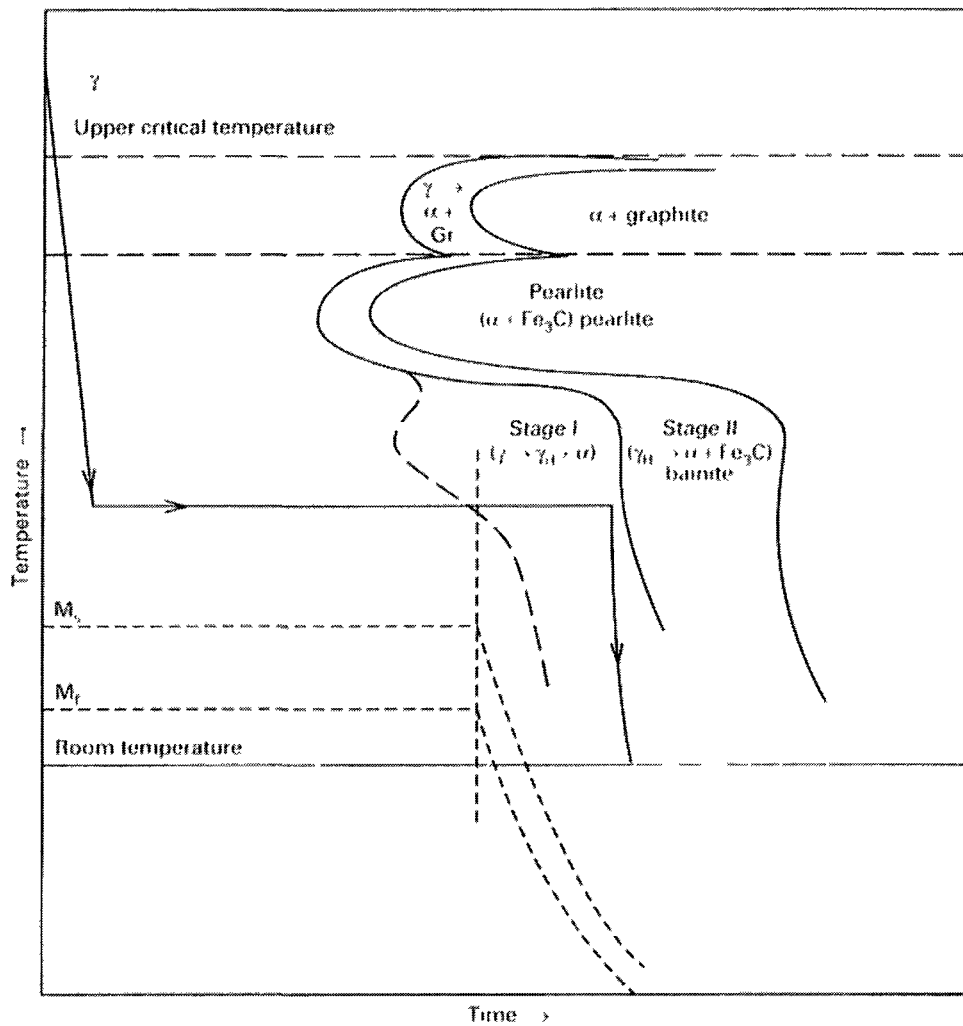


Figure 2.16: TTT curve for ADI [22]

2.8 Alloying Element Segregation in ADI:

Alloying element segregation could take place during both the austenitizing and austempering processes which strongly influences the microstructure, and the effectiveness of the alloying elements. Consequently alloy segregation could reduce the process window and increase carbide precipitation with a large reduction in mechanical properties. This segregation is due to the effect of manganese (Mn), phosphorus (P) and molybdenum (Mo). With increasing amounts of manganese (Mn), mechanical properties

such as yield and tensile strength, and elongation decrease because of the formation of intercellular embrittling regions due to a strong segregation effect. Alloying elements like molybdenum and manganese segregate strongly in the intercellular region prompting carbide formation and thus interfering with the austempering reactions in these areas. Hence, it may be possible to improve the mechanical properties including fracture toughness of ADI by eliminating molybdenum and keeping the manganese content as low as possible [20].

2.9 Mechanical Properties of ADI:

The use of ADI is exponentially growing around the world as the manufacturers keep discovering the excellent combination of properties of ADI. The performance achieved is made even more attractive due to the fabrication simplicity and relatively lower cost compared to steel. The mechanical properties of ADI with a high carbon retained austenite matrix are much superior over other normal grades of cast ductile iron, where Fe is present in the body-center-cubic (BCC) phase. The established reasoning behind this remarkable toughness and hardness combination is due to the presence of the FCC crystal structure in the retained austenite and the ferrite and carbide distributions in that FCC matrix. The FCC metals are known for having more ductility compared to any other crystalline metals. Metals such as copper, aluminum, gold and silver all have the FCC crystal structure which is highly ductile and malleable[6]. Austenitic steels which are capable of a deep-drawing process are also highly ductile compared to other ferritic steels.

A range of mechanical properties can be obtained with ADI. On one end, the ASTM grade I, where it is merely austenite phase with graphite nodules. This material

represents the most ductile and machinable ADI with low surface hardness. At the other extreme of the spectrum is ASTM grade V, containing an austenite matrix with embedded carbide, bainite and martensite representing the least ductile and machinable of the ADIs and highest surface hardness. In between are the other grades of the ADI. The ASTM specification A897 is now the most commonly accepted specification for Austempered Ductile Iron [2, 9, 10]. The five grades specified are detailed in **Table 2.1**:

Table 2.1: ASTM Grades for ADI [5, 10]

AUSTEMPERED DUCTILE IRON					
ASTM A897 - 06					
Grades	ADI Grade	Min. Tensile (psi)	Min. Yield (psi)	Elongation (%)	Typical HB(Brinell)
125-90-09	1	125,000	80,000	10	269 - 341
150-110-07	2	150,000	110,000	7	302 - 375
175-125-04	3	175,000	125,000	4	341 - 444
200-155-02	4	200,000	155,000	2	388 - 477
230-185-01	5	230,000	185,000	1	402 - 512

Like other ductile iron specifications, ASTM A897 defines the minimum tensile properties for grades of ADI. From Table 2.1, it can be seen that the lower grades have a higher elongation up to 10%, while having lower tensile strength. Higher grades have higher hardness, but reduced the elongation.

A comparison of where the ADI grades stand relative to cast irons and steel is shown in the commercial information provided in Figure 2.17 and Table 2.2.

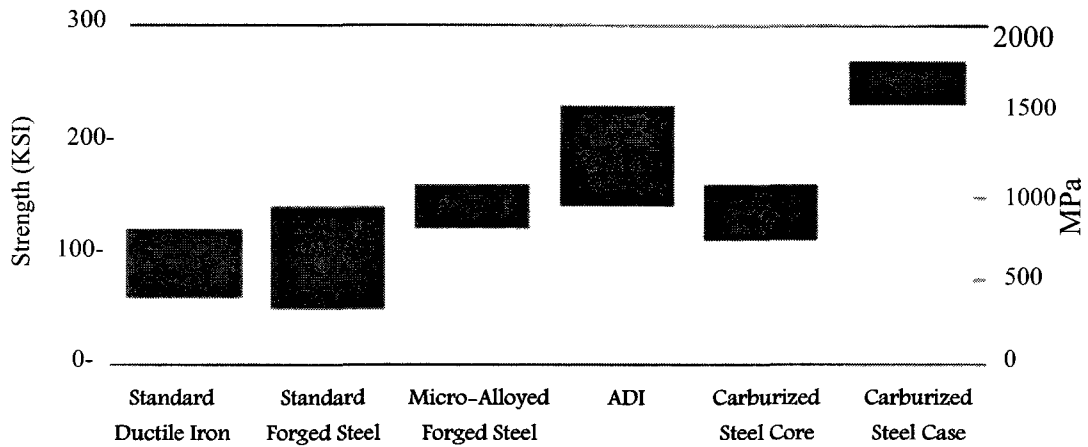


Figure 2.17: Strength comparison of ADI and other ferrous metals [2].

It can be seen from Figure 2.17 that the strength of the ADI is higher than most other steels and ductile irons, and considerably higher than the standard ductile iron and forged steel. Also notable, ADI has the widest range compared to all other entries in the diagram. The only entry with higher strength is the carburized steel case which has a very narrow range.

From Table 2.2, it can be seen that tensile properties of ADI of all the grades are much higher than cast irons, especially the yield strength. When compared to cast steel, all grades of ADI possessed higher tensile and yield strength. While forged steel only has a higher tensile and yield strength range than Grades I and II ADI. Elongation for cast and forged steels and malleable and ductile iron is higher than ADI Grades.

Table 2.2: Tensile properties comparison of ADI, cast irons and steels [2]

	ADI					Cast Irons			Steels	
	Grades					Gray A48	Malleable A602	Ductile A536	Cast A27	Forged A290 A-D
	1	2	3	4	5					
Tensile (10³ psi)	125	150	175	200	230	20-60	50-105	60-100	60-70	80-170
Yield (10³ psi)	80	100	125	155	185	-	32-85	40-70	30-40	45-145
Elongation %	10	7	4	1	N/A	<1	10-1	18-3	24-22	22-10

2.10 Scuffing Process and ADI Scuffing Research:

Tribology studies are also part of this research. A brief discussion of scuffing mechanisms and ADI scuffing research is thus necessary.

As noted by Qu et al. [23]: “The term ‘scuffing’ has been used to describe surface damage in various contexts throughout the field of engineering”. Scuffing is associated with a sharp rise in friction and surface temperature, usually accompanied by a rise in noise and vibration [24, 25]. There has been no general agreement on a definition for scuffing. This has, to a large extent, been due to the complexity of the process. However, one definition that has captured many of the features of scuffing is: “Scuffing is a form of sliding-induced contact damage to a bearing surface, usually associated with asperity-scale plastic deformation that results in localized and perceptible changes in roughness or appearance without significantly altering the geometric form of the part on which the damage occurs [23].”

Usually scuffing damage is catastrophic and not self-healing so that the scuffed part must be replaced. Scuffing may be delayed or prevented by selecting materials with appropriate microstructure and hardness. However due to the complexity of the scuffing process, there is a need to conduct a variety of experiments to better understand the scuffing mechanism, and to evaluate the influence of material microstructure and hardness on scuffing.

Significant research have been carried out on the tribological behaviour of ADI [26-28], but few have examined scuffing. Magalhães and Seabra [29] found that heat treating to produce a material that is simultaneously strong and ductile, helps resist scuffing. However there is limited published research on the effect of heat treatment on the microstructure, mechanical and tribological property relationships. The present research examines the effect of heat treatment schedules on the microstructure, hardness, toughness and the scuffing properties of a Ni-Cu-Mo ADI alloy and develops microstructure-property relationships.

2.11 Applications of ADI

The present applications of ADI include [2, 7-11, 26, 30, 31]:

- Agriculture- excellent resistance to soil wear: Suspensions, ground engaging equipment, tractor wheels.
- Soil cutting machines and tools: digger/grab teeth, high strength and wear resistance.
- Automotive: chassis, crankshafts, camshafts, pinion and ring gear pairs, timing gears for diesel engines.

- Heavy Trucks: spring hanger brackets, pivot pins, clip plates, engine mounts, connecting rods etc.
- Railroads: side bearing top caps, truck plates, rail braces suspension components.
- Industrial: components subjected to wear and high stress.
- Gears: wear resistance and vibration damping ability better than steel.
- Construction: crushing, grading and wear components.
- Food and feed milling: grinding, mixing. Crushing machines.

The various uses of ADI are illustrated in Figure 2.18.



Figure 2.18: Various commercial applications of ADI a.) gears, rotors, bodywork and other machine components[32], b) propellers [11], c)large wheels, shafts, mechanical housing of ADI[33].

2.12 Previous Studies of Particular Relevance:

This section discusses a few of the key papers from previous ADI research that are particularly relevant to the current research.

The austempering schedule determines the microstructure formation and thus the mechanical properties of ADI. Ausferrite, martensite, bainite and carbide form at different times and temperatures during austempering. Much research has been conducted over the last decade exploring the effects of a wide range of austempering schedules on various ADI compositions.

Researchers generally selected an austempering temperature in the range from 300 to 410°C. Below this temperature range, the ADI transformation is near the martensite-start, M_s , temperature, where the microstructure becomes martensitic or lower bainitic, which is often brittle and weak. Kim et al [34] found in their research with Cu-Mo alloyed ADI that was austempered over the range of 350 to 410°C, that a higher austempering temperature produced a higher ductility. Tensile strength was found to be highest for austempering at 350°C. Eric et al [4, 35] in their research with a Cu-Ni-Mo ADI found that the microstructure and the mechanical properties varied greatly with austempering temperature in the range 320 to 400°C. The highest volume fraction of ausferrite and retained austenite was developed by austempering at 320°C. This produced the highest impact energy of 133J. When austempering at 400°C, blocky austenite and martensite were formed which resulted in tensile and Charpy properties approximately equal to those for 320°C austempered specimens.

Stepped austempering possibilities have been explored by a number of researchers in the ADI field. Whereas in conventional austempering, the austempering temperature is

kept constant through the austempering duration, in the stepped process, the ADI samples are austempered usually at a lower than conventional austempering temperature for a short amount of time (step 1), and then the temperature is elevated (step 2) to a temperature similar to conventional austempering temperature. The two step process has a large influence on the microstructure and mechanical property development of the ADI.

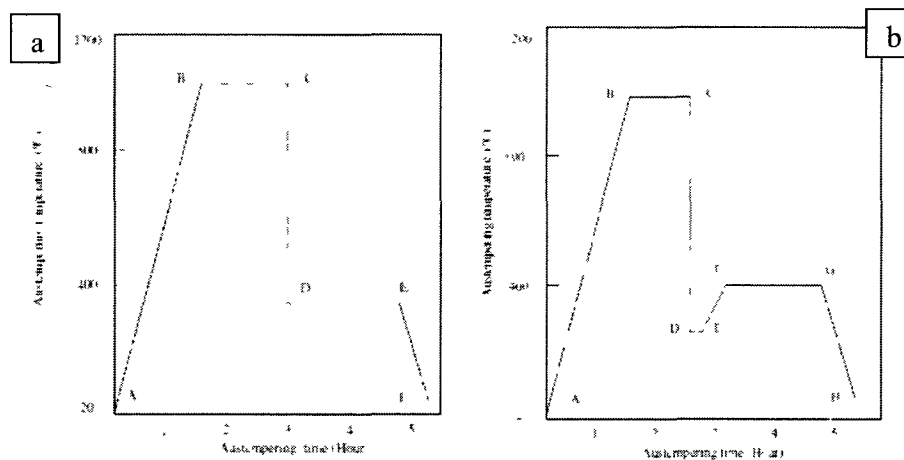


Figure 2.19: ADI heat treatment, a) conventional austempering, b) 2 step austempering [17]

Yang and Putatunda [17] investigated a novel two step austempering process (Figure 2.19) to compare with the conventionally austempered ADI with a 1.5Si-0.4Mn-0.30 Mo composition. While austenitizing was done at 927°C for 2h, the austempering was done over a wide range of temperatures between 260°C and 400°C for conventional austempering. For stepped austempering, the samples were quenched to 260°C for 5 min to serve as the step 1 austempering, and then they were austempered to same temperature and time as the conventional batch. The stepped austempering batch of ADI samples were found to have higher yield strength, tensile strength and fracture toughness compared to the conventionally austempered batch of samples. The stepped process also resulted in a

finer ferrite and austenite as well as higher austenitic carbon, which is crucial to maintain the stability of the retained austenite. But tensile toughness was found lower for two-step samples, which could be attributed to the reduction in the ductility as a result of two-step process.

Ravishanker et al [36] had similar findings regarding stepped austempering 1.5Ni-0.5Cu-0.3Mo ADI. Tensile and yield strengths increased with the two-step process while the ductility and tensile toughness decreased. Fracture toughness was also found to be increased with the 2-step process. This was attributed to a finer ferrite microstructure and increased carbon content in the retained austenite. Two-step austempering resulted in a microstructure of upper and lower bainite. But, the proportion of upper and lower bainite was dependent of the duration of the first step of austempering. The retained austenite content decreased with increasing carbon content in the retained austenite increasing.

Although austempering temperature and duration plays a pivotal role in tailoring the ADI microstructure and mechanical properties, the austenitizing parameters also have a noticeable effect on the microstructure and mechanical properties of ADI. A number of researchers have shown a strong influence on the ADI properties varying over the change of the austenitizing parameters. Bosnjak and Radulovic [37] examined a Ni-Mo alloyed ADI for varying austenitizing temperatures. Three austenitizing temperatures were selected (850, 900 and 930°C) and the austenitizing duration for each was 120 min. It was found that with lower austenitizing temperature, the austenite carbon content and austemperability are diminished while the propensity to the formation proeutectoid ferrite and pearlite is increased. Austemperability is the maximum section size of ductile iron that can be austempered without formation of pearlite during the austempering process. A more uniform microstructure was obtained by a lower austenitizing temperature. The

ausferrite transformation rate was found to be faster and the stage I austempering driving force was higher, with little or no effect on the stage II austempering for the low austenitizing temperature. Also, the process window was shifted to earlier austempering times, which would be beneficial from a cost point of view.

For a Ni-Cu-Mo alloyed ADI, the optimum austenitizing temperature was found to be 900°C. It was found by Bosnjak et al [38], that although decreasing the austenitizing temperature would increase the carbon content of the retained austenite, and improve on the toughness properties, the overall % retained austenite was reduced. The carbon solubility was lower than required at 850°C, which resulted in proeutectoid ferrite and pearlite in the microstructures. An higher austenitizing temperature such as 930°C, led to a significant reduction in mechanical properties as the higher temperature produced embrittling carbide precipitation.

Austenitizing below a critical austenitizing temperature results in partial austenitizing. By partial austenitizing, the ferrite-pearlite phase forms by commencing the austempering process from the ($\alpha+\gamma$) phase. Kicili and Erdogan [30] took this partial austenitizing approach in their ADI research. Partial austenitizing was done between 795 and 815°C and also conventional full austenitizing was done at 900°C for comparison. Partial austenitizing produced a microstructure with proeutectoid ferrite and ausferrite. Also, new ferrite of an epitaxial ferrite phase was found to be developed with a coarse austenite dispersion after austenitizing from the in the ($\alpha+\gamma$) phase. The series of ADI samples partially austenitized from the ($\alpha+\gamma$) field, the tensile strength increased and ductility decreased with increasing ausferrite volume fraction and decreasing proeutectoid ferrite volume. The best combination of ductility and strength was found with

60-65% ausferrite volume fraction compared to pearlitic ductile iron grades. But the ductility was slightly lower than the ferritic grades.

The TRIP (Transformation Induced Plasticity) effect is also influenced by the austenitizing parameters. The TRIP effect refers to the transformation of metastable austenite into martensite upon mechanical deformation. The TRIP effect is often considered to be negative, mainly because it results in premature wear. TRIP might also have some positive impact such as raising the fatigue resistance to a level comparable to carburized steel. But it must be emphasized that the TRIP effect is related to the austenite present within the volume of ausferrite. Although it might improve the surface wear properties, the toughness and tensile property would be reduced [3]. The TRIP effect and its relationship to the austenitizing parameters was studied by Daber et al [39]. In their work, a 1.5Ni-0.3Mo-0.5Cu composition ADI was subjected to austenitization at 850, 900 and 950°C for 2 hours. Tensile tests were carried out to observe the TRIP effect due to the tensile fracture. It was found that increasing austenitizing temperature increased the tendency for the formation of strain induced martensite, regardless of the austempering process. Also, a high austenitizing temperature coupled with a high austempering temperature was found to form unstable retained austenite which increased the tendency to form martensite upon mechanical deformation.

In a similar study by Daber and Rao [40], the TRIP effect due to conventional and two step austempering was investigated. The ADI composition was the same Ni-Cu-Mo ADI as in reference [39]. A conventional set of samples were austenitized for 30 min at 950°C and austempered for 2 hours at 300, 350 and 400°C. While the two step set of samples were first austempered at 300°C for 10, 20, 30, 45 or 60 min and then transferred

to furnace at 400°C for 2 hour austempering. Microstructural studies revealed that increased strain hardening was associated with the formation of strain-induced martensite. Samples with blocky austenite had the higher propensity to form more TRIP martensite. As found in [39], samples with higher temperature austempering had greater tendency to form TRIP martensite. The stepped samples, which were subjected to a short first step had large amount of upper ausferrite, which resulted greater strain hardening ability. This higher strain hardening ability of ADI was due to strain induced transformation of retained austenite, or in other words, TRIP martensite.

When doing research on ADI, it is very important to understand the microstructure descriptions of ADI. In the literature review, it was found that the main microstructure of ADI is being named differently. The term ‘ausferrite’ was most often used in the published research work. As discussed earlier, ausferrite is a unique microstructural arrangement of ferrite and austenite. Zimba et al [28], Trudel et al [41], Rundman et al [19], Thomson [42] and Kim et al [34] used the term ausferrite in their published works. Dai et al [43], Taran et al [44], and Sahin et al [26] preferred the term bainitic ferrite for the ferrite laths. The feathery laths of the ADI are often the shape of upper bainite ferrite laths. Upper and lower bainite terminology was used by Bhadeshia[45] and Rao et al [36, 39, 40, 46]. Yang and Putatunda [17] just defined the “special” ferrite as ferrite. A detailed explanation of the ADI microstructure can be found in the research publications of Kiliçli [30], Rundman [6] and Achary [18].

CHAPTER III

EXPERIMENTAL DETAILS

To understand and evaluate the ADI microstructure kinetics and properties, a series of ADI samples were created and then tested. The samples were created from a wide range of heat treatment schedules. They were tested and analyzed for three aspects: *mechanical*, *tribological* and *microstructural* properties. Mechanical properties included surface hardness, microstructural phase hardness (microhardness), tensile property, and toughness analysis. Tribological properties included scuffing and surface deformation analysis. Metallographic analysis was performed on all the samples using a variety of instruments and methods.

3.1 Overview of the Experimental Procedures and Measurements:

The experimental procedures can be divided into 5 main areas, namely:

1. Heat treatment design
2. Sample production
3. Mechanical property testing
 - a. Macrohardness
 - b. Micro hardness
 - c. Charpy impact test
 - d. Tensile testing
4. Tribology testing:
 - a. Scuffing performance
 - b. Surface deformation observation
5. Microstructural analysis

- a. Optical metallography
- b. SEM (Scanning Electron Microscopy) metallography
- c. Image analysis
- d. X-ray diffraction (XRD)

The XRD analysis was performed at Chrysler LLC Technology Center, MI. The scuffing testing was performed at the University of Oakland, MI. The tensile testing was performed jointly at Chrysler LLC Technology Center (CTC) and University of Windsor.

3.2 Material and Casting:

The ADI was a special chemistry ADI that was provided to us by our research partner, Chrysler LLC Technology Center (CTC). The chemical composition, which shows that it is predominantly a Ni-Cu-Mo alloyed ADI, is given on Table 3.1.

Table 3.1 Alloy composition of ADI

Element %wt	1	2	3
C	3.77	3.76	3.75
Mn	0.24	0.24	0.24
P	0.027	0.028	0.028
S	0.004	0.006	0.005
Si	2.45	2.60	2.50
Cr	0.03	0.03	0.03
Ni	1.62	1.59	1.62
Mo	0.11	0.11	0.11
Cu	0.77	0.81	0.77
Al	0.025	0.006	0.019
V	0.009	0.009	0.010
Cb	0.001	0.001	0.001
Ti	0.005	0.004	0.006
Co	0.023	0.024	0.023
Sn	0.002	0.001	0.002
B	0.0003	ND	0.0015
Mg	0.056	0.051	0.064
W	0.012	0.010	0.011

**1, 2, 3 indicate positions in the cast ingot.*

3.2.2 Casting Details:

- Wood patterns were created by the Chrysler Wood Shop.
- Cope & drag molds were produced with no-bake PepSet sand.
- Iron was melted in Ajax 500# coreless induction furnace at 1510°C.
- Melt charge consisted of pig iron, steel, ferrosilicon, copper, nickel.
- Iron was treated with 5% MgFeSi alloy with cover steel.
- Iron was inoculated with 75% foundry grade FeSi during transfer to pouring ladle.
- Iron was poured in molds at 1426°C.
- Molds were allowed to cool to room temperature before shakeout.
- Castings were cut from the gating with a band saw.
- Casts were shot blasted for surface finishing.

3.2.3 As cast samples:

Optical metallography of the as-cast ADI (without any heat treatment) (Figure 3.1) showed it to be predominantly pearlitic (85%) ductile iron with ferrite and nodular graphite. The bright ferrite regions surrounding the dark graphite nodules are often termed as “Cow’s Eye” or “Bull’s Eye”.

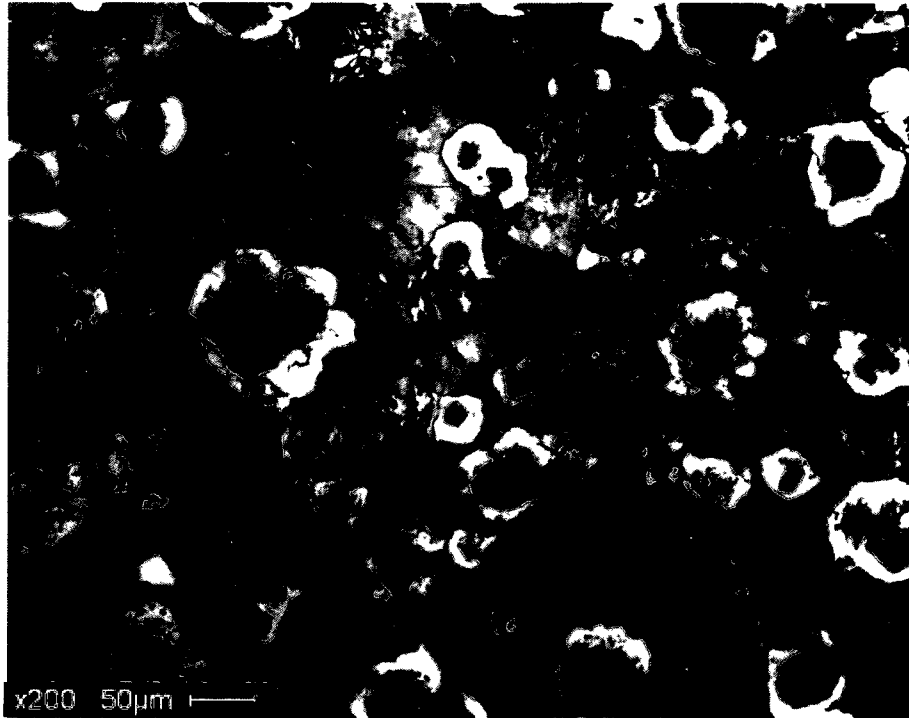


Figure 3.1: Optical micrograph of as-cast sample.

3.3 Heat Treatment Design:

3.3.1 Austenitizing temperature experiment:

A series of as-cast samples were austenitized for 15 minutes to observe the microstructural changes. The samples were then oil quenched to room temperature without any austempering. This experiment was conducted to observe the pearlite and ferrite transformations in the sample to determine an appropriate austenitizing temperature; see Table 3.2. Figure 3.2 (a-d) shows four optical micrographs illustrating the austenitizing time/temperature effects. From Figures 3.2(a) and (b), it can be seen that the ferrite-pearlite microstructure still remains at 700 & 740°C. At 740°C, the pearlite lamellas are segmented and shortened. At 820°C and 900°C, (Figures 3.2 (c) and (d)) it can be seen that the ferrite halos round the graphite nodules have been completely removed and the matrix microstructure is bainitic. A bainitic microstructure is only

possible through austenite decomposition, which indicates that at 820-900°C, our samples were fully austenitized. After careful metallographic observation of all samples, an austenitizing temperature of 890°C for 20 minutes was selected for the subsequent tests.

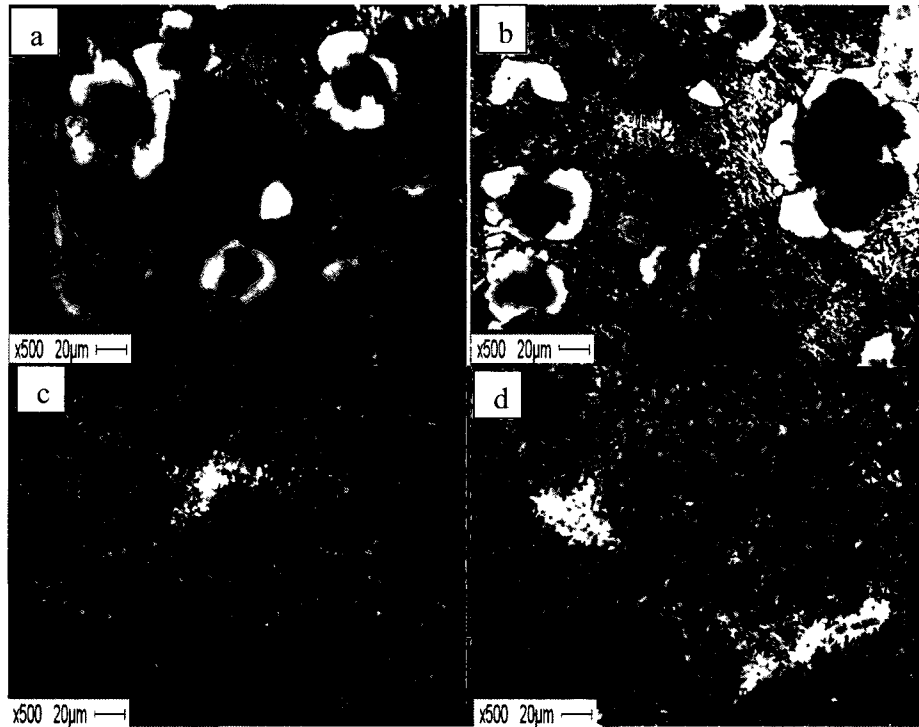


Figure 3.2 Microstructure comparison of austenitized samples: a)700C, b)740C, c)820C d)900C

Table 3.2: Austenitizing process of initial test samples.

Sample no	Heating Temperature (°C)	Hold Time (Mins)	Quenching Method
Sample 1	As Cast	-	-
Sample 2	700	15	Oil Quench
Sample 3	740	15	Oil Quench
Sample 4	780	15	Oil Quench
Sample 5	820	15	Oil Quench
Sample 6	840	15	Oil Quench
Sample 7	880	15	Oil Quench
Sample 8	900	15	Oil Quench
Sample 9	920	15	Oil Quench
Sample 10	940	30	Oil Quench
Sample 11	960	30	Oil Quench

3.3.2 Austenitizing and austempering schedules:

Heat treatment schedules with a fixed austenitizing time/temperature but a range of austempering times/temperatures were chosen on the basis of the published literature and industrial experience. This variation in austempering time and temperature is expected to provide a spectrum of mechanical/tribological performance. Figure 3.3 illustrates the heat-treatment schedules chosen.

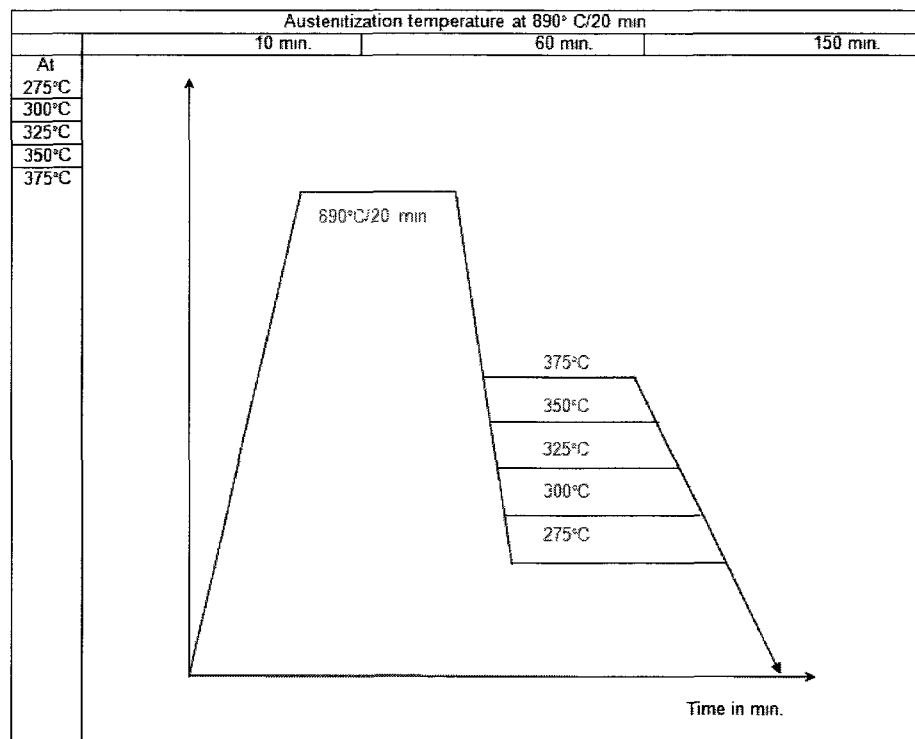


Figure 3.3: Heat Treatment Schedules

The austenitization was set at 890°C for 20 minutes. Austempering on the other hand was conducted at 15 different time-temperature combinations. The temperatures ranged from 275-375°C and the austempering times ranged from 10 to 150 minutes.

3.4 Charpy Impact Testing:

The Charpy tests were conducted at Chrysler LLC Technology Center (CTC) to ASTM E23 specifications [47]. The specimens were V notched with the dimensions of 55mmX10mmX10mm; see Figure 3.4. The impact velocity used was 17.21 ft/s. Three samples were tested for each heat treatment condition. Figure 3.5 shows a broken (after testing) Charpy sample.

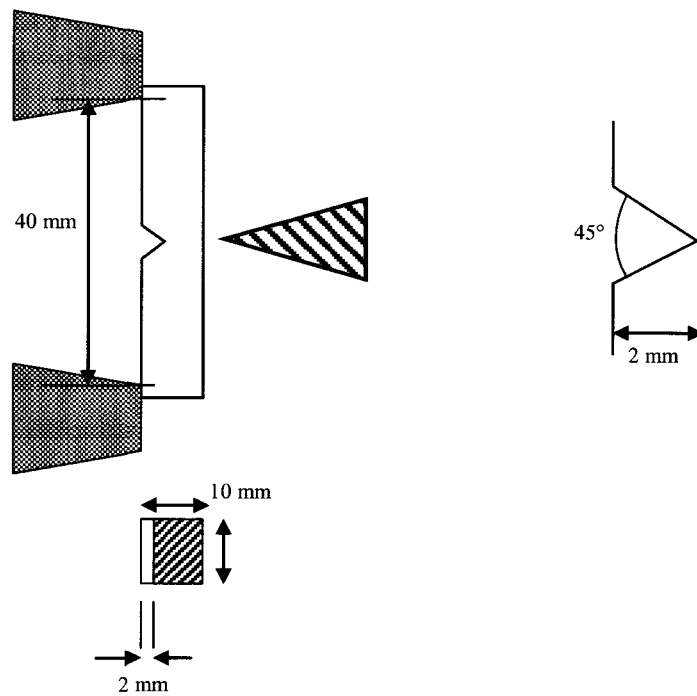


Figure 3.4 ASTM E23 Charpy test diagram

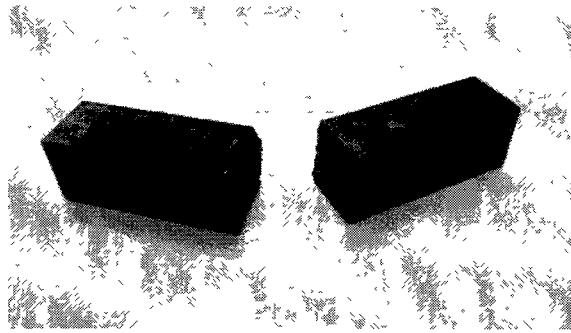


Figure 3.5 Charpy sample after testing.

3.5 Hardness Tests:

Both surface hardness (macrohardness) and microhardness measurements were made.

3.5.1 Surface Hardness:

For surface hardness (macrohardness), the Rockwell hardness test with a Rockwell C scale (150 kg load: Brale indenter) was used (Figure 3.6). Broken Charpy samples were used to conduct the hardness test. The surfaces of the samples were cleaned with a rubbing cloth and checked for any surface impurities. Only clean and smooth areas without any deformation or cracks were selected for the hardness testing. Five indentions were done on each sample, and the average hardness result calculated.

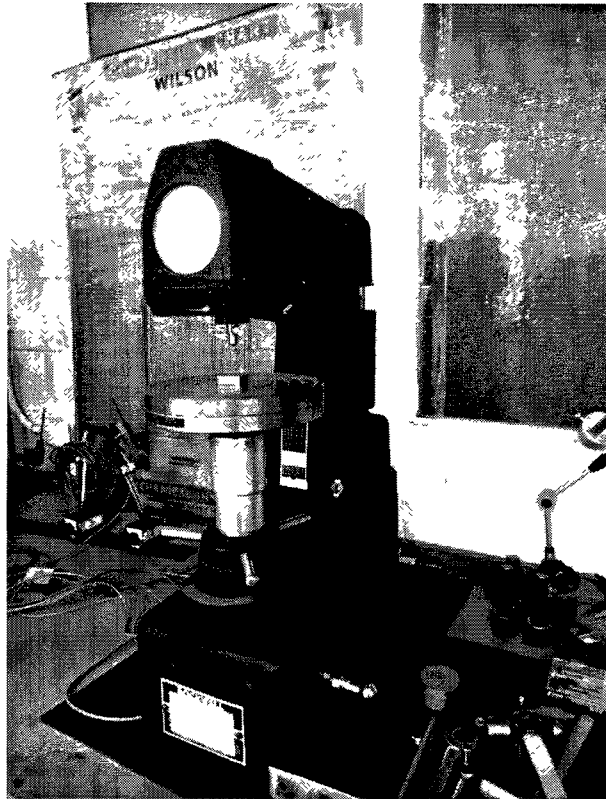


Figure 3.6 Rockwell hardness testing machine.

3.5.2 Microhardness:

Microhardness tests were also conducted on all of the samples. The microhardness testing machine was equipped with an optical microscope with up to 100X magnification. This allowed us to measure the hardness of the specific phases, which were clearly observable on the optical metallographs. The hardness of all the separate phases (pearlite, ferrite, retained austenite, ausferrite, and martensite) was measured with a Knoop (200-400g load, indenter and 15 sec indentation time) hardness method. A total of five indentations were conducted on each phase area and the average hardness value calculated. The samples used for the microhardness testing were the same as for SEM and Optical metallography.

3.6 Tensile Testing:

Tensile testing was performed according to ASTM standard E8-04 [48]. The tests were conducted at both the Chrysler LLC Technology Center (CTC) and the University of Windsor. Figure 3.7 shows the dimensions of the ASTM E8-04 tensile bars. Two specimens were tested for each austempering time/temperature combination.

The testing system is shown in Figure 3.8a. The elongation was measured by an extensometer which was attached in the center area of the tensile bars (Figure 3.8b). The gage length was 1 inch. Figure 3.8c shows a broken tensile bar after the test. The initial tensile bar grips had serrated edges. The wedged mechanical grips on the tensile testing machines were slipping under high tensile loads, rendering the elongation results invalid. The grip area was too short for the steel wedges. The grip area was then threaded to give better gripping and less slip. Initially the tensile tests were performed on an Instron™ tensile testing machine, but the maximum load capacity of the machine was unable to fracture the ADI samples. Subsequent samples were tested on a Tinius-Olsen™ tensile testing machine with a higher load capacity.

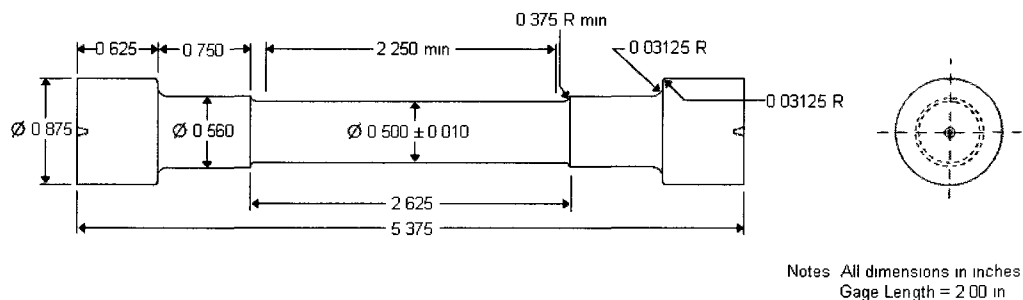


Figure 3.7 : ASTM E8-04 Specification for tensile test specimens [48]

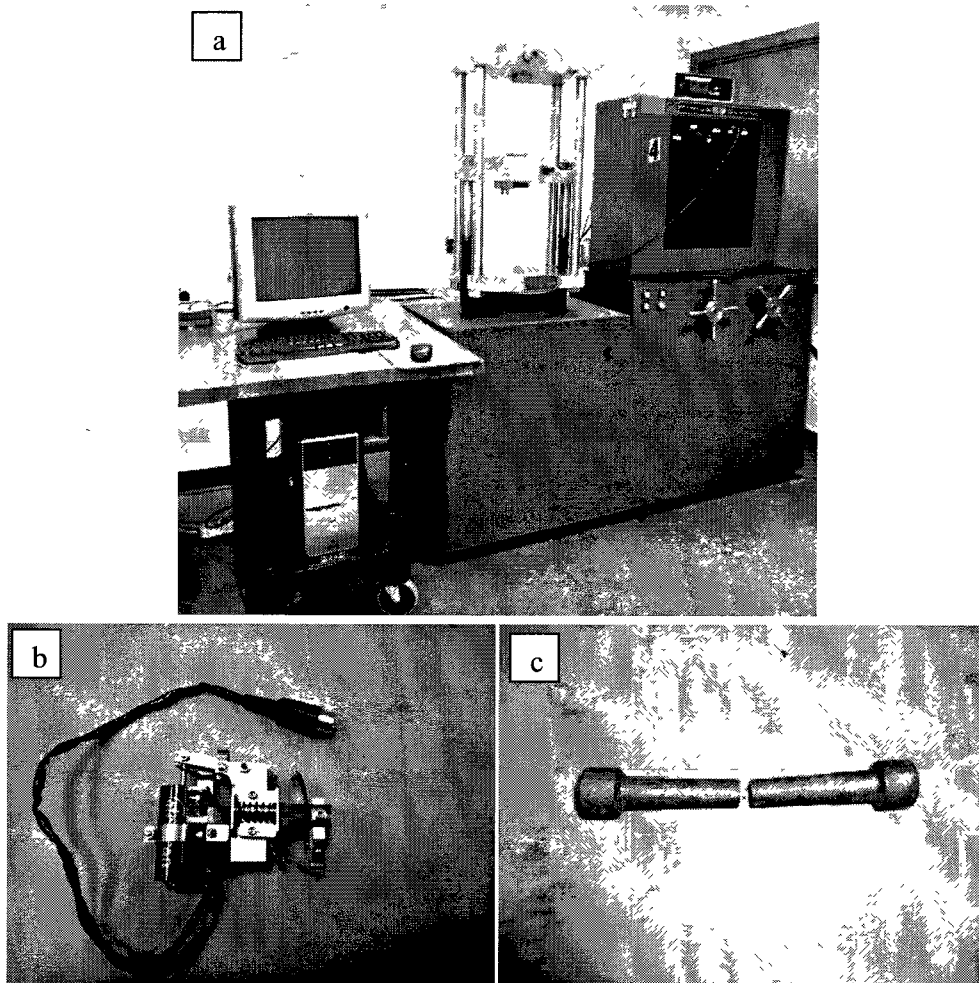


Figure 3.8 : Tensile testing equipment a) Tinius-Olsen testing system, b) extensometer, c) broken sample after testing.

3.7 Surface Profilometry:

The Charpy fracture surfaces were observed using both metallography to determine the general fracture characteristics and by stylus profilometry (Figure 3.9). To increase the stylus accuracy, it was sharpened after purchase. Stylus profilometry gave results with $1\mu\text{m}$ accuracy. The measuring equipment was Mitutoyo-Type IDC-112MEB, capable of measuring to $.001\text{mm}$. A 1mm fine point stylus was used to mount on the measuring device after further sharpening the tip to near 0.1mm .

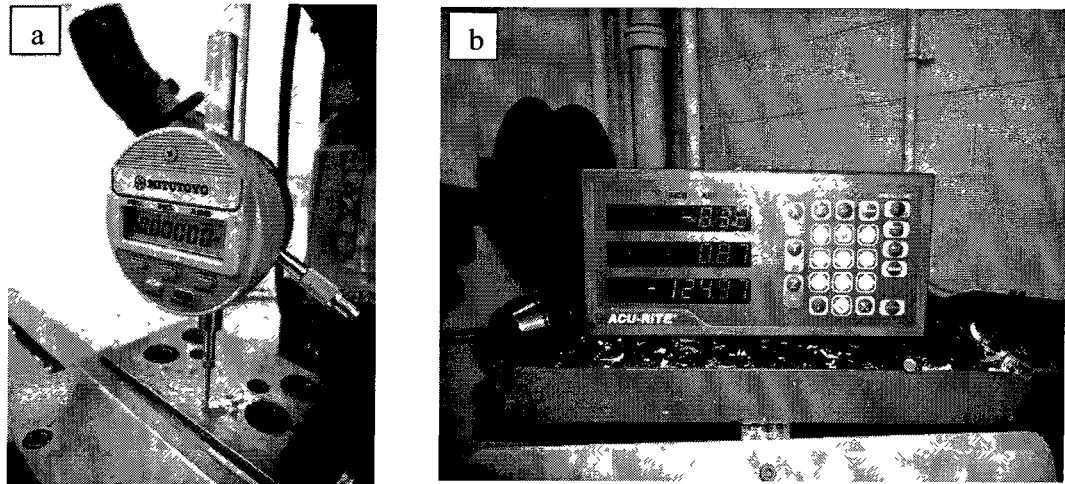


Figure 3.9 : Stylus surface profilometry a) Measuring unit, b) Digital tray control

The surface profile was measured both along (X axis) and across (Y axis) the Charpy impact motion. The profile was recorded at 1 mm intervals in both X and Y directions for all the fractured samples. This profilometry could provide valuable information on the surface roughness, ductility of the material and also help us better understand the SEM images [49].

The surface roughness was measured with roughness average R_a . Roughness average R_a is the arithmetic average of the absolute values of the roughness profile ordinates. Equation 3.1 shows the mathematical equation of measuring the surface roughness R_a .

$$R_a = \frac{1}{l} \int_0^l Z(x)/dx \quad \text{Equation 3.1}$$

Where l is the total measured length, and z is the height of the surface peaks [50].

3.8 Metallography:

For optical metallography, each sample was hot mounted using a Buehler Mineral Filled Phthalate powder. Samples were then ground and polished to a mirror surface. The

polishing was done in steps with a Buehler Handimet II Roll Grinder, starting with a rough, abrasive polish to a very fine smooth polishing. The first steps were done using SiC papers from 100 grit to 600 grit. Final polishing was done with a Buehler Metaserv Grind-Polisher and Buehler Micropolish II Deagglomerated Alpha Alumina oxide powder (Al_2O_3) suspended in water. Samples were polished using $1.0\ \mu\text{m}$ oxide powder applied to a Buehler Billiard Cloth, and $0.05\ \mu\text{m}$ oxide powder applied to a Buehler Microcloth. After polishing, the samples were etched with nital. For optical microscopy, they were etched with 2% nital for about 5 seconds. For SEM metallography, the samples were etched with 1% nital for a approximately two seconds. Optical micrographs were taken on each sample at 50, 100, 200, 500 and 1000 times magnification levels. Figure 3.10 shows the SEM equipment used for the ADI metallography.

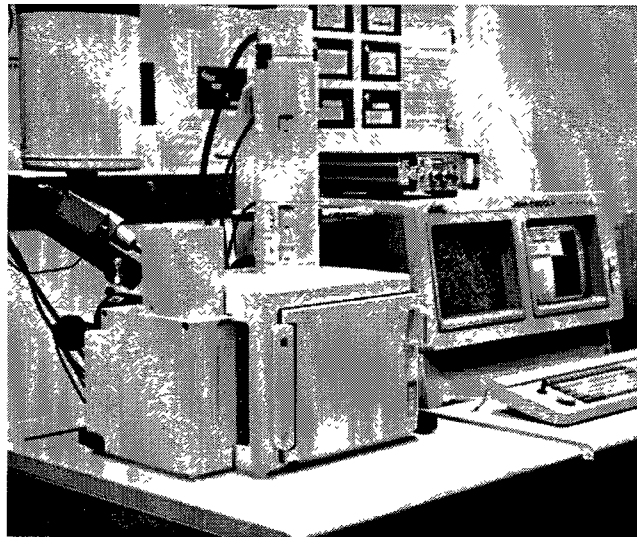


Figure 3.10: SEM equipment

3.9 X-Ray Diffraction:

To determine the volume fraction of retained austenite for each heat treatment process, X-ray diffraction (XRD) was done by using monochromatic Cr-K α radiation (wavelength $\lambda=2.29 \text{ \AA}$) at 20 kV and 20 mA, and an X-ray diffraction intensity strip chart recording. The recorded profiles were analyzed to obtain the precise diffraction peak positions and integrated intensities. The volume fraction of retained austenite was determined by the direct comparison method using integrated intensities of the (200) α and (211) α peaks of ferrite, and the (200) γ and (220) γ peaks of austenite [51, 52].

3.10 Scuffing Test:

A ball-on-disc tribometer, Figure 3.11, was used to carry out the tests. The linear sliding speed was either 1.649m/s or 1.356m/s. The applied normal load was increased 22N every 120 seconds and the test was terminated when a sudden increase of the coefficient of friction, large noise and severe vibration occurred. The load at this moment was defined as the scuffing load. The friction force was measured with a strain gauge mounted on the sample holder. The disc specimen was lubricated by white mineral oil with a viscosity of 33.5cSt at 40°C. All tests were repeated 4 times and the average coefficient of friction (COF) and scuffing load were recorded. Typically the coefficient of friction was approximately 0.1 before scuffing and increased rapidly to approximately 0.25 when scuffing occurred.

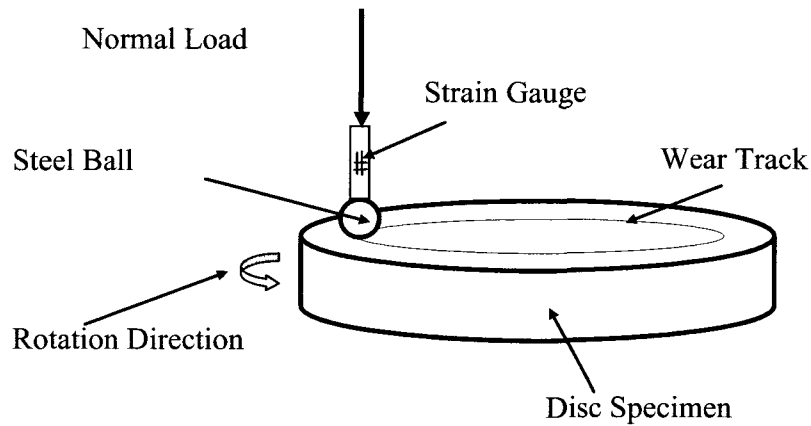


Figure 3.11: Ball on disc scuffing test equipment

3.11 Image Analysis:

The microstructure images obtained by the optical microscopy were analyzed using ImageJ [53] and Photoshop software. The software analysis provided a very good understanding on the overall quantitative assessment of the microstructures present in the optical micrograph.

The image analysis was performed to isolate and measure the area percentage of three different phases in the microstructure: The dark nodular graphite, Grey/semi dark acicular phase, which is ausferrite or martensite depending on the sample, and the light coloured retained austenite. They were separated using the color and geometric features. For example, graphite was separable due to its very dark appearance and the nodular shape. ImageJ provided tools to separate using the color saturation and the nodularity factor. Then they were further filtered using Photoshop to exclude any of the inconsistencies which were not graphite. Finally the images were exported back to the ImageJ to calculate the area percentage of the graphite nodules.

The optical images selected for this analysis were at the 50X and 100X magnification levels, which are the two lowest magnification levels. This was done due to the fact that 50x images had an overview of all the possible phases present in the system. Higher magnification would provide the software a better chance to recognize the geometric features, but the overall image might not represent a true picture of the actual phase distributions.

Figures 3.12 (a-b), shows a image analysis photo comparison. Figure 3.12(a) is the original optical micrograph of our sample ADI. Figure 3.12(b) is the isolation of the graphite nodules only from the original image, which was done using the ImageJ saturation system and nodularity tool. Further enhancement was manually done using Adobe PhotoShop.

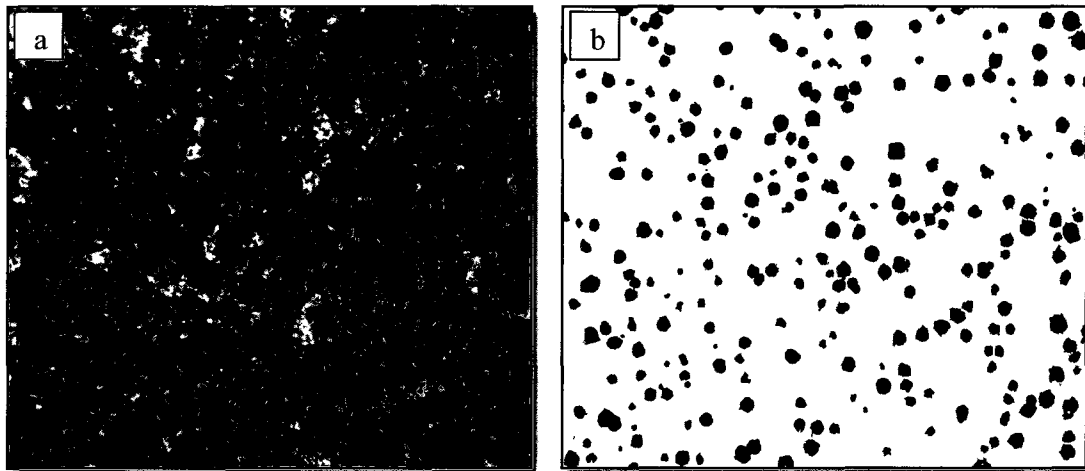


Figure 3.12: Optical image analysis for graphite nodule percentage. a) original micrograph, b) graphite nodules separated after ImageJ and Photoshop filtering.

CHAPTER IV

MICROSTRUCTURE CHARACTERIZATION

This chapter discusses the microstructural observation and characterization of all ADI samples. Both qualitative and quantitative analysis was performed on the data gathered from optical micrographs, SEM images, XRD results for retained austenite and software image analysis.

4.1 Austempering Temperature and Time Effect:

Optical micrographs of the as cast and all the heat treated samples are shown in a series of images shown in Figures 4.1 to 4.6. For each sample, two images at high (1000x) and low (200x) magnifications are presented. The lower magnification image is useful in understanding the overall phase and graphite nodule distribution. The higher magnification image is required to understand the detailed microstructures.

From Figures 4.1 (a-b) it can be seen that the as cast microstructure does not contain any acicular bainitic ferrite or martensite. The as-cast microstructure is predominantly pearlitic (85%). The graphite is mainly nodular in shape, and almost every graphite nodule is surrounded by a bright halo of ferrite. This formation of bright ferrite surrounding the dark graphite nodule is often termed as 'Bull's Eye' [54]. There is some ferrite present which is divorced from the graphite nodules. Some ferrite is also present in the pearlite grain boundary regions.

The heat-treated samples can be segmented into 3 groups based on their microstructural characteristics: martensitic, mixed martensite-ausferrite, and ausferritic (Bainitic ferrite). The lower austempering temperature samples (275 and 300C) produced a microstructure which is predominantly martensite. From Figures 4.2-4.3, we can see in

the high magnification images very sharp and long dagger-shaped martensitic laths. Although at times, it was difficult to differentiate between bainite and martensite laths, the bainite laths would be thicker and plate shaped. There is a noticeable effect of the austempering time. The 10 min austempered samples at both temperatures (275 and 300°C) had the sharpest and coarsest needles: see Figures 4.2 (a-b) and 4.3 (a-b). The 60 min austempering samples had the finest needles: see Figures 4.2 (c-d) and 4.3 (c-d).

The medium austempering temperature (325°C) samples created a unique mixed ADI microstructure, which are shown on Figure 4.4. From the high magnification microstructures (Figure 4.4- b, d and f), it can be seen that the microstructures consists of both a martensite microstructure with dark sheaves of ausferrite (bainitic ferrite) needles. The 10 minute sample (Figure 4.4 a-b) microstructure has less bainitic ferrite sheaves. The 60 minute sample (Figure 4.4 c-d) has more balanced martensite-ausferrite microstructure. The 150 minute sample (Figure 4.4 e-f) is mostly ausferrite.

Higher austempering temperatures (350 and 375°C) however create a microstructure which is predominantly ausferrite, as shown in Figures 4.5 and 4.6. The bainitic ferrite laths are very thick and feathery for the longer austempering times. This is because as the austempering temperature increases, the sheaves of bainite become thicker and the subunits are easier to resolve [14]. When comparing the laths/sheaves of the ausferrite samples with the martensite samples (Figure 4.6d and Figure 4.2b), the difference between the martensite and ausferrite microstructure is very evident. Ausferrite or bainitic ferrite laths are thicker, shorter, segmented and the edges have a feathery or saw-type profile. On the other hand, the martensite needles are much longer, narrower

and have a smooth profile edge. For both 350 and 375°C, it can be seen that the 10 minute samples have the narrowest and least feathery ausferrite laths: see Figure 4.5b and 4.6b. SEM images at higher magnification of samples austempered for 60 or 150 mins at 350 and 375°C are shown on Figures 4.7 a-b. This image comparison gives us a clear idea on the feathery ausferrite profile. The highly feathery ausferrite laths (Figure 4.7b) are seen to be much more segmented, thicker and rough profiled compared to the lower feathery ausferrite (Figure 4.7a).

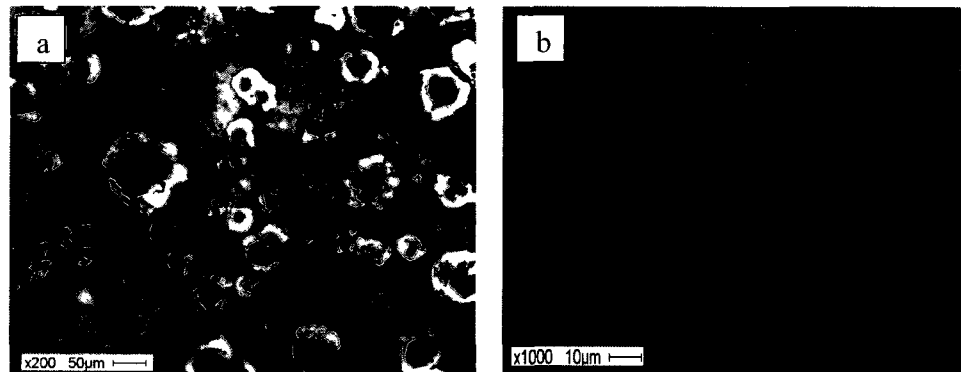


Figure 4.1 : Optical micrographs of As-cast samples.

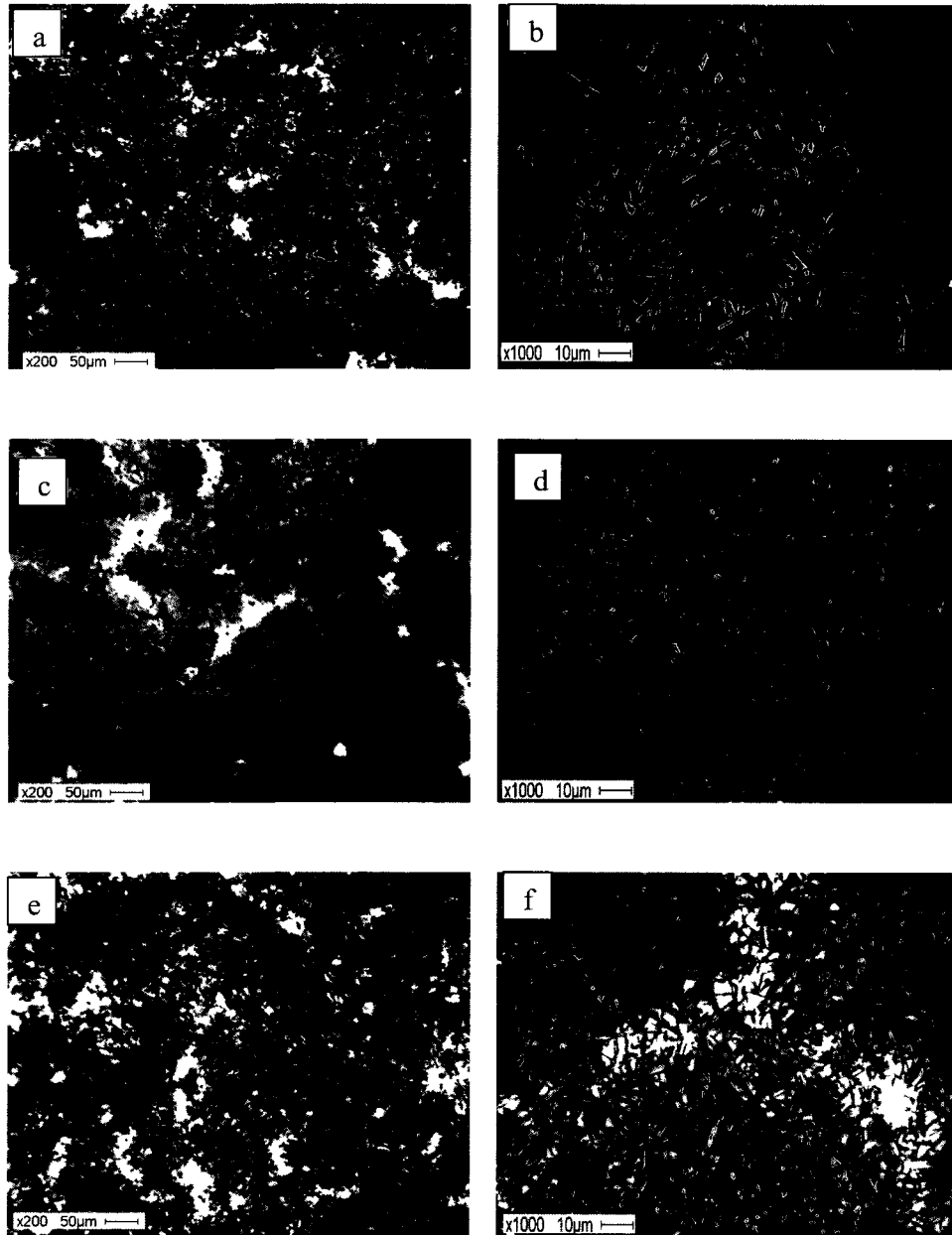


Figure 4.2 : Optical micrographs of samples austempered at 275°C, a-b) 10 min, c-d)60 min e-f)150 min.

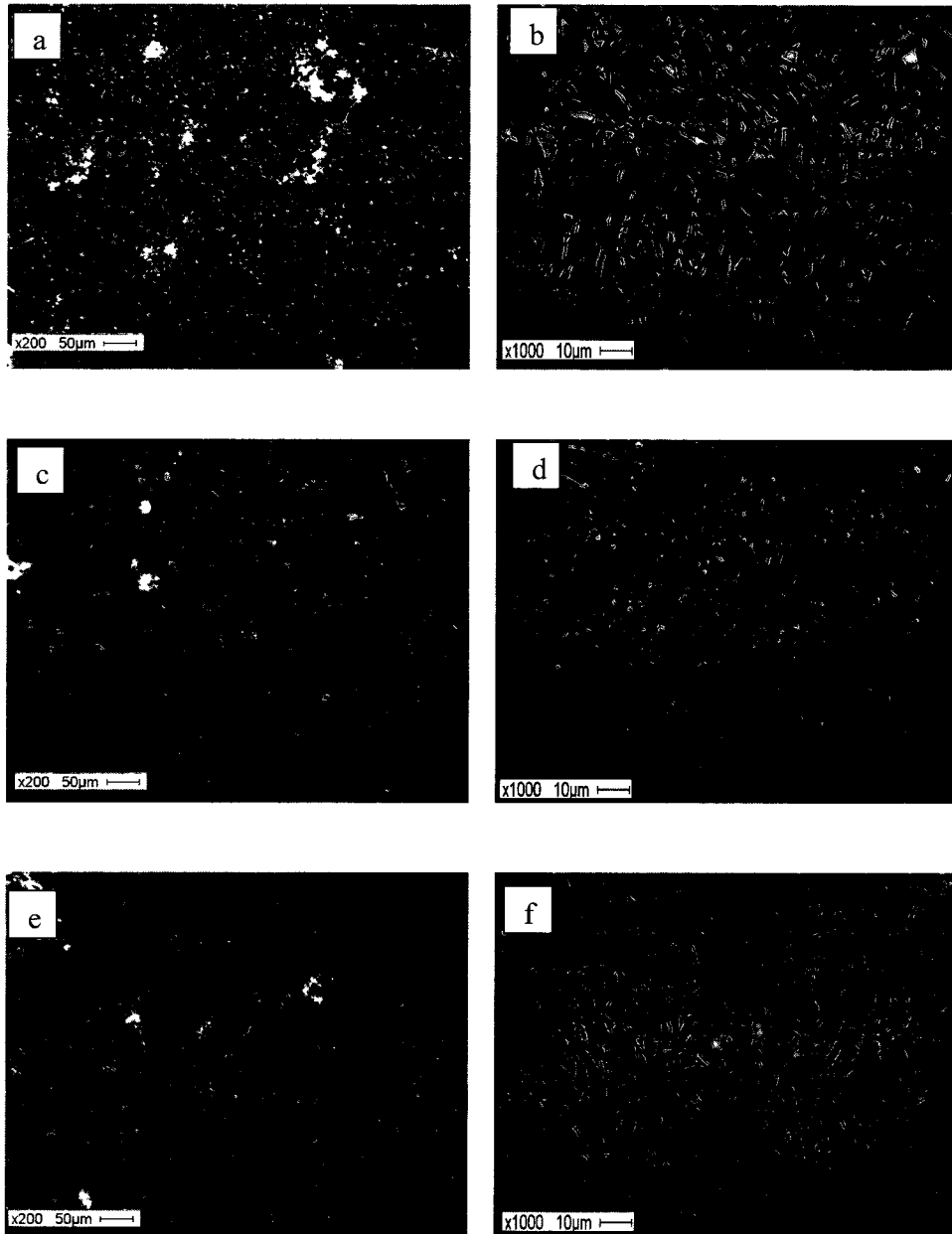


Figure 4.3 Optical micrographs of samples austempered at 300°C, a-b) 10 min, c-d)60 min e-f)150 min

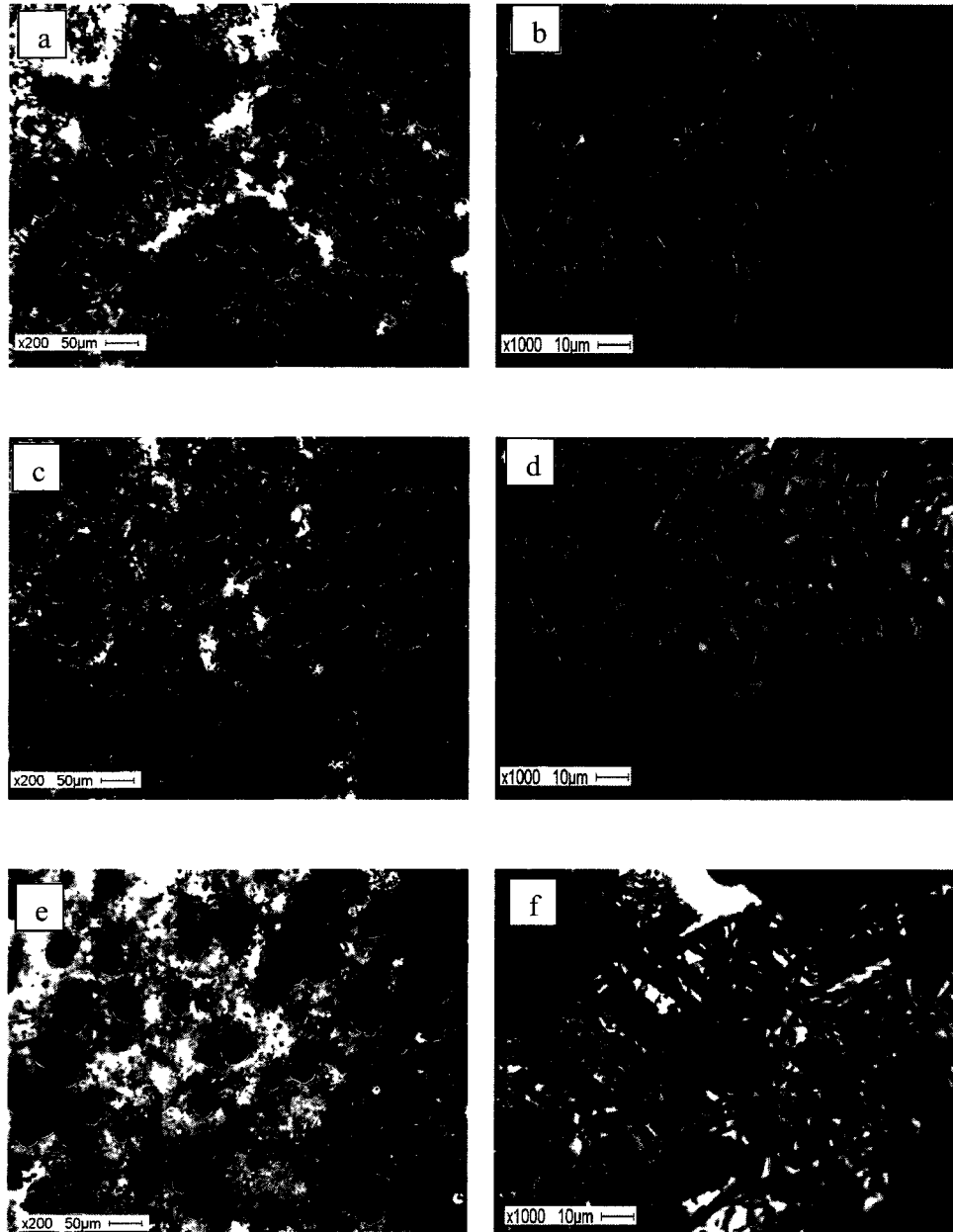


Figure 4.4 :Optical micrographs of samples austempered at 325°C, a-b) 10 min, c-d)60 min e-f)150 min

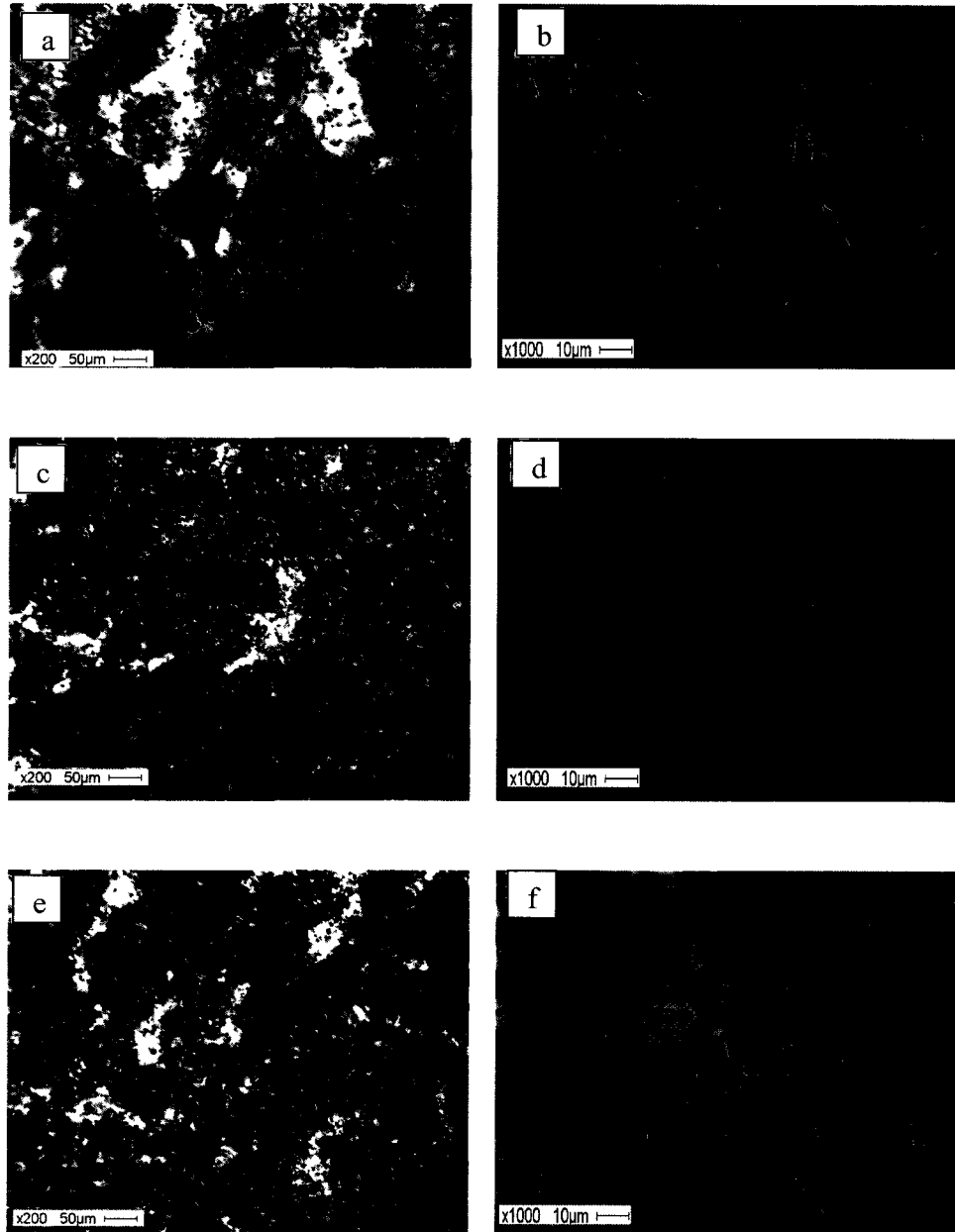


Figure 4.5:Optical micrographs of samples austempered at 350°C, a-b) 10 min, c-d)60 min e-f)150 min

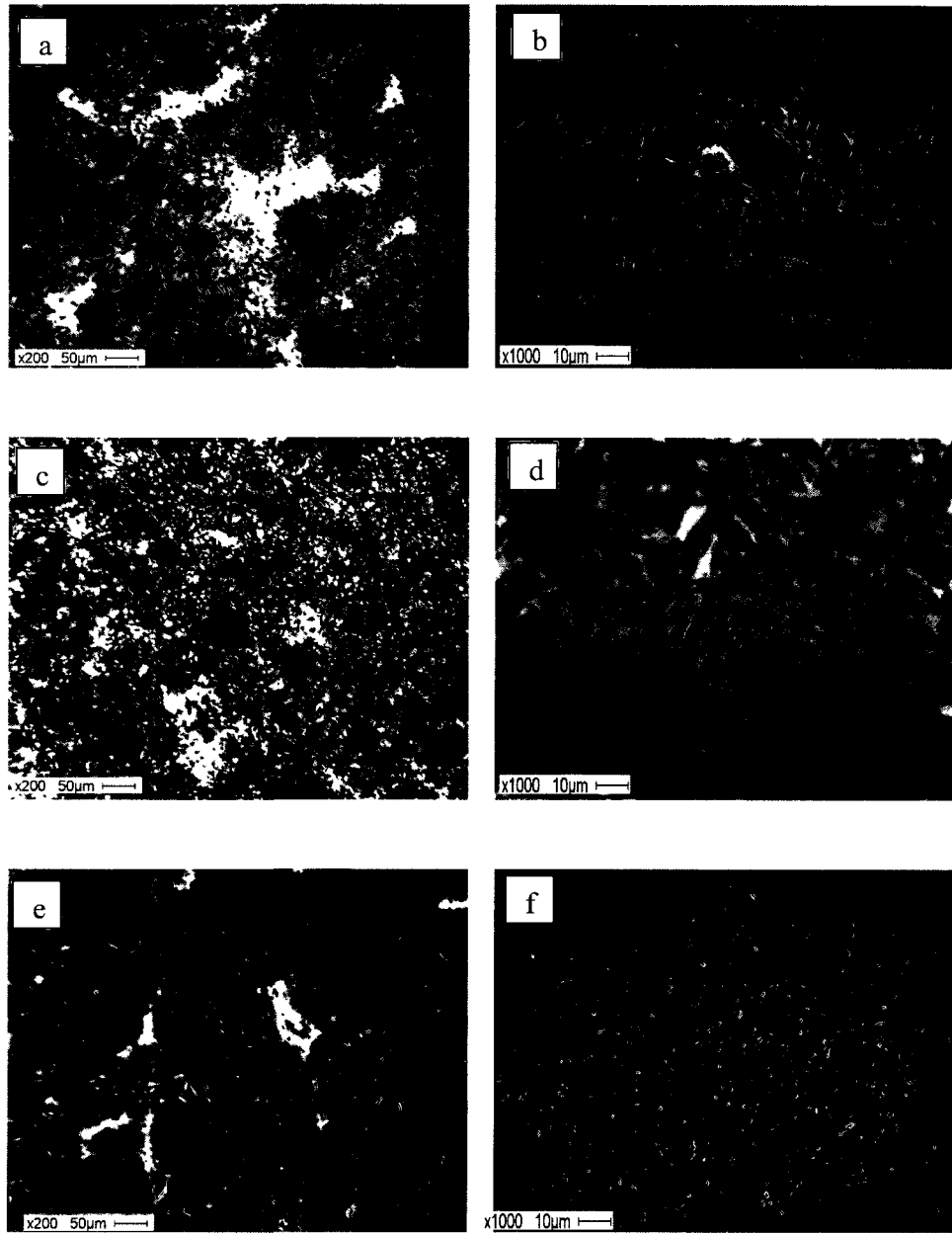


Figure 4.6: Optical micrographs of samples austempered at 375°C, a-b) 10 min, c-d)60 min e-f)150 min

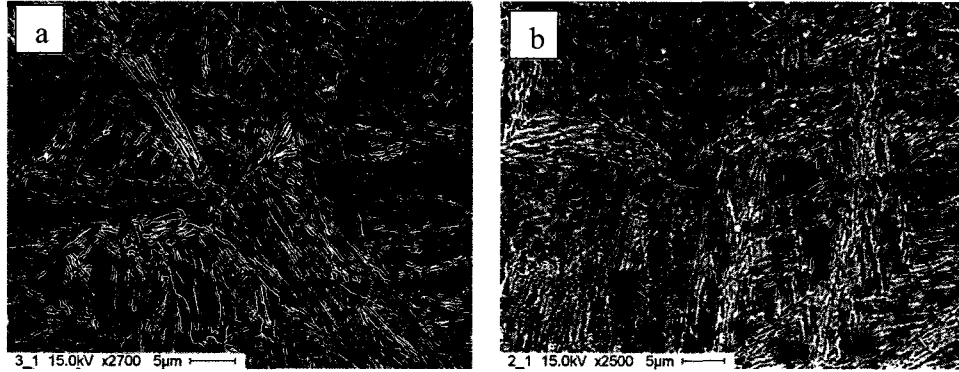


Figure 4.7: SEM micrographs of: (a) Medium feathery ausferrite, (b): Highly feathery ausferrite.

4.2 Retained Austenite:

XRD analysis showed that the % retained austenite was dependant on the austempering time and temperature: see Table 4.1. The table is color coded for high (dark gray), medium (light gray) and low (white)-retained austenite content. 35-33% is considered high, 25-29% as medium and 12-24% is categorized as low.

Table 4.1: Volume % retained austenite for ADI samples.

Temp\Time	10min	60min	150min
275°C	12	15	14
300°C	18	28	27
325°C	23	33	33
350°C	27	35	34
375°C	29	36	35

The % retained austenite versus austempering temperature for 10, 60 and 150 minutes austempering time is plotted in Figure 4.8. The % retained austenite increases with increasing austempering temperature regardless of the austempering time. The 10 minute samples have the lowest % retained austenite, compared to 60 and 150 minute samples. The % retained austenite is a indicator of the ausferrite, or bainitic ferrite, content on the microstructure. Samples with martensitic microstructure contain the least

% retained austenite, while samples with coarse feathery bainitic ferrite contain the highest % retained austenite.

These results can be explained by the stage 1, stage 2 process and the process window for the austempering process. It could be assumed that the austempering process ends before completion of stage 1, generating only a small amount of ausferrite and converting the remaining matrix into martensite when specimens are quenched after only 10 minutes. 60 minutes could be assumed to be within the process window, thus producing the highest amount of ausferrite, and thus retained austenite. 150 minutes however could be assumed to be entering the stage 2 of the austempering, which will begin to reduce the ausferrite content by developing carbides. It can be seen by a slight drop in the austenite content from 60 to 150 minutes on **Table 4.1**.

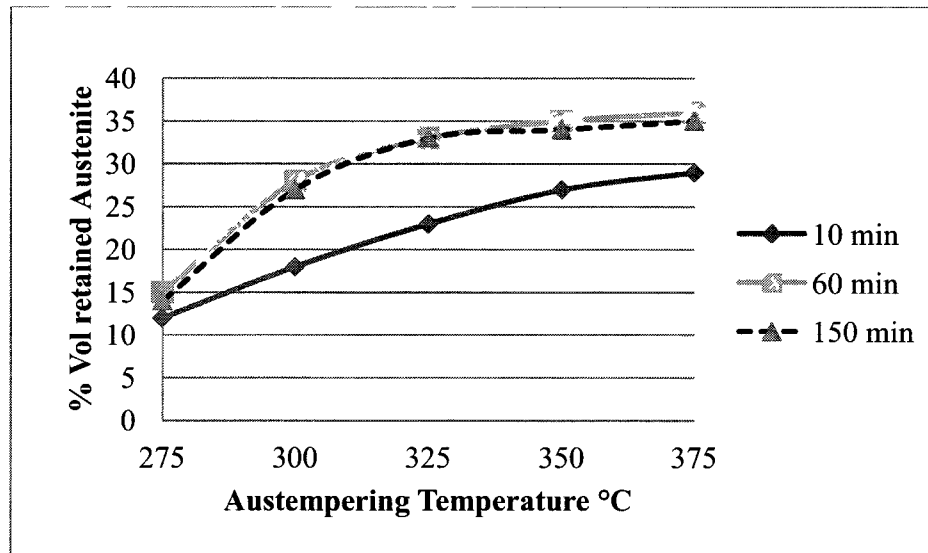


Figure 4.8: Relation between austempering temperature and % vol retained austenite for 3 different time durations.

Relationship between the austempering time/temperature and the % retained austenite is best illustrated in a 3D plot shown in Figure 4.9. The bright yellow/orange zone represents the highest % of retained austenite and dark blue represents the lowest. It

can be seen that the bright yellow and orange region is located at the 60 min high temperature zone. Although 150 minute zone represents high % retained austenite, the diagram shows it is slightly less than the 60 minute zone.

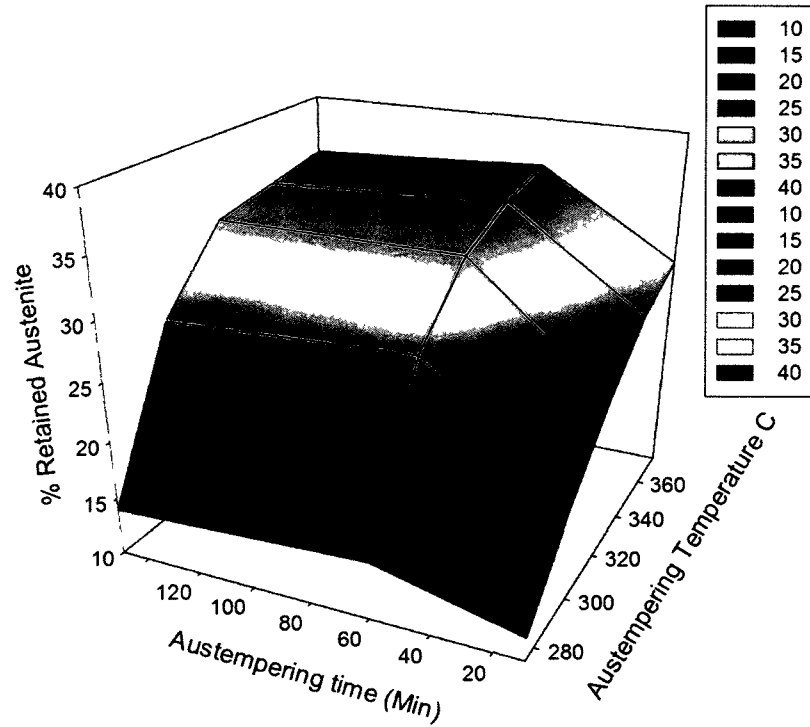


Figure 4.9: 3D plot relationship between % retained austenite and austempering time/temperature.

4.3 Qualitative Microstructure Image Analysis:

Image analysis with the help of ImageJ, Adobe Photoshop and the XRD results of the retained austenite allowed us to develop an approximate qualitative breakdown on the percentage of microstructural phases in the ADI samples. Table 4.2 shows the results of the qualitative microstructure characterization of the ADI samples. The boxes with N/P indicates that the phase was assumed to be absent from the microstructure characteristic observation.

Table.4.1: Microstructure area % of the ADI samples

Austempering Temp (C)	Time (Min)	graphite	Retained Austenite	Ausferrite	Martensite
275	10	13.6	12	N/P	74.4
	60	17.2	15	N/P	67.8
	150	13.2	14	N/P	72.8
300	10	14.4	18	N/P	67.6
	60	10.8	28	N/P	61.2
	150	12.1	27	N/P	60.9
325	10	15.4	23	29.9	31.7
	60	13.4	33	53.6	N/P
	150	15.7	33	51.3	N/P
350	10	13.9	27	38.6	18.5
	60	13.2	35	51.8	N/P
	150	12.4	34	53.6	N/P
375	10	13.9	29	26.8	30.3
	60	15.8	36	48.2.1	N/P
	150	16.9	35	48.1	N/P

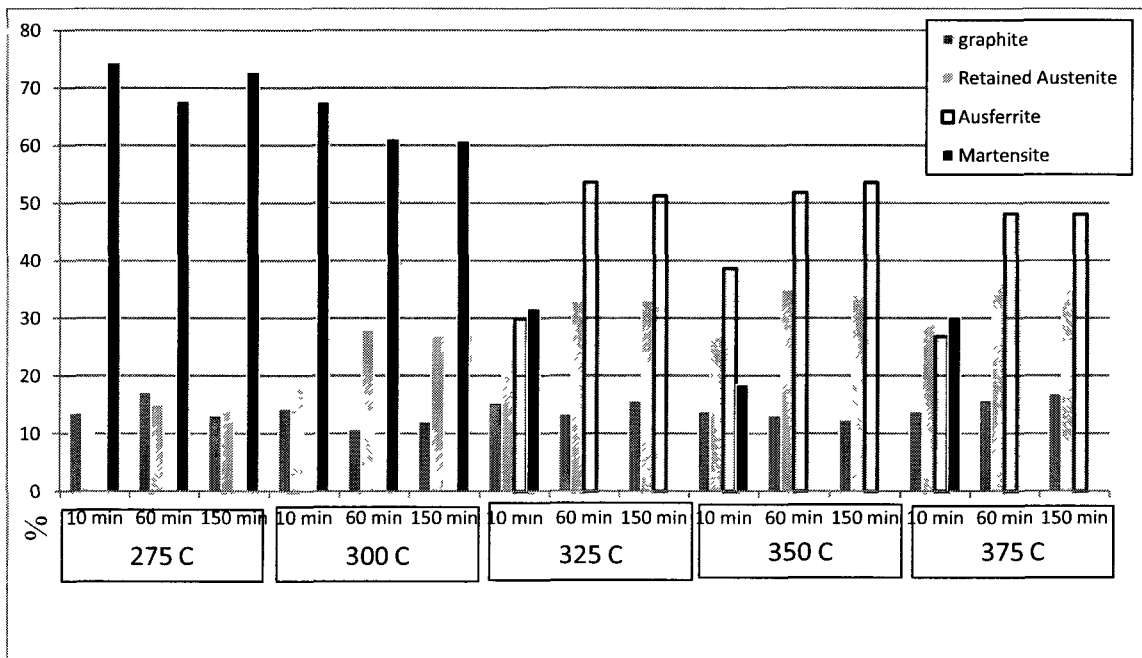


Figure 4.10 : Microstructure balance comparison of all the ADI samples.

Figure 4.10 shows a schematic representation of the different phases that are present in the various austempered samples. An important factor worth noticing here is the martensite-ausferrite-retained austenite balance in the samples. Samples with less than 25% retained austenite have a high level of martensite and no ausferrite. Higher levels of retained austenite are usually paired with ausferrite. From the literature review in chapter 2.12, a combination of ausferrite and retained austenite gives the best mechanical performance for ADI.

4.4 Summary

Following conclusions are drawn from the microstructural analysis:

1. Austempering temperature and duration heavily influences the microstructure of ADI.
2. Three groups of microstructures are developed from varied austempering time (10-150min) and temperature (275-375°C): martensitic, mixed martensite-ausferrite, ausferritic microstructure.
3. Lower austempering time and temperature gives a martensitic microstructure, higher austempering time and temperature gives an ausferritic microstructure.
4. Some of the ADI samples with medium austempering temperature (300-325°C) and short to medium time (10-60 min) produce a mixed martensite-ausferrite microstructure.

CHAPTER V

MECHANICAL PROPERTY ANALYSIS

This chapter focuses on the analysis of the data obtained from the mechanical testing, including tensile testing, Charpy testing and hardness testing.

5.1 Hardness:

Table 5.1 summarises the macrohardness data obtained from the Rockwell hardness tests. From Table 5.1 it can be seen that the hardness of the as-cast sample is the lowest with 23 HRC, presumably due to the pearlite-ferrite microstructure which was discussed previously in Chapter 4.1. The 10 minute samples all had a very high hardness level. This is due to the presence of martensite in the microstructure as discussed in Chapter 4.1. The hardness level decreased with increasing austempering time and temperature. Figure 5.1 illustrates the relationship between hardness and austempering conditions.

The samples having the highest hardness levels are 275C-10 and 60 minutes and 300C-10min, and the lowest hardness levels were found in samples 375C-60 and 150 min, and 350C-60 and 150 minute. From the microstructure of these samples, we can conclude that the presence of martensite gives the highest hardness, while the feathery bainitic ferrite or ausferrite microstructure produces the lowest hardness.

It is noticeable from Figure 5.1 and Table 5.1 that every heat treated sample had a significant jump on the hardness level compared to the as cast sample. All grades (I to V) were achieved by the austempering of our specified chemistry ADI. The numbers in the parentheses () in Table 5.1 represent the ASTM hardness grade for ADI. The dark gray, gray and white color coding indicates high, medium and low hardness levels.

Table 5.1: Hardness (HRC) of the as cast and heat treated samples.

Temp/Time	10min	60min	150min
As Cast	23		
275C	55.8 ±1(V)	46.0±0.5(IV)	45.1±0.5(III)
300C	51.0±1(V)	42.1±4(III)	42.4±0.1(III)
325C	45.7±0.3(III)	35.2±2(II)	36.7±1.2(III)
350C	45.4±1(III)	32.0±1.5(II)	32.0±1.25(II)
375C	45.2±3(III)	27.6±0.5(I)	27.6±1(I)

* Number in the brackets indicate ASTM hardness grade.

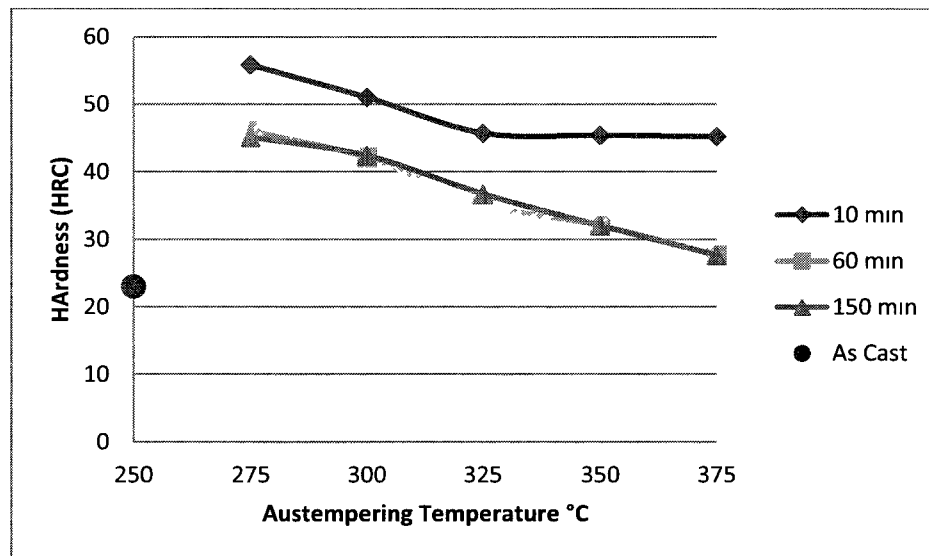


Figure 5.1: Relationship between hardness (HRC) and austempering temperature for 3 different time durations.

The hardness level can be related to the % retained austenite, since the presence of retained austenite determines the microstructure. Figure 5.2 shows a fairly linear, inverse relationship between the hardness level and the % retained austenite. Two separate relationships have been developed from the plotting. The hardness relationship of ADI samples with less than 30% retained austenite is expressed on Equation 5.1 and the solid

trend-line in Figure 5.2. Equation 5.2 and the dotted trend-line shows the relationship between retained austenite and hardness for ADI samples with higher than 30% retained austenite. From the coefficient of determination R^2 values, it can be said that the hardness decreases much faster for high (more than 30%) retained austenite ADI samples. In Figure 5.1, the hardness curve fitting has been segmented into two lines, below and above 30% retained austenite level. From the microstructure characterization, it was observed that ADI with greater than 30% retained austenite develops feathery ausferrite, which has significant influence on the mechanical properties. Also on Figure 5.1, it can be seen that the hardness level drops sharply once the retained austenite goes higher than 30%. Thus the plot was segmented to two parts. From Equation 5.1 and 5.2, it can be seen that the coefficient of determination is much higher for the ADI samples with higher than 30% retained austenite. This indicates that the hardness trend is more predictable with ausferrite microstructure. The points at the 10-15% austenite zone is very scattered. This is the low temperature, low time sample region. This inconsistencies of hardness has reduced the coefficient of determination for the low retained austenite samples. The combined result is also shown on Equation 5.3. A combined result shows R^2 value of 0.77, which is slightly lower than the high austenite hardness, but higher than the low austenite hardness.

$$H = -0.4375(RA) + 55.298 \quad (R^2 = 0.4665) \quad \text{Equation 5.1}$$

$$H = -2.8364(RA) + 129.23 \quad (R^2 = 0.8319) \quad \text{Equation 5.2}$$

$$H = -0.8889(RA) + 64.298 \quad (R^2 = 0.7687) \quad \text{Equation 5.3}$$

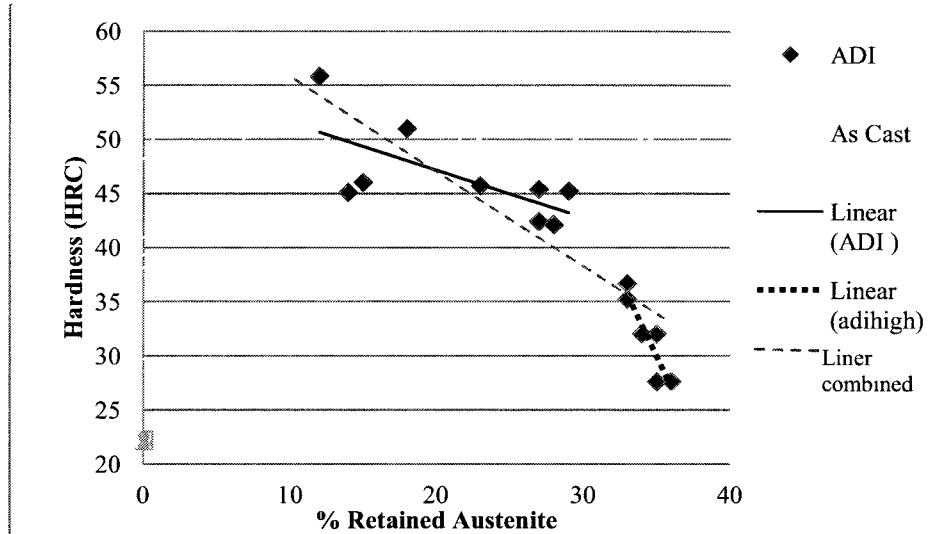


Figure 5.2: Relationship between hardness (HRC) and %vol retained austenite.

Figure 5.3 shows the relationship between hardness and the austempering time and temperature in a 3D plot. It can be seen that the high hardness values of yellow and orange color area falls in the low time and temperature zone of the 3D quadrant. It is noticeable from the figure that the low and high hardness falls in the extremes of the plot. Which indicates the hardness and softness is found at the lowest and highest temperatures. Also noticeable is the very wide range of hardness that was achieved from the heat treatment. The plot ranges approximately from 25-60 HRC. This is a wide spectrum of hardness level which can be useful over a very wide range of engineering applications.

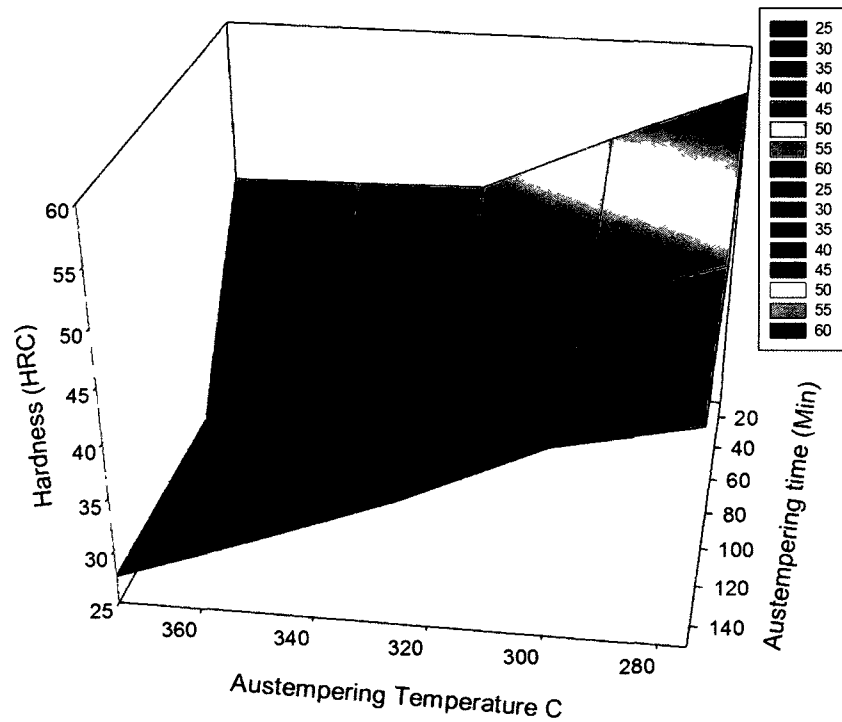


Figure 5.3: 3D plot relationship between hardness (HRC) austenite and austempering time/temperature.

5.1.1 Microhardness:

The microhardness data of the individual phase areas are shown in Vickers hardness in Table 5.2. It is difficult to see any particular trends apart from the highest value was recorded from the martensite and the lowest value was recorded from retained austenite. The range of hardness measured for each phase was quite large. This could be due to the fact that the targeted microhardness locations have different phases in the subsurface.

Table 5.2: Microhardness (HV) of different phases in ADI samples

Austempering Temperature (C)	Time (Min)	Martensite	Ausferrite	Retained Austenite
275	10	5941	N/P	5287
	60	4209	N/P	4052
	150	4740	N/P	3762
300	10	4376	N/P	N/P
	60	3708	N/P	3383
	150	3270	N/P	3059
325	10	N/P	4923	N/P
	60	N/P	4850	N/P
	150	N/P	3226	N/P
350	10	N/P	4157	4157
	60	N/P	3226	3226
	150	N/P	2939	2739
375	10	N/P	3226	N/P
	60	N/P	4923	N/P
	150	N/P	3941	N/P

5.2 Toughness:

The Charpy fracture toughness results are given in Table 5.3. It is worth mentioning here that the Charpy toughness specimens in our tests were notched specimens as detailed in Chapter 3. Notched samples provide a much lower level of toughness values compared to un-notched samples [41]. It should also be mentioned that the results for the 10 minute samples are not given in Table 5.3 since they showed high variability in test results.

From Table 5.3 and Figure 5.4, it can be seen that the Charpy toughness increases with increasing austempering temperature. Also the 150 minute samples exhibit a slightly higher toughness level compared to the 60 minute samples. The highest toughness levels were obtained from 350°C-150 min and 375°C-60 minute and 150 minute samples. These samples also contained the highest % retained austenite, i.e. ausferrite microstructure. The

samples with a thick and feathery ausferrite microstructure produced the highest toughness levels. Figures 5.5a and b demonstrate that the toughness is proportional to the % retained austenite, and inversely proportional to the hardness.

Table 5.3: Charpy impact toughness (J) for as cast and ADI samples.

Temp/Time	60min	150min
As-Cast	2.2	
275°C	4.11	4.36
300°C	5.13	5.46
325°C	5.96	6.28
350°C	5.98	6.71
375°C	6.45	9.20

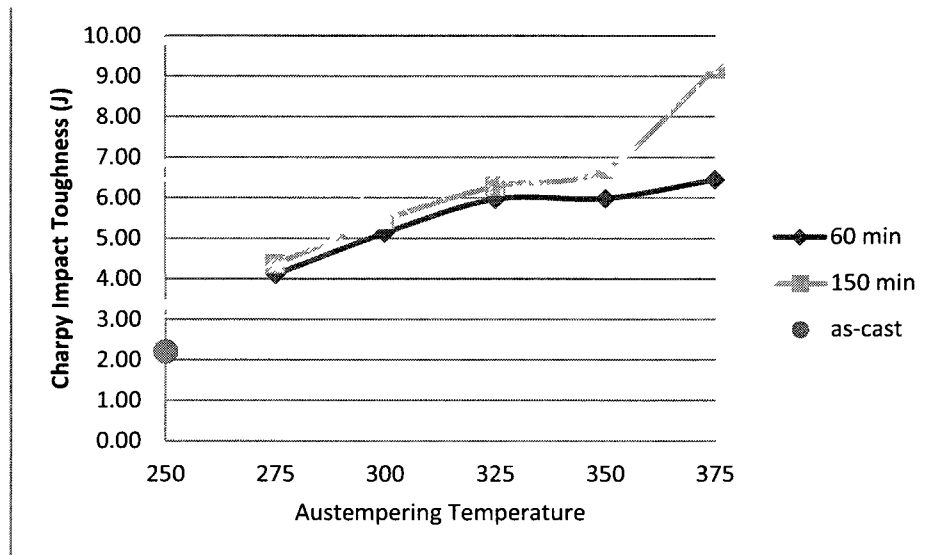


Figure 5.4 : Relationship between Charpy impact toughness (J) and austempering temperature for 2 different times.

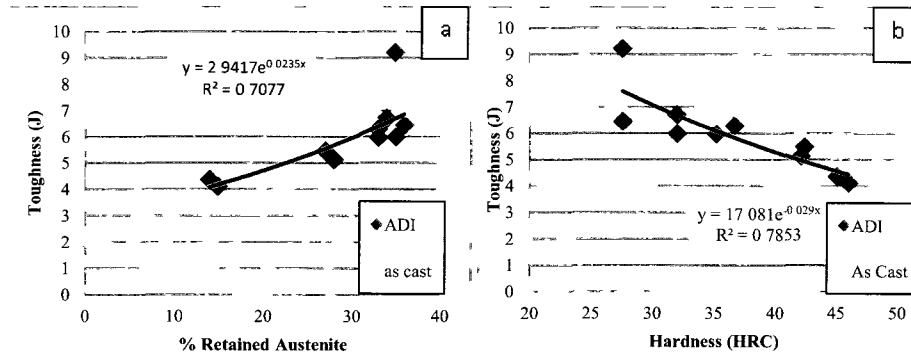


Figure 5.5: Relationship between toughness and (a) % retained austenite and (b) hardness.

SEM fractographs of all the Charpy samples at 500x magnification are illustrated on Figures 5.6 to 5.11. It can be seen that all the heat treated samples had a very rough fracture surface. This is sign of enhanced toughness. In contrast, the as-cast sample Figure 5.6, exhibited a relatively flat surface that is characteristic of brittle fracture, cleavage facets are noted. The heat-treated samples exhibit micro-cup and cone features. It is difficult to perform any quantitative analysis of the SEM fractographs. But qualitatively it can be stated a brittle material would have a smooth surface and a tough material would have a rougher fracture surface.

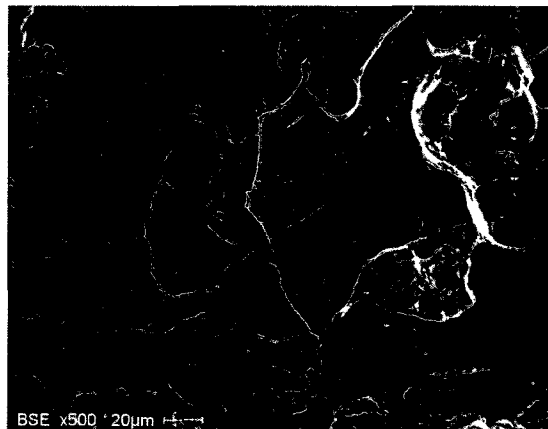


Figure 5.6: SEM fractographs of Charpy specimens of the as-cast sample.

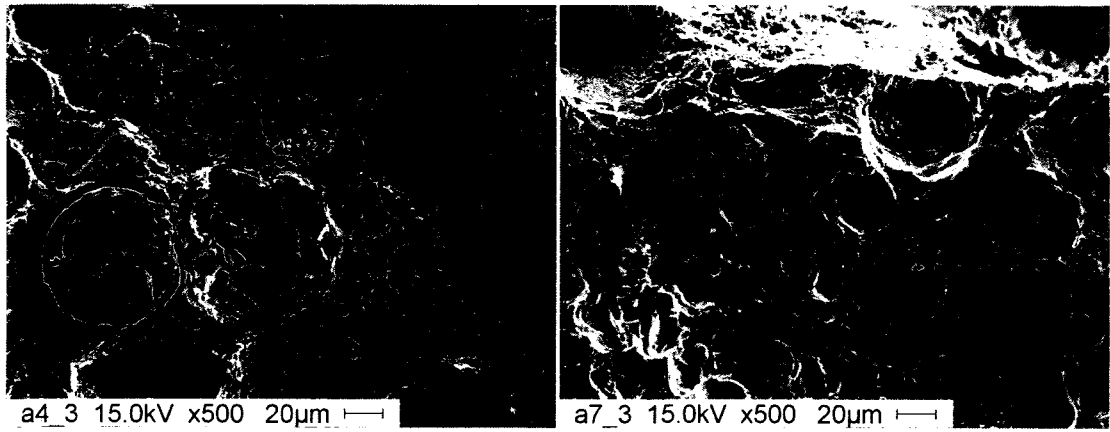


Figure 5.7: SEM fractographs of Charpy specimens austempered at 275 C, for a) 60 min, b)150 min

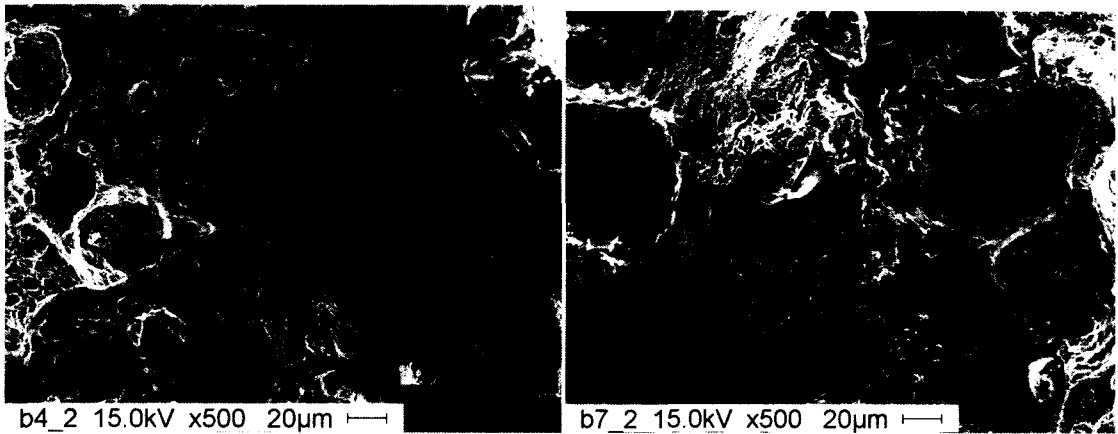


Figure 5.8: SEM fractographs of Charpy specimens austempered at 300 C, for a) 60 min, b)150 min

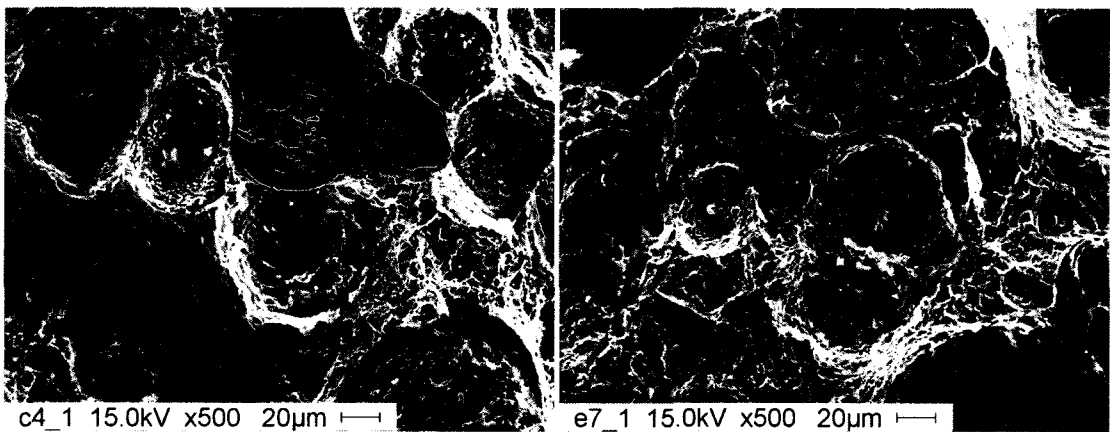


Figure 5.9: SEM fractographs of Charpy specimens austempered at 325 C, for a) 60 min, b)150 min

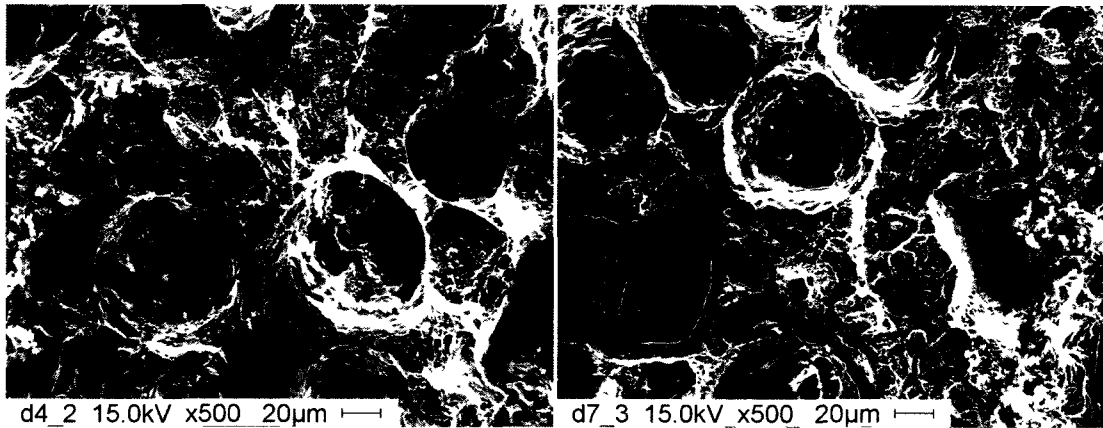


Figure 5.10: SEM fractographs of Charpy specimens austempered at 350 C, for a) 60 min, b)150 min

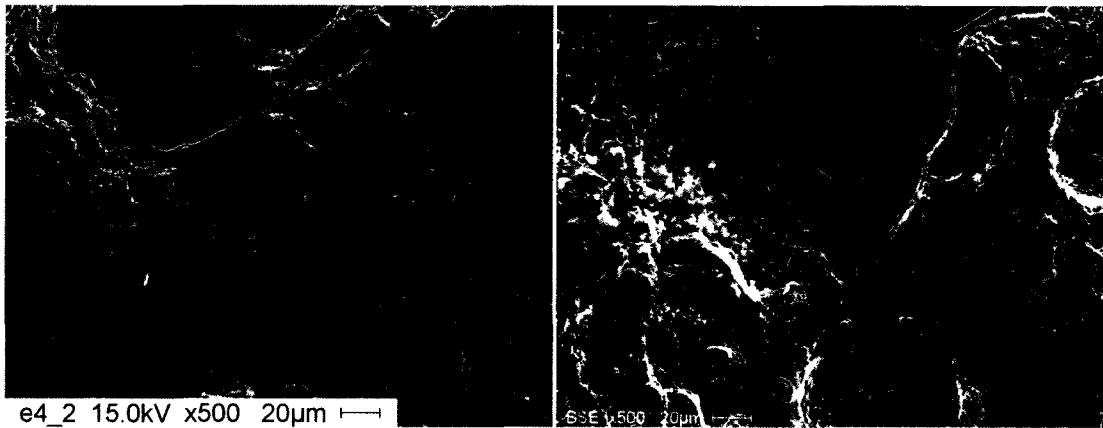


Figure 5.11: SEM fractographs of Charpy specimens austempered at 375 C, for a) 60 min, b)150 min

The average roughness (Ra) values as obtained by surface profilometry are given in Table 5.4 and compared in Figure 5.12. The austempering temperature has no obvious effect on Ra. However, a trend can be seen with austempering time. The 150 minute austempered samples had a rougher fracture surface compared to the 60 minute austempered samples for an identical temperature. In Table 5.4, gray color code is again used to indicate relatively higher Ra values. The higher Ra is evidence of higher ductility: more cup and cone and less cleavage fracture.

Table 5.4: Average roughness (R_a) of fractured ADI samples.

Austempering Temperatures (C)	Orientation	Roughness Average R_a (μm)	
		60 min	150 min
275	X	28.26	35.36
	Y	51.10	83.59
300	X	28.89	54.36
	Y	17.32	64.74
325	X	47.69	89.95
	Y	23.78	38.74
350	X	63.23	104.01
	Y	44.75	59.12
375	X	44.62	72.19
	Y	29.93	78.67
Average		37.96	68.07

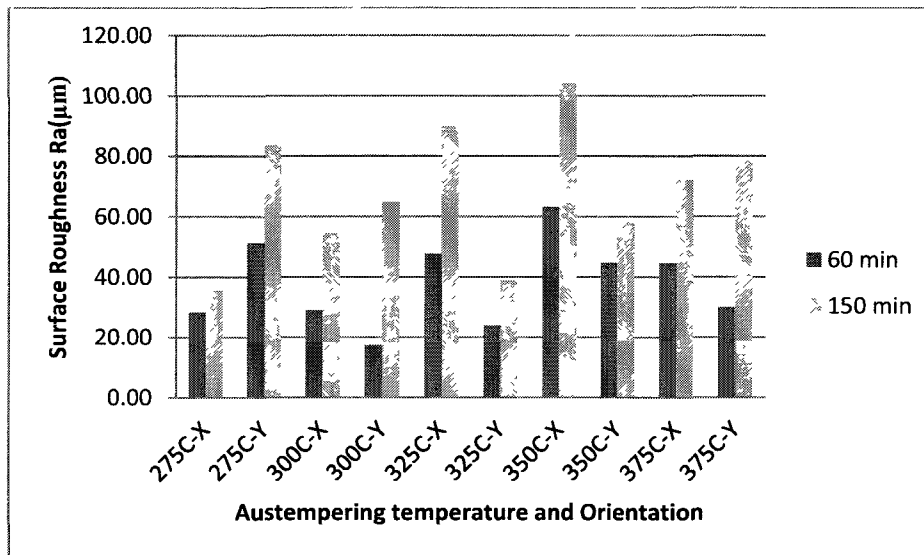


Figure 5.12: Charpy fracture surface roughness average (R_a) comparison between 60 min and 150 min austempered ADI.

5.3 Tensile Properties:

Tensile properties of the heat-treated samples are summarised in Table 5.5. A wide range of tensile properties were developed. The ultimate tensile strength varied over the range 900 to 1500Mpa, and the elongation ranged was from 1 to 7.8%. The gray color code in Table 5.5 indicates results from faulty samples which fractured outside the gage length and N/A indicates an experiment malfunction.

Table 5.5: Tensile properties of the as-cast and austempered samples

Heat Treatment		Sample	YS(MPa)	UTS (Mpa)	%El
As Cast		1	550.6	768.0	3.95
		2	546.5	737.6	4.25
275C	60min	1	1275.0	1275.0	1.0
		2	888.0	1373.5	2.25
	150min	1	1261.5	1459.6	1.57
		2	1256.0	1538.6	2.79
300C	60 min	1	965.5	1283.5	1.733
		2	1214.5	1320.0	1.47
	150 min	1	N/A	1309.0	N/A
		2	N/A	1408.0	N/A
325C	60 min	1	N/A	1236.5	N/A
		2	N/A	776.5	N/A
	150 min	1	1028.0	1247.5	3.23
		2	1003.0	1238.5	2.82
350C	60 min	1	726.0	988.5	3.4
		2	722.5	981.5	3.5
	150 min	1	771.0	976.5	4
		2	779.5	991.0	4
375C	60 min	1	647.5	942.5	6.1
		2	684.5	913.5	6.1
	150 min	1	656.0	924.5	7.8
		2	664.5	880.0	4.65

The UTS data are plotted in Figure 5.13. All the heat treated samples had significantly higher ultimate tensile strength (UTS) compared to the as-cast sample. The austempering temperature had a significant effect on the UTS, with UTS decreasing with

increasing austempering temperature. This is an agreement with the hardness data in Table 5.1. The percentage elongation showed an opposite trend to the UTS; see Figure 5.14. The 150 minute austempered samples had slightly higher elongations compared to the 60 minute samples. The relationship between percentage elongation and the UTS is illustrated on Figure 5.15. As expected, elongation is reduced with increasing tensile strength. The two power series trend-line covered area on Figure 5.15 are consistent with ADI expected tensile properties given in the ASTM A897 standard [5]. There appears to be a limiting UTS (~900MPa) at which further elongation improvement does not lead to a reduction in tensile strength in the ADI samples.

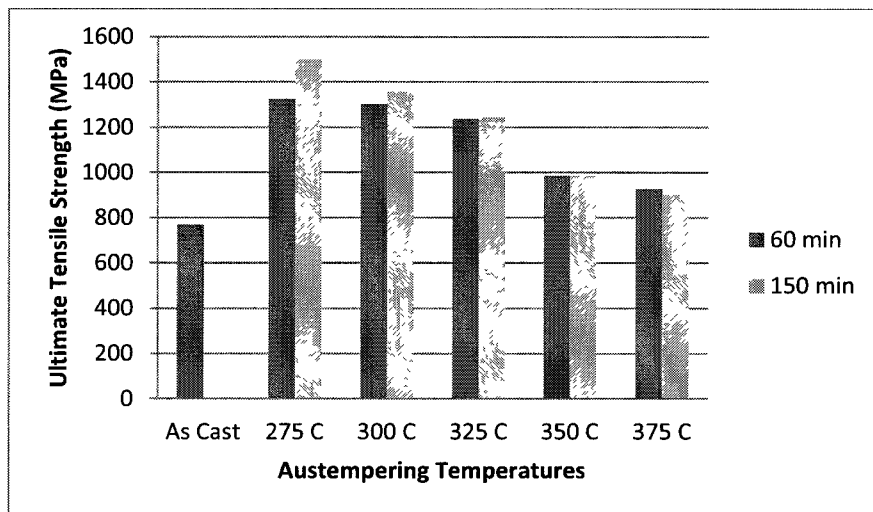


Figure 5.13: Tensile strength (MPa) of as-cast and ADI samples at 60 and 150 min austempering.

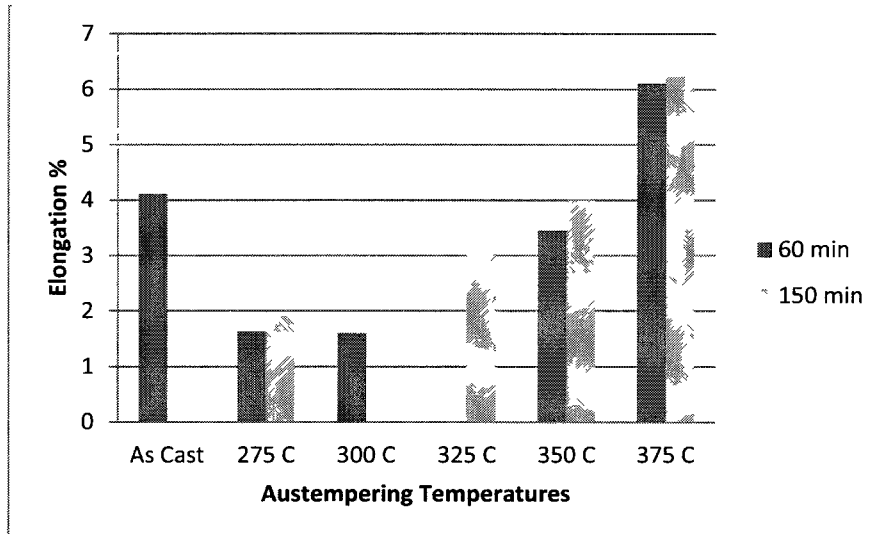


Figure 5.14: Elongation % of as-cast and ADI samples at 60 and 150 min austempering.

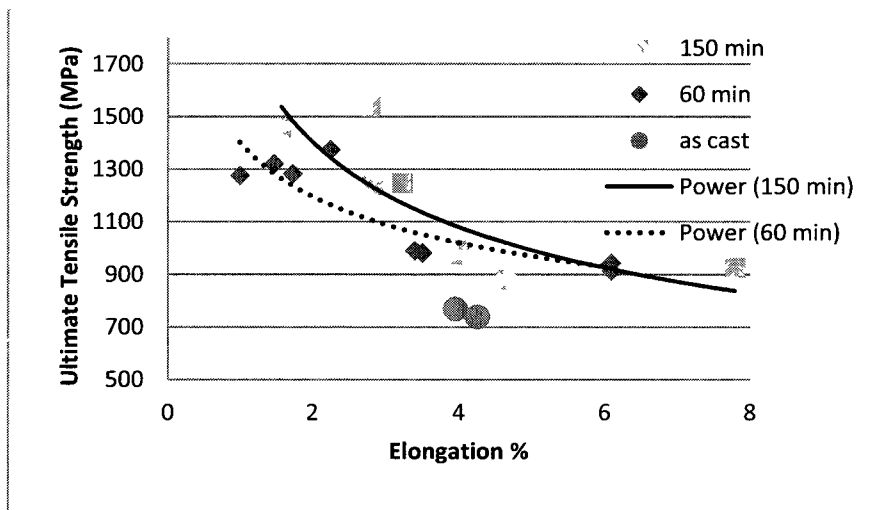


Figure 5.15: Elongation and tensile strength relation of the samples.

5.4 Mechanical Property Summary

- 1 All five grades of ASTM standard hardness were achieved with the ADI samples.
- 2 Martensitic samples had the highest hardness and feathery ausferritic samples the lowest.

- 3 Charpy toughness of the ADI samples were significantly higher than as-cast alloy. High austempering time and temperature gave high Charpy impact toughness for ADI.
- 4 High UTS was achieved by the austempering process, which is comparable to the ASTM ADI standards. ADI samples with lower temperature austempering produced very high UTS but with minimum elongation.

CHAPTER VI
SCUFFING PERFORMANCE

The scuffing failure loads at both speeds are shown on Table 6.1 and Figure 6.1. It can be seen that a lower sliding speed generated overall higher scuffing failure loads. This is expected as abrasion and surface deformation is more severe and abrupt with increasing sliding speeds [55]. For both sliding speeds, the lower austempering temperature and time samples exhibited poorer scuffing performance. Better scuffing performance was found for samples austempered at higher temperatures, and longer times. Same dark gray, gray and white color coding is used in the Table 6.1 to assign high, medium and low values.

Table 6.1: Scuffing load of ADI samples

Austempering Temperature (°C)	Time	Scuffing Load1.65 (m/s)	Scuffing Load1.35 (m/s)
275	10	90	150
	60	103	140
	150	118	148
300	10	108	136
	60	124	145
	150	110	150
325	10	118	155
	60	170	170
	150	126	162
350	10	124	155
	60	170	178
	150	140	140
375	10	128	165
	60	177	185
	150	143	182

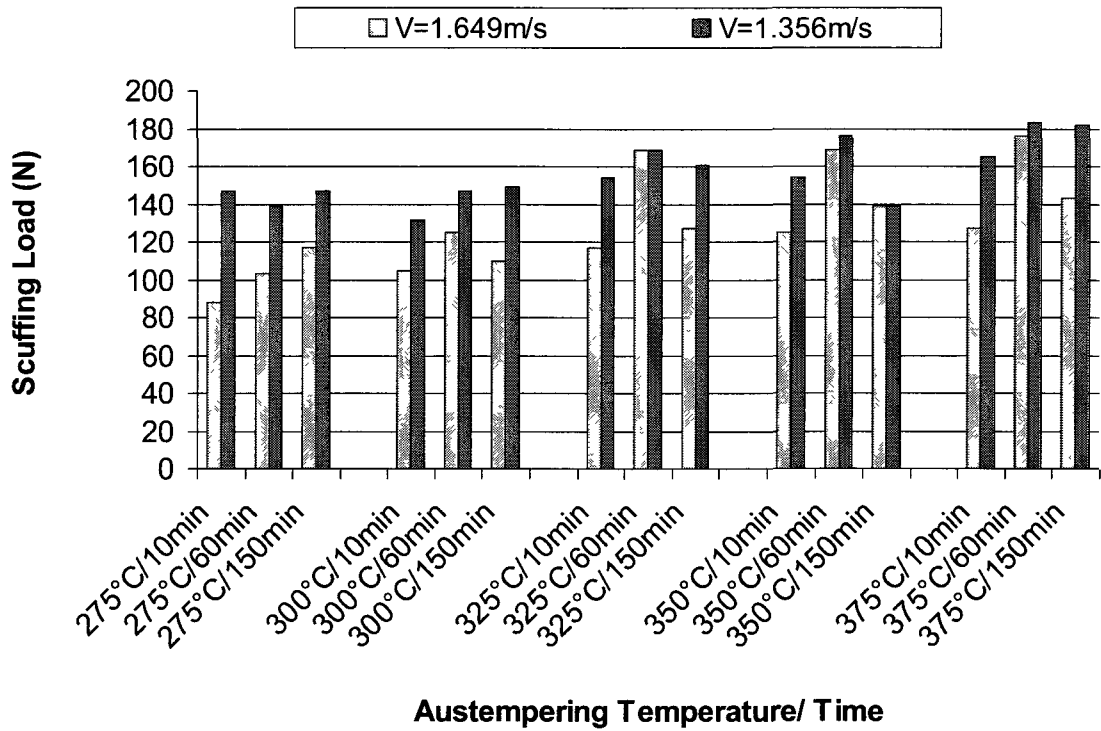


Figure 6.1: Comparison of scuffing failure loads.

When the scuffing performance as measured by the scuffing load is plotted against the % retained austenite (Figure 6.2a) it shows that the performance improves with the increasing % retained austenite.

The relationship between scuffing load and % retained austenite is given in Equations 6.1 and 6.2. The polynomial curve fitting gives an acceptable coefficient of determination R^2 values in Equations (6.1) and (6.2).

$$L = 138 - 4.496RA + 0.144(RA)^2 \quad (R^2=0.749; 1.649 \text{ m/s}) \quad \text{Equation 6.1}$$

$$L = 138 - 4.496RA + 0.110(RA)^2 \quad (R^2=0.586; 1.356 \text{ m/s}) \quad \text{Equation 6.2}$$

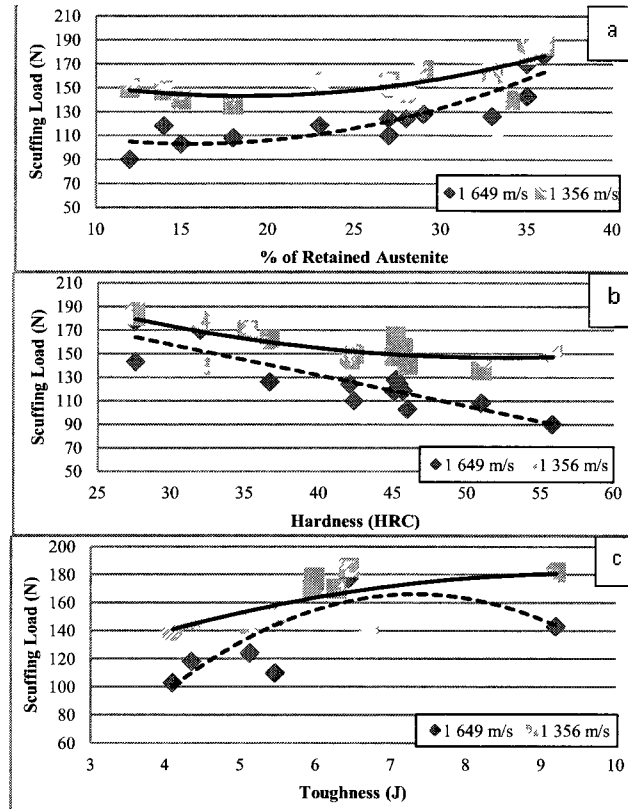


Figure 6.2 Relationship between scuffing load and (a) % retained austenite, (b) hardness and (c) toughness.

For both sliding speeds, the scuffing load increases with decreasing hardness: see Figure 6.2b and Equations (6.3) and (6.4).

$$L = 235 - 2.561H - 0.0H^2 \quad (R^2=0.728; 1.649\text{m/s}) \quad \text{Equation 6.3}$$

$$L = 294.6 - 5.685H - 0.054H^2 \quad (R^2=0.540; 1.356 \text{ m/s}) \quad \text{Equation 6.4}$$

As the hardness is inversely proportional to toughness, the scuffing load increases with higher Charpy values as shown in Figure 6.2c and Equations 6.5 and 6.6.

$$L = -6.36C^2 + 93.13C - 175.18 \quad (R^2= 0.6052; 1.649 \text{ m/s}) \quad \text{Equation 6.5}$$

$$L = -1.3C^2 + 25C + 59.88 \quad (R^2= 0.4388; 1.356\text{m/s}) \quad \text{Equation 6.6}$$

The range of toughness is approximately 5.5 to 7 J where the scuffing load was the highest. For the same notched-type sample, the as-cast alloy had a toughness of only 2.16J. The scuffing load decreases with increasing of sliding speed. The higher speed data (1.649 m/s) has higher R^2 values compared to the lower speed (1.356 m/s) data in all the plots (Figures 6.2(a-c)). This suggests that scuffing resistance at the lower sliding speed is less predictable.

It must be mentioned that the overall R^2 values found throughout the scuffing test were not very impressive. Scuffing tests are very time consuming and it is not a controlled or a precise procedure. The failure load can never be predicted perfectly, because of the nature of the scuffing mechanism. If we tested with many other samples to tabulate a large database, the coefficient of determination may have been higher. For a tribology test otherwise, the coefficient of determination is expected to be lower.

3D plots are utilized to show the scuffing load relationship with austempering time/temperature on Figure 6.3 (a-b). It can be seen that for both sliding speeds (1.65 and 1.35m/s), 60 min austempering at high temperature (350-375°C) gives the highest scuffing load performance.

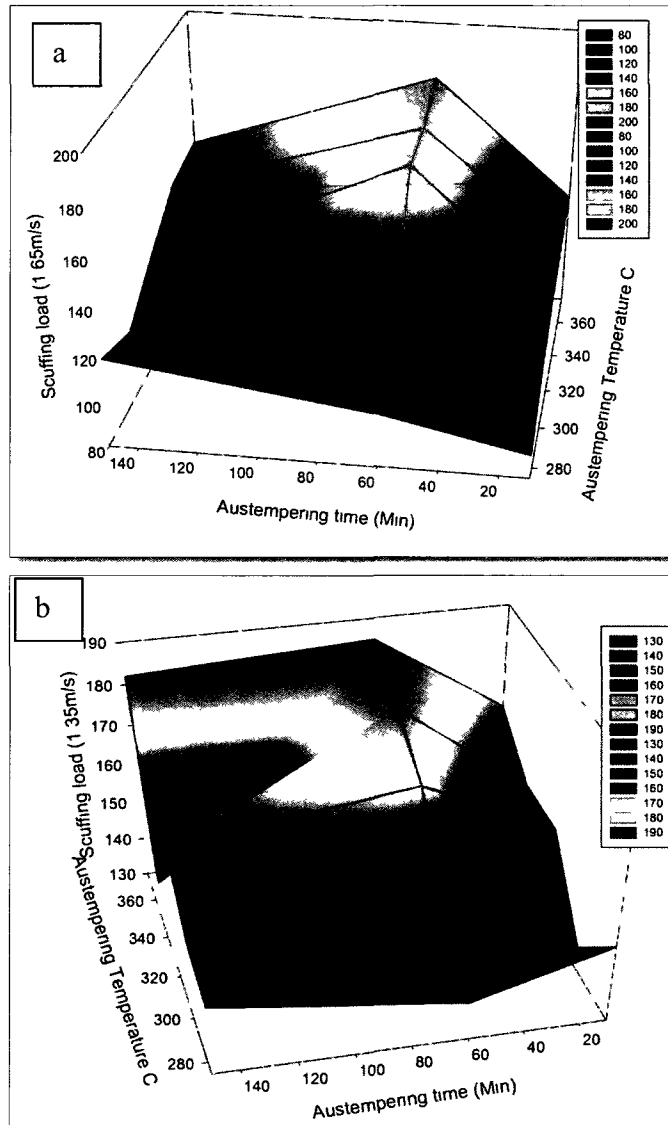


Figure 6.3: 3D plot relationship between scuffing load (N) and austempering time/temperature: a) 1.65m/s sliding speed, b) 1.35 m/s sliding speed.

The scuffing performance is ultimately related to the microstructure of the sample. As discussed in Chapter 4, the % retained austenite is dependent on the amount of ausferrite or bainitic ferrite contained in the sample. Lower % retained austenite samples have more martensite and higher % retained austenite samples have feathery and thick ausferrite. The maximum scuffing loads were found for samples with a higher fraction of

feathery ausferrite (375°C, 60min-176N), while samples with a smaller amount of ausferrite and higher martensite content showed lower scuffing loads (275°C, 10min-88N). The relative amounts of martensite and ausferrite was critical in determining the scuffing performance.

6.1 Metallurgical Examination of Scuffed Samples

SEM images were taken to understand the subsurface deformation of the scuffed ADI samples. Figures 6.4 (a-i) show the cross-sectional views of the scuffed track of the ADI samples. The first row of images, Figures 6.4 (a-c) is for 10 minute austempered samples at three different temperatures. Thin, sharp needles of the martensitic microstructure are visible in the images. Cracks are observed at the graphite/martensite matrix interfacial regions in the subsurface and cracks are seen to be propagating from the interfacial regions. The result of this crack propagation will be the generation of a wear particle and the “pull-out” of graphite. Shelton and Bonner [56] in their study of copper-containing ADI also suggested that sub-surface crack initiation and propagation, which lead to the surface delamination, always initiated at the graphite nodules. An in-situ observation of the microprocess of crack initiation and propagation in ADI by Dai and He [43] also gave similar findings. Very little plastic deformation was found in most of the 10 minute samples except at 375°C (Figure 6.4c) which has the highest content of ausferrite for samples austempered for 10 minutes (Table 5.2).

Figures 6.4 (d-f), are for with medium austempering temperatures (275-300°C and 60-150 mins). In Chapter 4, we have shown that these samples contain medium amounts of retained austenite, and some have a mixed ausferrite-martensite microstructure. Moderate plastic deformation was observed for these samples. A few

cracks were also observed, which are expected to produce wear particles after propagation. There was also deformation of the graphite due to the scuffing process.

The samples heat treated at high temperatures and long austempering times,, Figures 6.4 (g-i) exhibit a large amount of plastic deformation. The patterns of the ausferrite laths or feathery structures show signs of heavy deformation during the sliding. Very few or no cracks were seen in these samples.

Cracks can initiate easily in the harder surface during the sliding contact. Macrostructures with a hard martensitic matrix cannot “protect” the graphite nodules. The graphite is prone to pull out during sliding because of its weak strength; consequently, cracks can be propagated as in Figures 6.4 (a-c). After a low critical number of cycles, a large amount of wear particles are produced. These particles destroy the lubricant film, leading to metal-to-metal contact and eventually, catastrophic failure. This leads to a low scuffing resistance. This theory is also supported by the scuffing load-toughness relationship. Scuffing load is proportional to the toughness. Samples with lower toughness would be prone to surface cracks and debris accumulation, leading to lubricant film destruction. A tougher surface is thus the key to an improved scuffing performance.

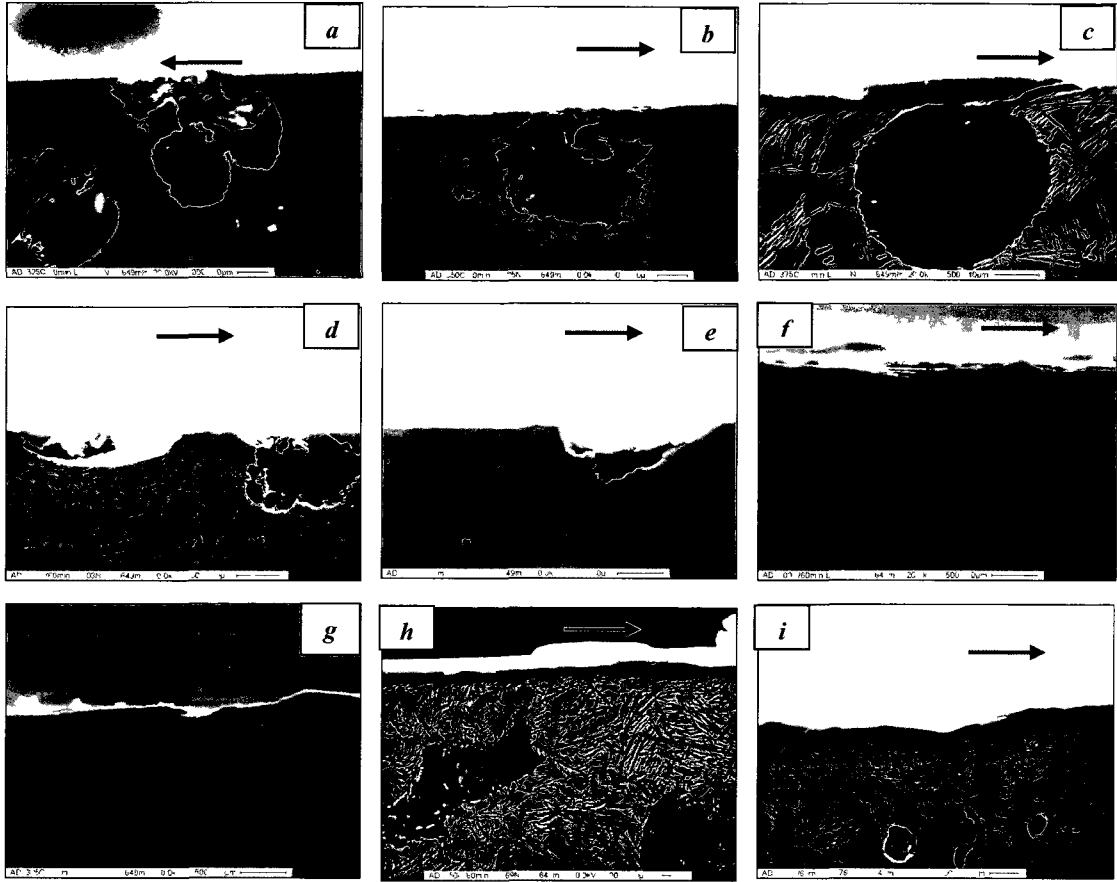


Figure 6.4:SEM image in the subsurface micrograph at sliding speed of 1.649m/s (the horizontal arrow shows the sliding direction) for ADI austempered in (a) 325°C/10min, scuffing load=117N; (b) 350°C/10min, scuffing load=125N; (c) 375°C/10min, scuffing load=127N; (d) 275°C/60min, scuffing load=103N; (e) 275°C/150min, scuffing load=117N; (f) 300°C/60min, scuffing load=125N; (g) 325°C/150min, scuffing load=127N; (h) 350°C/60min, scuffing load=169N; (i) 375°C/60min, scuffing load=176N.

A trace of a white layer is observed in Figure 6.4g. This “white layer” constituent has been mentioned in cast iron research studies dating back to the 1940s. Clayton and Jenkins [57] found that a cast iron surface rubbing against steel develops a thin layer of a white constituent. The material was assumed to have two phases; cementite and a high carbon ferritic base developed from austenite. Ludema [58] in his research on scuffing for a lubricated surface mentioned the formation of a white layer. This white layer is termed

as W2. XRD and transmission electron microscopy (TEM) analysis by Cranshaw and Company [24] suggested that W2 was a heavily deformed mixture of austenite and martensite. The formation of the strain induced martensite in austempered ductile iron has been discussed in detail by Daber et al [39, 40]. The transformation of austenite to martensite on the surface has been shown by both Johansson [59] and Ball et al [60] to lead to an increase in wear resistance of austenitic-bainitic ductile iron and stainless steels.

6.2 Scuffing Summary

- 1 Feathery ausferrite microstructure ADI gives superior scuffing performance compared to martensitic microstructure ADI.
- 2 Feathery ausferrite ADI undergoes heavy plastic deformation but very little crack initiation and propagation under scuffing.
- 3 Cracks initiate in the graphite nodule and ferrous matrix interphase of the martensitic ADI.

CHAPTER VII
CONCLUSIONS, RECOMMENDATIONS AND FUTURE WORK

The following conclusions are also drawn from this study:

1. An austenitizing temperature for our special chemistry ADI could safely be established at 890°C. The microstructural analysis of the ADI samples, as well as the initially austenitized samples showed no evidence of pearlite or α -ferrite above 890C. It can be assumed that 890C is comfortably above the inter-critical austenitizing temperature or ICAT.
2. The austenitizing time was 20 minutes. This time was selected to reduce production costs. But short austenitizing could lead to segregation of the alloying elements, with resulting inconsistencies in performance. Some of the poorer Charpy and tensile test results could be due to the low austenitizing time. Although the mechanical properties were comparable to established grades, a longer austenitizing time (1 hour) would be both practical and effective.
3. A combination of austempering time and temperature determined the microstructure. Low austempering temperatures (275-300°C) and time (10 min) produced a martensite microstructure. Increasing time and temperature (350-375°C; 60-150 min) produced a feathery ausferritic microstructure with high % retained austenite. Some samples, austempered at medium level temperatures (300-325°C), contained both ausferrite and martensite laths.
4. XRD results showed that the retained austenite levels were a function of the heat treatment process. The percentage retained austenite increases with increasing austempering time. A 60 minute austempering process generated the highest %

retained austenite since it is inside the process window for austempering. A 150 minute austempering is assumed to be entering the 2nd stage of austempering, resulting in a slight decrease in the % retained austenite.

5. All five (I-V) ASTM hardness grades were achieved by the austempering. Martensitic samples had the highest hardness level (Grade V). Ausferritic samples with thick and feathery ausferrite laths were the softest (Grade I). The hardness level can be directly related to the % of retained austenite. The hardness levels of all the heat treated samples were superior compared to the as-cast pearlite-ferrite material.
6. Charpy impact results showed that the toughness of all the austempered samples were much higher than the as-cast alloy. Toughness levels increased with increasing austempering temperature. 150 minute samples had higher toughness values compared to 60 minute samples. The thick, feathery ausferrite microstructure is beneficial in producing a high level of toughness.
7. Low to medium austempering temperatures generated a high ultimate tensile strength and low elongation (Grade IV and V). As the temperature increased, the tensile strength decreased. None of the heat treatment schedules produces the Grade I specification which is 850Mpa UTS and 11% elongation. Feathery ausferrite samples had lower tensile strength and higher elongation compared to the martensitic samples.
8. In scuffing tests, martensitic samples exhibited very little plastic deformation, but considerable crack initiation and propagation in graphite/matrix interphase. A moderate level of surface deformation was found in medium feathery ausferrite microstructure. The thick and feathery ausferrite microstructure exhibited heavy

plastic deformation and little, or no, crack initiation. The scuffing performance was significantly higher for these feathery ausferrite samples.

9. A white layer surface material, which is believed to be a deformed mixture of ferrite and martensite, could be influential in controlling the scuffing mechanism.

7.1 Recommendations for Future Work:

The target applications for ADI in this research were in automotive crankshafts (28-32 HRC), camshafts (50 HRC) and lower arm suspensions (40-45 HRC). ADI with 28-32 HRC had very good toughness and scuffing performance, which is ideal for the crankshaft application. 50HRC ADI samples had poor toughness and scuffing performance. Such ADI is not recommended for use in camshafts. Softer ADI (30-40 HRC) could be further hardened with carburizing or other hardening methods for camshaft application. This would develop a camshaft with a hard shell and a tough core. Further research is required for camshaft ADI applications. ADI in the range of 40-45HRC had moderate toughness, tensile performance and scuffing performance. Thus a lower arm application of ADI is recommended.

7.2 Recommendations for Future Work:

A wide range of mechanical and tribological properties were achieved by altering the austempering time schedules. The following work is suggested to further understand and improve ADI properties.

1. The effect of alloying elements should be studied along with the austempering schedules. Alloying elements such as Cu, Mo, Ni could alter the ADI microstructure and, thereby, properties.

2. Longer austenitizing times should be considered to ensure an uniform distribution of the alloying elements. The effects of austenitizing temperature/time would be useful information for commercial heat treaters.
3. A multistep austempering processes should be investigated as a means of improving the mechanical properties.
4. The TRIP effect or strain induces transformation should be examined in more detail. Most of the ADI components in commercial applications i.e. crank shafts and cam shafts, are expected to experience surface deformation.
5. Investigate the applicability of a surface engineered ADI where the required scuffing and wear resistance is obtained through the surface layer.

REFERENCES

1. G.E. Totten (Editor), Steel Heat Treatment Handbook, 2nd Edition , Vol 1. CRC Press- Taylor and Francis, 6000 Broken Sound Parkway NW, Boca Raton, FL, 2006, PP 1-91, 92-121,122-165.
2. Detroit Stocker Company- ADI Gear Suppliers, Available from: <http://www.detroitstoker.com/downloads/literature/AustemperedDuctileIron.PDF>. [D.O.A-28th August 2011]
3. D. Myszka, Austenite-Martensite Transformations in Austempered Ductile Iron. Archives of Metallurgy and Materials, 52(3), 2007, pp. 475-480.
4. O. Eric, M. Jovanovic, Microstructure and mechanical properties of Cu-Ni-Mo austempered ductile iron. Journal of Mining and Metallurgy, 40B(1), 2004, pp. 11-19.
5. Standard Specification for Austempered Ductile Iron Castings, A897/A897M – 06, , ASTM International: 100 Barr Harbor Drive P.O. Box C-700 West Conshohocken, Pennsylvania 19428-2959, United States, University of Windsor Leddy Library Licence Agreement Download-24/08/2011 .
6. K. B. Rundman, "It's About Austenite and Carbon, Mate"- A Story of the Physical Metallurgy of ADI-Part II, 35th Australian Foundry Institute National Conference Proceeding 31st Oct-3rd Nov 2004, Adelaide, Australia. pp 1-10.
7. GearsHub, Supplier, Manufacturer and Exporter of Industrial Gears And Custom Made Gears, Available from: <http://www.gearshub.com/ductile-iron-gears.html>. [D.O.A-15th July 2011]
8. B. C. Macdonald and Company, Available from: http://www.bcmac.com/pdf_files/surface%20finish%20101.pdf. [D.O.A-05th August 2011]
9. A Design Study in Austempered Ductile Iron-Drive Wheel for the Tracks on a Compact Utility Loader, AFS-International, 2005 , Available from: http://www.sfsa.org/tutorials/drive_wheel/Drive%20Wheel.pdf. [D.O.A-05th August 2011]
10. Lethbridge Iron-Works, Alberta. Producer and Supplier of ADI Components, Available from: http://www.lethbridgeironworks.com/ADI_pages/ADI.html. [D.O.A-18th August 2011]
11. T.H.Dick & Co Limited, 2007, Available from: http://thdick.co.uk/index.php/grades/adi_austempered_ductile_iron. [D.O.A-25th August 2011]

12. M. A. Kenawy, A. M. Abdel-Fattah, N. Okasha, M. El-Gazery, Mechanical and Structural Properties of Ductile Cast Iron. *Egyptian Journal of Solids*, 24(2), 2001, pp. 151-159.
13. W. D. Callister, *Materials Science and Engineering-An Introduction*, 7th Edition, York, PA, U.S.A, John Wiley and Sons,2007, pp. 253-304, 312-356
14. M. A. Y. Gonzalez, Modelling the Microstructure and Mechanical Properties of Austempered Ductile Irons, in Department of Materials Science and Metallurgy (PhD Thesis), University of Cambridge, Cambridge, 2001, pp. 5-183.
15. A. Leiro, Tribological Studies on Various Materials Under Mixed-Boundary Lubrication Regime (M. A. Sc Thesis), Department of Materials Science. 2009, Lulea University of Technology, Lulea.
16. T. Tun, K. T. Lwin, Optimizing the Microstructure and the Mechanical Properties of Austempered Ductile Iron for Automobile Differential Gear, *Journal of Metals, Materials and Minerals*, 18(2), 2008, pp. 199-205.
17. J. Yang, S. K. Putatunda, Improvement in strength and toughness of austempered ductile cast iron by a novel two-step austempering process, *Materials and Design*, 25, 2004, pp. 219-230.
18. J. Achary, D. Venugopalan, Microstructural Development and Austempering Kinetics of Ductile Iron During Thermomechanical Processing, *Metallurgical and Materials Transactions A*, 31(A), 2000, pp. 2575-2585.
19. K. B. Rundman, D. J. Moore, K. L. Hayrynen, W. J. Dubensky, T. N. Rouns, The Microstructure and Mechanical Properties of Austempered Ductile Iron, *Journal of Heat Treatment*,. 5(2), 1988, pp. 79-95.
20. S. K. Putatunda, P. K. Gadicherla, Influence of Austenitizing Temperature on Fracture Toughness of a Low Manganese Austempered Ductile Iron (ADI) with Ferritic As Cast Structure, *Material Science and Engineering*, 268(A), 1999, pp. 15-31.
21. K. Ogawa, S. Kajiwara, Basic Differences Between Martensitic and Bainitic Transformation Revealed by High-Resolution Electron Microscopy, *Material Science and Engineering*, A438(440), 2006, pp. 91-94.
22. H. Chandler, *Heat Treater's Guide – Practices and procedures for iron and steels*, 2nd Edition, 1995, pp.831, ASM International, Materials Park, OH
23. J. Qu., J. J. Truhan, P. J. Blau, R. Ott, The Development of a 'Pin on Twin' Scuffing Test to Evaluate Materials for Heavy-Duty Diesel Fuel Injectors, *Tribology Transactions*, 50, 2007, pp. 50-57.

24. T. E. Cranshaw, R. G. Company, The Study of Scoring and Scuffing on Lubricated Sliding Surfaces by Mossbauer Spectroscopy, *Journal De Physique*, C2(3), 1979, pp. 589-591.
25. P. J. Blau, J. Qu, Transient scuffing of candidate diesel engine materials at temperatures up to 600C, Technical Report for Oak Ridge National Library, Report Number ORNL/TM-2003/142, June 2003
26. Y. Sahin, M. Erdogan, V. Kilicli, Wear Behaviour of Austempered Ductile Irons with Dual Matrix Structures. *Material Science and Engineering*, A(444), 2007, pp. 31-38.
27. M. J. Perez, M. M. Cisneros, H. F. Lopez, Wear Resistance of Cu-Ni-Mo Austempered Ductile Iron. *Wear*, 260, 2006, pp. 879-885.
28. J. Zimba, M. Samandi, D. Yu, T. Chandra, E. Navara, D. J. Simbi, Un-Lubricated Sliding Wear Performance of Unalloyed Austempered Ductile Iron Under High Contact Stresses. *Materials and Design*, 25, 2004, pp. 431-438.
29. L. Magalhaes, J. Seabra, Wear and Scuffing of Austempered Ductile Iron Gears *Wear*, 215, 1998, pp. 237-246.
30. V. Kilicli, M. Erdogan, Effect of Ausferrite Volume Fraction and Morphology on Tensile Properties of Partially Austenitized and Austempered Ductile Irons with Dual Matrix Structures, *International Journal of Cast Metals Research*, 20(4), 2007, pp. 202-213.
31. R. J. Warwick, P. Althoff, P. H. Mani, M. L. Rackers, Austempered Ductile Iron for Chassis Applications, SAE Technical Paper Series 2000, SAE. Detroit, MI,
32. OEM Off Highway: Solution for the Off-road Market (Online Industrial Magazine), Available from: <http://www.oemoffhighway.com/product/10184301/austempered-ductile-iron>. [D.O.A-25th August 2011]
33. Oil City Iron Works, Foundry Company and ADI Component Suppliers, Available from: <http://www.ociw.com/materialsproduced.html>. [D.O.A-25th August 2011]
34. Y. J. Kim, H. Shin, H. Park, J. D. Lim, Investigation into Mechanical Properties of Austempered Ductile Cast Iron (ADI) in Accordance with Austempering Temperature, *Materials Letters*,. 62, 2007, pp. 357-360.
35. O. Eric, M. Jovanovic, D. Rajnovic, Z. Burzic, L. Sidjanin, Fracture Toughness of Alloyed Austempered Ductile Iron (ADI), *Fracture of Nano and Engineering Materials and Structures*, C23, 2006, pp. 1145-1146.
36. K. S. Ravishankar, U. K. Rajendra, P. P. Rao, Development of Austempered Ductile Iron for High Tensile and Fracture Toughness by Two Step Austempering Process.

- in 68th WFC-World Foundry Congress Proceeding 7th to 10th February , 2008, Chennai, India, pp. 35-40
37. B. Bosnjak, B. Radulovic, Effect of Austenitising Temperature on Austempering Kinetics of Ni-Mo Alloyed Ductile Iron. *Materiali in Tehnoloije*, 38(6), 2004, pp. 307-312.
 38. B. Bosnjak, B. Radulovic, R. Harding, K. P. Tonev, V. Asanovic, The Influence of Austenitising Temperature on the Microstructure and Mechanical Properties of Low-Alloyed Ni-Mo-Cu Austempered Ductile Iron. *Materiali in Tehnoloije*, 34(5), 2000, pp. 207-215.
 39. S. Daber, P. P. Rao, K. S. Ravishanker, Influence of Austenitising Temperature on the Formation of Strain Induced Martensite in Austempered Ductile Iron. *Journal of Material and Science*, 43, 2008, pp. 4929-4937.
 40. S. Daber, P. P. Rao, Formation of Strain-Induced Martensite in Austempered Ductile Iron. *Journal of Material and Science*, 43, 2008, pp. 357-367.
 41. A. Trudel, M. Grange, Effect of Composition and Heat Treatment Parameters on the Characteristics of Austempered Ductile Iron. *Canadian Metallurgical Quarterly*, 35(5), 1997, pp. 289-298.
 42. R. C. Thomson, Modelling Microstructural Evolution in Cast Alloys. WFT-World Foundry Congress Conference Proceeding. 4-7th June 2006. Harrogate, UK, pp 1-12.
 43. P. Q. Dai, Z. R. He, C. M. Zheng, Z. Y. Mao, In-situ SEM Observation on the Fracture of Austempered Ductile Iron. *Material Science and Engineering*, A319(321), 2001, pp. 531-534.
 44. Y. N. Taran, K.I.U., A. Y. Kustov, The Bainite Reaction Kinetics in Austempered Ductile Iron. *J. PHYS. IV FRANCE*, 1997. 7(C5): p. 429-434.
 45. Bhadeshia, H.K.D.H., *Bainite in Steels*. 2nd ed. 2001, London: The Institute of Materials.
 46. U. R. Kumari, P. P. Rao, Study of the Wear Behaviour of Austempered Ductile Iron. *Journal of Material and Science*, 44, 2009, pp. 1082-1093.
 47. ASTM Standard E23-07a. 2007, ASTM International: 100 Barr Harbor Drive P.O. Box C-700 West Conshohocken, Pennsylvania 19428-2959, United States, University of Windsor Leddy Library Licence Agreement Download-24/08/2011.
 48. Annual Book of ASTM Standards-ASTM Standards E8-04. 2006 ed, ed. V.A.M.e. al. Vol. Vol. 03.01. 2006, West Conshohocken, PA, USA: ASTM International. 64-87.

49. C. Secieru, I. Dumitru, Fractal Analysis of Fracture Surfaces of Steel Charpy Specimens. *Key Engineering Materials*, 399, 2009, pp. 43-49.
50. Misumi South East Asia, Instrument Company, Available from: http://sg.misumi-ec.com/pdf/tech/press/pr1167_1168.pdf [D.O.A-25th August 2011]
51. ASTM Standards (E975-03), Standard Practice for Xray Determination of Retained Austenite in Steel with Near Random Crystallographic Orientation., in *American Society for Testing and Materials*. 2003, ASTM International: West Conshohocken, PA, USA.
52. *Properties and Selection Irons, Steels, and High-Performance Alloys*, in *Metals Handbook*. 1990, ASTM International, Materials Park, OH, USA.
53. ImageJ, Research Services Branch NIMH & NINDS. ImageJ - Image processing and analysis in Java. Web site: <http://rsb.info.nih.gov/ij/>.
54. Kathleen Mills *et al.*(Editor) *ASM Handbook: Metallography and Microstructures*. 9th ed, ed, Vol. 9, Materials Park, OH, USA: ASM International, 1985, pp. 242-255.
55. L. Magalhães, J. Seabra, C. Sá, Experimental Observations of Contact Fatigue Crack Mechanisms for Austempered Ductile Iron (ADI) Disc, *Wear*, 246, 2000, pp. 134-148.
56. P.W. Shelton, A. A. Bonner, The Effect of Copper Addition to the Mechanical Properties of Austempered Ductile Iron (ADI). *Journal of Materials Processing Technology*, 173, 2005, pp. 269-274.
57. D. Clayton, C. H. M. Jenkins, Physical Changes in Rubbing Surfaces on Scuffing. *British Journal of Applied Physics*, 2, 1951, pp. 69-78.
58. K. C. Ludema, A review of scuffing and running-in of lubricated surfaces, with asperities and oxides in perspective. *Wear*, 100, 1984, pp. 315-333.
59. M. Johansson, Austenitic-Bainitic Ductile Iron. *AFS Transactions*, 85, 1977, pp. 117-122.
60. A. Ball, C. Allen, B. Prothoreo, The abrasive-corrosive wear of stainless steel. *Wear*, 74, 1981, pp. 287-305.

PUBLICATIONS AND PRESENTATIONS

Publications

T. Nasir, D. O. Northwood, J. Han, Q. Zou, G. Barber, X. Sun, P. Seaton, Heat treatment – microstructure –mechanical/tribological property relationships in austempered ductile iron, WIT Transactions of Engineering Science, Vol 71, 2011, pp 159-170.

Presentations

“Heat treatment – microstructure –mechanical/tribological property relationships in austempered ductile iron”, T. Nasir, D. O. Northwood, J. Han, Q. Zou, G. Barber, X. Sun, P. Seaton, Presented at 10th International Conference on Surface Effects and Contact Mechanics, Malta, 21-23 September , 2011

VITA AUCTORIS

NAME	Tanzim Nasir
PLACE OF BIRTH	Dhaka, Bangladesh
DATE OF BIRTH	October 18 th , 1985
EDUCATION	Secondary School Certificate (SSC) Government Laboratory High School Dhaka, Bangladesh 2001
	Higher Secondary Certificate (HSC) Dhaka College Dhaka, Bangladesh 2003
	Bachelor (Hons) of Mechanical Engineering Multimedia University Malacca, Malaysia 2009
	Masters of Applied Science Engineering Materials University of Windsor Windsor- ON, Canada 2011